Cape Peninsula
University of Technology

Saturated absorption spectroscopy of rubidium and feedback control of LASER frequency for Doppler cooling

by

Adrian L. Wyngaard

Thesis submitted in partial fulfilment of the requirements for the degree

Master of Engineering: Electrical Engineering

in the faculty of Engineering

at the Cape Peninsula University of Technology

Supervisor: Dr. Kessie Govender
Co-Supervisor: Dr. Christine Steenkamp

Bellville
February, 2018

Declaration

I, Adrian Leigh Wyngaard, declare that the contents of this thesis represent my own unaided work, and that the thesis has not previously been submitted for academic examination towards any qualification. Furthermore, it represents my own opinions and not necessarily those of the Cape Peninsula University of Technology.

Signed	Date

Abstract

This research investigates the absorption spectra of rubidium and the feedback control of an external cavity diode laser. This research is a necessary prerequisite for laser (Doppler) cooling and trapping of rubidium atoms.

Cooling rubidium atoms down to such low temperatures can be achieved using the Doppler cooling technique. Here a laser is tuned to remain resonant with a specific atomic transition. To do this, the absorption spectra of rubidium must therefore be observed. All of the above require a reasonable knowledge about topics such as atomic physics, laser cooling and trapping, feedback control systems, and absorption spectroscopy. A discussion of these topics is provided.

We have utilised an experimental setup which allowed for measurements of the Doppler broadened and Doppler free absorption spectra of rubidium, as well the analysis of the Zeeman effect on the Doppler free spectra. The setup consisted of a saturated absorption spectrometer for high resolution spectroscopy and a Michelson interferometer for calibrating our measurements. In analysing the Zeeman effect we added a set of Helmholtz coils to the saturated absorption spectroscopy arrangement to measure the splitting of the hyperfine energy levels. We also performed a theoretical analysis of

the magnetic energy level splitting of rubidium.

Our estimations of the separations and lifetimes of the $5S_{1/2}$ and $5P_{3/2}$ hyperfine energy levels of rubidium 85 and 87 showed agreement with current literature. The analysis of the Zeeman splitting at the $5S_{1/2}$ and $5P_{3/2}$ hyperfine energy levels showed large variations between theory and experiment. However, this was improved by comparing measurements with theoretical predictions of transitions that were different to our initial assumptions.

In addition to observing the absorption spectra we used a pre-built laser frequency feedback control system to maintain the laser frequency at a specific hyperfine absorption line. While the laser was locked to this transition we subjected the system to various disturbances; the laser remained locked. We managed to lock the laser to the same transition for roughly an hour.

The results of our absorption spectroscopy experiment as well as the laser locking experiment show that a good foundation has been laid for future work involving the study of cold atoms.

Acknowledgements

Firstly, I wish to thank Dr. Kessie Govender, from the Department of Electrical, Electronic, and Computer Engineering at the Cape Peninsula University of Technology. The amount of time and effort he has put into guiding me through this research project is greatly appreciated. From providing nearly three years of unofficial physics lectures, to assisting me with theoretical calculations; he has been very patient and has always been a great motivator. I could not have asked for a better supervisor.

I would also like to thank Dr. Christine Steenkamp from the Department of Physics at Stellenbosch University. Her experience in the field of atomic physics has afforded me invaluable insight to the research undertaken in this thesis, and her assistance in the write-up of the thesis is very much appreciated.

I thank the members of the Quantum Physics Research Group at the Cape Peninsula University of Technology for their contributions to this research, as well as their company during the last three years. I also thank the technical staff in the Department of Electrical, Electronic, and Computer Engineering at the Cape Peninsula University of Technology for assistance that they have provided during the duration of the research.

On behalf of our Quantum Physics Research Group, I wish to thank Stellenbosch University and Dr. Christine Steenkamp for providing us with the necessary laboratory equipment in order to conduct this research. We also acknowledge the Council for Scientific and Industrial Research (CSIR) National Laser Centre for providing us with Lasers and other opto-mechanical components.

I thank the Cape Peninsula University of Technology, French South African Institute of Technology (F'SATI), and the National Research Foundation for their financial support through this research project. (Opinions expressed in this thesis and the conclusions arrived at, are those of the author, and are not necessarily to be attributed to the National Research Foundation.)

Lastly, I am forever grateful to my parents, family, and friends. Although you have not contributed directly to the research, you have definitely motivated me all the way through.

Research Outputs

Wyngaard, A., Govender, K., and Steenkamp, C. (2016), "Measurements of the Hyperfine and Weak-Field Zeeman Spectra of Rb 85 and Rb 87", *Poster presentation at the 61st Annual Conference of the South African Institute of Physics (SAIP2016).*

Patel, M., De Jager, G., Nkosi, Z., Wyngaard, A., and Govender, K. (2017), "On the non-linear spectroscopy including saturated absorption and four-wave mixing in two and multi-level atoms: a computational study", *IOP Conf. Series: Journal of Physics: Conf. Series 905.*

Wyngaard, A., De Jager, G., Steenkamp, C., and Govender, K. (2017), "Experimental study of the weak field Zeeman spectra of 85Rb and 87Rb", *The Proceedings of the 62nd Annual Conference of the South African Institute of Physics (SAIP2017).*

Opeolu, V., Govender, K., Wyngaard, A., Ouassini, N., De Jager, G., and Scarrot, J. (2017), "Analysis and Performance of a closed loop external cavity diode laser control system", *The Proceedings of the 62nd Annual Conference of the South African Institute of Physics (SAIP2017).*

Opeolu, V., Govender, K., Wyngaard, A., Ouassini, N., De Jager, G., and Scarrot, J. (2017), "Analysis and Performance of a closed loop external cavity diode laser control system", *Poster presentation at the 62nd Annual Conference of the South African Institute of Physics (SAIP2017).*

Contents

Chapter 1

Introduction

In this thesis we present the study of the absorption spectra of rubidium with the view to locking an external cavity diode laser to a particular atomic transition of rubidium for future experiments involving laser cooled neutral atoms. This project forms part of the research and development of quantum technologies conducted by a group of engineers and scientists at the Cape Peninsula University of Technology.

The research involved a spectral analysis of rubidium using saturated absorption spectroscopy, followed by the locking of an external cavity diode laser to a specific atomic transition of rubidium using feedback control. The spectral analysis of rubidium was carried out using a saturated absorption spectroscopy setup where two arrangements were investigated, as well as a Michelson interferometer. Both arrangements yielded results that showed agreement with the current literature. Additionally, a pair of Helmholtz coils were added to the absorption spectroscopy setup in order to investigate the weak field Zeeman effect on the absorption spectra of rubidium. Locking the laser to one of the atomic transitions of rubidium was performed using a previously built feedback system which was based on a proportional-integral-derivative controller. The performance of this system was investigated. A lock-in amplifier was later developed in order to improve the performance of the feedback system, however this was not properly characterised due to time constraints.

The motivation for this research was based on the fact that it has become increasingly apparent that quantum systems will provide the next step in improving technologies such as computing, communications and cryptography. Currently these technologies are based on principles of classical physics which have fundamental limitations, limitations that quantum systems could overcome. A simple way of explaining the advantage of a quantum system is to compare quantum and classical computers. Computers operate using bits and each bit has two possible states. Suppose we have an n bit system, classical computers would then have 2^n possible states and can be in one state at any given time. In a quantum computer these bits are represented using the ground and excited energy states of an atom. The advantage is due to the principle of quantum superposition which says that an atom may be in both energy states at any given time. Quantum computers can therefore be in all 2^n states at any given time, a tremendous advantage in computational ability (Nielsen and Chuang, 2010).

Quantum systems, however, are not straightforward. Conventional methods for measuring the state of a quantum system destroy the quantum state. Realising techniques for non-disruptive measurements of quantum systems is therefore essential for the development of quantum technologies. Additionally, quantum systems are very sensitive to decoherence and thermal degradation from interactions with the environment. To increase coherence periods, the atoms must be cooled to sub-Kelvin temperatures (Bloch, 2008).

Cooling of atoms to these temperatures can be accomplished using a system of lasers. The lasers have to be tuned to two suitable energy levels of the atom. This research is an endeavour to understand the energy level structure of rubidium in order to conduct experiments involving the cooling of rubidium atoms using lasers. Integral to this is the locking of a laser to a particular atomic transition of rubidium, which is included in the research.

1.1 Aim of Research

The aim was to conduct measurements of the rubidium absorption spectra and to lock the laser to the relevant atomic transitions of rubidium used in laser cooling experiments. To achieve this, the following objectives were identified:

1. Perform a detailed study of the absorption spectra of rubidium using saturated absorption spectroscopy.
2. Conduct a detailed study of the absorption spectra of rubidium when the atoms are placed in a magnetic field, i.e. Zeeman spectra.
3. Investigate and implement suitable laser locking schemes for future laser cooling experiments.

1.2 Literature Review

This section provides a review of the literature related to our aim, which was to investigate the absorption spectra of rubidium for the purpose of locking an external cavity diode laser to an atomic transition of rubidium as required for the cooling of rubidium atoms. The section thus reviews literature relating to topics such as Doppler cooling, laser locking, and spectroscopic studies of rubidium. We begin with a brief overview of laser cooling since it was the motivation for the research.

Research involving cold atoms begins with reducing the temperature of the atoms down to the microkelvin range. This can be achieved using a device called a magneto-optical trap, which enables both trapping and cooling of atoms by using magnetic fields and lasers. The atoms to be cooled are generally those found in group 1 of the periodic table as they have only one valence electron which simplifies both the theoretical and practical considerations. Rubidium and Caesium are the most typically used group 1 atoms since the wavelength required for excitation at particular energy states is commonly produced by diode lasers, therefore making experiments cheap and easy to conduct (Sesko, Fan, and Wieman, 1988; Macadam, Steinbach, and Wieman, 1992).

1.2.1 Doppler Cooling

The idea of cooling atoms via laser radiation was introduced by Hansch and Schawlow (1975). They suggested that by keeping the laser light to frequencies at the lower half of the atomic absorption line, the radiation pressure of the light and the velocity-dependent absorption (due to the Doppler effect) could reduce the average kinetic energy and therefore cool the gas. It was estimated that this could provide a reduction in the temperature of a gas such that the absorption line width could be reduced from a Doppler width to the natural line width.

Initial experiments, performed by Gordienko et al. (1977) and Wineland, Drullinger, and Walls (1978), involved cooling of atoms and ions respectively, with a single beam. The process, called Doppler cooling, was then improved by multiple researchers (e.g. Balykin, Letokhov, and Mushin, 1979; Dalibard, Reynaud, and Cohen-Tannoudji, 1984; Prodan et al., 1985; and Chu et al., 1985). These researchers found that the cooling efficacy could be increased by scanning the laser frequency, having a three dimensional beam configuration, and having orthogonal beam polarisations for each of the three beam axes. Thereafter, the idea of generating beams using smaller, cheaper, and more readily available diode lasers was presented by Sesko, Fan, and Wieman (1988).

Cooling atoms to sub-Kelvin temperatures is desired for any research involving cold atoms; getting to sub-Kelvin temperatures via Doppler cooling is still a common starting point. Recent experiments by Wesenberg et al., 2007 and Stellmer et al., 2013 show how relevant the Doppler Cooling technique still is. Furthermore, Doppler cooling has also been used in the demonstration of Bose-Einstein condensation of a gas (Stellmer et al., 2013).

1.2.2 Laser Frequency Locking

Locking the frequency of the light from a laser (laser locking) to an atomic transition is critical to the Doppler cooing process. Macadam, Steinbach, and Wieman (1992) have discussed how a narrow-band tunable diode laser can be locked to either side of an absorption peak, observed in saturated absorption spectroscopy, by using a proportional-integral-derivative feedback control system to adjust laser cavity length and thus the laser frequency;

this is a side locking technique. Locking the laser to the top of an absorption peak (peak locking) was demonstrated by Weel and Kumarakrishnan (2002) where they made use of a lock-in amplifier for locking the laser frequency.

Saturated absorption spectroscopy using polarised beams (polarisation spectroscopy) has also been used to stabilise the frequency of a laser (Lancaster et al., 1999; Hansch and Couillaud, 1980). Using polarisation spectroscopy, Ratnapala et al. (2004) were able to achieve a 200 MHz region for controlling the locked laser which enabled them to induce large frequency steps over short time scales without losing stabilisation, ideal for use in laser cooling experiments.

A technique known as dichroic atomic vapour laser locking (DAVLL), which uses Zeeman shifted absorption lines to provide a broader range for controlling the the locked laser frequency, was demonstrated by Corwin et al. (1998). In their experiment, a 100 gauss (G) magnetic field was used to induce the Zeeman shifts and a sub-MHz linewidth was acquired although this was performed using a Doppler broadened absorption line; their experiment was based on that of Cheron et al. (1994). Petelski et al. (2003) improved on this technique by demonstrating Doppler free DAVLL, they were able to achieve a linewidth of 100-500 KHz using a magnetic field of 11 G. Like Petelski et al. (2003), Okubo, Iwakuni, and Hasegawa (2012) achieved a narrow linewidth (300 KHz) but instead used a transverse magnetic field in their setup. The DAVLL method is desirable not only for providing a broader range for controlling the the locked laser frequency, but also because it does not involve modulating the laser frequency, which leads to heating effects in laser cooling experiments (Weel and Kumarakrishnan, 2002).

1.2.3 Absorption Spectroscopy

To lock the laser frequency at one of the atomic transitions of rubidium, the absorption spectra of rubidium must be observed. Absorption spectroscopy is thus critical to understanding and demonstrating laser cooling and locking, and should be the starting point for any experiments involving cold atoms.

After the development of the continuous wave laser (Javan, Bennet, and Herriott, 1961), the study of the interaction between light and atoms was vastly improved due to the characteristics of the laser. It was later shown that a transition may be saturated by having counter propagating beams interact with the same velocity atoms (Lamb, 1964), the process was called hole burning. This process was further investigated by many researchers (Basov, O. Kompanets, et al., 1971; Letokhov, 1969; Basov, I. Kompanets, et al., 1969) who found uses such as laser stabilisation and narrow resonance observation. Wieman and Hansch (1976) demonstrated that a change in polarisation of the beams resulted in a better-signal-to-noise ratio than that of saturated absorption spectroscopy. This allowed the observation of the Stark splitting of the fine electronic structure of hydrogen and deuterium. The study of the hyperfine structure and its use in laser stabilisation was demonstrated by O. Kompanets et al. (1976).

Macadam, Steinbach, and Wieman (1992) published a thorough guide for constructing an inexpensive narrow-band tunable diode laser for saturated absorption spectroscopy. They used a proportional-integral-derivative feedback control system to adjust laser cavity length for frequency stabilisation and achieved a sub-MHz linewidth ideal for high-resolution absorption spectroscopy. Doppler free absorption experiments are now quite common and inexpensive, such that they have been recommended for teaching in undergraduate courses (Preston, 1996), and measurements have been performed in undergraduate laboratories (Rao, Reddy, and Hecht, 1998). Although the hyperfine structure of the ground and first excited state of rubidium is well documented (Steck, 2015), recent Doppler free absorption measurements have been reported by Vachaspati and Pasterski (2013) and Bader and Zhou (2013).

Investigations of the effect of an external magnetic field on the spectral measurements show further splitting in the energy level structure of an atom. This splitting of energy levels is known as the Zeeman effect. Understanding the physics of this interaction is important for the cooling of atoms since trapping cold atoms requires the use of magnetic fields. Nakayama, Series, and Gawlik (1980) studied the Doppler free absorption spectrum at the D1 line of sodium in the presence of a 50 gauss magnetic field. Their results were compared with first order optical pumping theory in order to interpret the measured spectrum which had many crossover resonances. Bowie, Boyce, and Chiao (1995) showed observations of the weak-field Zeeman splitting in the D1 line of rubidium, although Kim et al. (1997) later showed that their measurements of the same spectrum yielded slightly different results when compared to other theories that describe the Zeeman splitting. More recently Bader and Zhou (2013) investigated the Zeeman effect on the hyperfine structure of the D2 line in rubidium and Hakhumyan et al. (2011) have studied the D1 and D2 lines in rubidium in the presence of strong magnetic fields. The weak field Zeeman effect has also been used to demonstrate magnetometry (Ram, Pattabiraman, and Vijayan, 2007).

1.3 Delineation of Research

This project involved the study of the absorption spectra of rubidium and the locking of an external cavity diode laser to a particular atomic transition, both in preparation for future experiments which involve the cooling of rubidium atoms. It did not include the cooling of atoms, the construction of a magneto optical trap, or generation of the various laser beams required for cooling rubidium atoms.

The spectroscopic study was limited to rubidium 85 and rubidium 87 isotopes using an tunable external cavity diode laser. Included in the study was an investigation of the effects of a weak external magnetic field on the absorption spectra using a pair of Helmholtz coils. The laser locking study involved the characterisation of an existing feedback system based on a proportional-integral-derivative controller.

1.4 Thesis Outline

This thesis is organised as follows. A theoretical background required to understand the aim of the project is provided in chapter two, which is followed by the experimental setup in section three. Sections four and five discuss the results of the spectral analysis of rubidium, and performance tests of the laser locking system is provided in chapter six. The research is concluded in chapter seven, followed by appendices which are referenced in the preceding chapters.

Chapter 2

Theory

2.1 Introduction

In order to conduct this research, it was necessary to have a sound grasp of the principles of various aspects of atomic physics. In this regard, the following will be discussed below: the quantum physics of atoms and photons, Doppler cooling, and absorption spectroscopy and interferometry; further reading on these topics can be found in books such as Eisberg and Resnick (1985a) and Svanberg (2003a). Basic feedback control theory is included in this discussion since in the long term we wish to lock the laser frequency to one of the absorption frequencies of rubidium.

2.2 Atomic Physics

2.2.1 Models of the atom

Although the structure of the atom is now best explained by a quantum mechanical treatment of the subject, we will begin this discussion with the

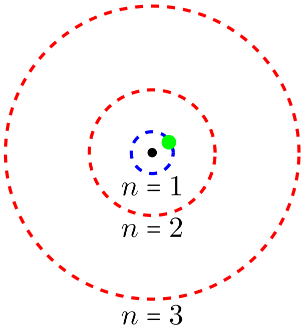

Figure 2.1: *Bohr model of a one-electron atom showing an electron (green) orbiting a nucleus (black), with orbits denoted by n.*

semi-classical treatment. The semi-classical theory of the atom is commonly explained using the Bohr model in figure 2.1, which shows the simple case of a one-electron (hydrogenic) atom.

The semi-classical theory states that electrons can exist only in certain orbits, also called energy states or levels, where no radiation of energy occurs while in these orbits. Absorption or emission of energy can only occur when the atom undergoes a transition between two energy states and this energy is equivalent to the change in energy between the two states:

$$\Delta E = E_1 - E_2 = hf \tag{2.1}$$

where h is Planck's constant and f is the frequency of the radiation.

This theory gives the energy of an atom as

$$E_n = -\frac{1}{n^2}\left(\frac{Ze^4 m}{8{\epsilon_0}^2 h^2}\right) \tag{2.2}$$

where n is the orbit, Z is the atomic number ($Z = 1$ for hydrogen), e is the electron charge, m is the electron mass, and ϵ_0 is the permittivity of free space. Since the terms in brackets are essentially constants, the energy at any orbit is therefore dependent on the value of n, the principal quantum number. The lowest value for n, one, corresponds to the orbit closest to the nucleus and values above one correspond to orbits farther from the nucleus, these are known as ground and excited states respectively.

At the sub-atomic level however, particles (such as electrons) behave like waves and these are more accurately described using a quantum mechanical approach. This wave-like behaviour is characterised by the wave function, Ψ, of the particle. To extract information from the wave function a mathematical operator must act on it. To obtain the energy of the atom, as in the semi-classical approach, we use the energy operator known as the Hamiltonian $\hat{H}$. The energy is then given by

$$\begin{aligned} \hat{H}\Psi &= E\Psi \\ \left[\frac{-\hbar^2}{2m}\nabla^2 + V(\mathbf{r})\right]\Psi &= E\Psi \end{aligned} \tag{2.3}$$

where $\hbar$ is the reduced Planck's constant $\frac{h}{2\pi}$, m is the particle's mass, ∇^2 is the Laplace operator, and V is the potential energy at point r. This eigenvalue equation is known as the time-independent Schrödinger equation.

Solving this equation reveals the characteristics of the wave function. These characteristics are described by a set of quantum numbers: n, l, and m_l, giving the total energy of the atom, the angular momentum of the electron, and the orientation of the angular momentum, respectively. Additionally, experimental studies have resulted in the need for two more quantum numbers to better describe the characteristics of the particle: s and m_s, which gives the spin angular momentum of the electron and the orientation of the spin angular momentum, respectively.

2.2.2 Energy Levels

Solutions to the Schrödinger equation show that only specific energies are allowed. This quantisation of energies satisfies the condition that the electron may only exist in certain orbits. Furthermore, the orbits are split into sub-levels that are defined by the quantum numbers. The amount of sub-levels possible is dependent on the orbit, with higher numbered orbits having more sub-levels.

Figure 2.2 illustrates this division of energy levels for the hydrogen atom since it is the simplest case. Recalling that the electron may exist at an orbit,

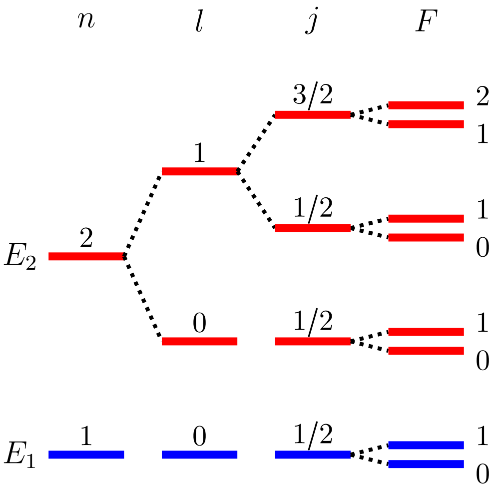

Figure 2.2: *Energy level digram for the hydrogen atom showing the energy levels and associated quantum numbers (n, l, j, and F) for the ground and first excited states, E_1 (blue) and E_2 (red). These energy levels are split further if the atom is perturbed by an external magnetic field.*

n, where n may be

$$n = 1, 2, 3, \ldots \; . \tag{2.4}$$

The orbiting electron has an angular momentum, L, which results in the splitting of each energy level into sub-levels. The orbital angular momentum of the electron is

$$L = \sqrt{l(l+1)}\hbar \; , \tag{2.5}$$

where l is the orbital angular momentum quantum number that characterises a specific sub-level. For a given n, l may take on values:

$$l = 0, \; \ldots, \; (n-1) \; . \tag{2.6}$$

The l sub-levels are typically referred to by the letter names given below, with the orbit as a prefix, for example 1s, 3p, or 5d (i.e. nl). In the case of hydrogen the 1s, 2s, and 2p sub-levels are present.

$l =$	0	1	2	3	4	5	6 ...
	s	p	d	f	g	h	i ...

The orbital motion of the electron results in a magnetic moment $\boldsymbol{\mu}_l$ given by

$$\boldsymbol{\mu}_l = -g_l \mu_B \mathbf{L} \; , \tag{2.7}$$

where g_l is a constant of proportionality and μ_B is the Bohr magneton.

When the atom is exposed to a magnetic field the orbital momentum vector may take on certain orientations in space, with each orientation constituting an energy sub-level. The orientation is specified by the z-component of the orbital angular momentum and is given by

$$L_z = m_l \hbar \tag{2.8}$$

where z is an arbitrarily chosen axis. This axis is usually chosen to be aligned with an external magnetic field. The magnetic quantum number m_l may assume the values

$$m_l = -l, \ \ldots, \ l \ , \tag{2.9}$$

with m_l increasing in integer steps.

In addition to the orbital angular momentum, electrons have an inherent spin which results in a spin angular momentum that is given by

$$\begin{aligned} S &= \sqrt{s(s+1)}\hbar \qquad (2.10) \\ &= \sqrt{\frac{1}{2} \cdot \frac{3}{2}}\hbar \\ &= \frac{\sqrt{3}}{2}\hbar \ , \qquad (2.11) \end{aligned}$$

where $s = 1/2$ is the spin quantum number.

As with the orbital momentum, the spin contributes a magnetic moment

$\boldsymbol{\mu}_s$ given by

$$\boldsymbol{\mu}_s = -g_s \mu_B \mathbf{S} \ , \tag{2.12}$$

where g_s is a constant of proportionality and μ_B is the Bohr magneton.

When the atom is exposed to a magnetic field the spin momentum vector may take on certain orientations in space. The orientation is specified by the z-component that is given by

$$S_z = m_s \hbar \tag{2.13}$$

where the m_s is the spin magnetic quantum number which may assume the values

$$m_s = -s, \ \ldots, \ s \ , \tag{2.14}$$

with m_s increasing in integer steps.

Fine Structure

We now consider an interaction known as the spin-orbit coupling, where the orbital angular momentum and spin angular momentum of the electron combine to give the total angular momentum. The interaction results in the splitting of energy levels into what is referred to as the fine structure.

The total angular momentum is

$$J = L + S \tag{2.15}$$

$$J = \sqrt{j(j+1)}\hbar \ , \tag{2.16}$$

where L and S are given in Equations (2.5) and (2.10), respectively, and j is the total angular momentum quantum number given by

$$\begin{aligned} j &= l + s \qquad (2.17) \\ &= l + 1/2 \\ j &= |l - s|,\ \ldots,\ |l + s|\ , \qquad (2.18) \end{aligned}$$

with j increasing in integer steps. For hydrogen this results in $j = 1/2$ for the $1s$ and $2s$ levels, and $j = 1/2$ and $j = 3/2$ for the $2p$ levels. Referencing of these sub-levels typically has the form nl_j (e.g. $2p_{3/2}$).

Since J is a combination of L and S, similarly, a magnetic moment $\boldsymbol{\mu}_j$ is present and is given by

$$\boldsymbol{\mu}_j = -g_j \mu_B \mathbf{J}\ , \qquad (2.19)$$

where g_j is a constant of proportionality and μ_B is the Bohr magneton.

As with L and S, the orientation in space is given by

$$J_z = m_j \hbar \qquad (2.20)$$

where the m_j is the spin magnetic quantum number which may assume the values

$$m_j = -j,\ \ldots,\ j\ , \qquad (2.21)$$

with m_j increasing in integer steps.

The difference in energy between two j sub-levels is given by

$$\Delta E = -\boldsymbol{\mu}_s \cdot \mathbf{B}_l \tag{2.22}$$

$$= \zeta \mathbf{L} \cdot \mathbf{S} \tag{2.23}$$

$$= \zeta \left[j(j+1) - l(l+1) - s(s+1) \right] /2 \ , \tag{2.24}$$

where $\mathbf{B}_l$ is the magnetic field produced by the orbiting electron which acts as a current loop and ζ is a proportionality constant. This equation normally includes a relativistic correction to the kinetic energy of the electron as well as the Darwin term, thus the energy will be different to Eq.2.24. However, the extra terms are omitted for clarity in this reduced fine structure model.

External Magnetic Fields

The orbital motion and spin of the electron are analogous to current loops which therefore generate magnetic fields. These internal magnetic fields interact with external magnetic fields, affecting the energy level structure we have just discussed.

Recalling that the orbital and spin moments of the electron may take on discrete orientations in space. For the orbital moment, the energy levels due to the orientations are specified by the value of the orbital magnetic quantum number m_l which ranges from $-l$ to l in steps of 1. For the spin moment, the energy levels are specified by value of the spin magnetic quantum number m_s which is $+1/2$ or $-1/2$. Similarly, the total orbital momentum may take on discrete orientations in space; the energy levels resulting from these orientations are specified by the total magnetic quantum number m_j which ranges in value from $-j$ to j in steps of 1.

Each orientation m_j constitutes a sub-level, however, these sub-levels for each j all appear to have the same energy and are called degenerate levels in the absence of an externally applied magnetic field. Only if an external magnetic field is present is the degeneracy removed. In the presence of a weak magnetic field the removal of degeneracy is known as the Zeeman effect. The removal of degeneracy by strong magnetic field is known as the Paschen-Back effect. In our experiment we only investigated the weak-field regime.

Hyperfine Structure

Finally we consider the interaction between the total angular momentum and the nuclear spin of the atom. Like the spin-orbit coupling, these moments combine to form the total momentum of the atom resulting in the division of the fine structure into hyperfine structure. The total momentum of the atom is given by

$$F = J + I \tag{2.25}$$

$$F = |j - I|\,,\ \ldots,\ |j + I|\ , \tag{2.26}$$

where J is given in Equation (2.15), I is the nuclear spin of the atom, and F increases in integer steps. In the case of hydrogen, $I = \frac{1}{2}$ therefore the $2p_{3/2}$ energy level has $F = 1$ and $F = 2$ hyperfine energy levels.

The Zeeman effect will cause the removal of the degeneracy in the z-component in the F sub-levels. The magnetic sub-levels are denoted by the quantum number m_F which may assume the values

$$m_F = -F,\ \ldots,\ F\ , \tag{2.27}$$

with m_F increasing in integer steps.

The difference in energy between two F sub-levels is given by

$$\begin{aligned} E &= a\mathbf{I}\cdot\mathbf{J} && (2.28)\\ &= \frac{a}{2}\left[F(F+1) - I(I+1) - J(J+1)\right]\ , && (2.29) \end{aligned}$$

with a being the magnetic dipole constant.

Magnetic Hyperfine Structure

When an atom is placed in a magnetic field the energy level structure is split into several magnetic sub-levels. These magnetic levels will have different energies. The shift in energy is given by

$$\Delta E = -\vec{\mu}\cdot\vec{B}\ , \tag{2.30}$$

where $\vec{\mu}$ is the magnetic dipole moment of the atom and $\vec{B}$ is the external magnetic field.

There are two cases to consider. The strong field where the internal magnetic field is very much smaller than the external magnetic field, and the weak field where the internal field is dominant.

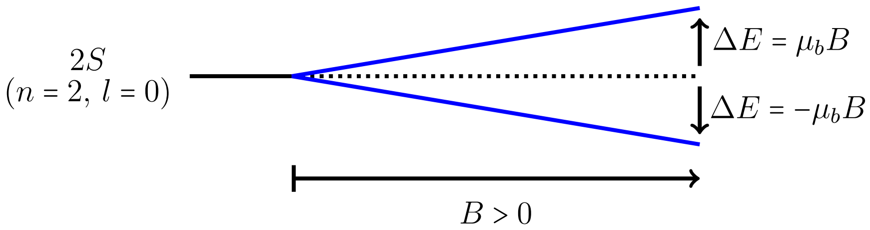

Figure 2.3: *A 2S ($n = 2$, $l = 0$) energy level split into two magnetic sub-levels (blue lines) separated by an energy difference ΔE of $\pm\mu_b B$ from the 2S level (solid and dotted black lines), due to an external magnetic field $\vec{B}$.*

Strong Field

In the presence of a strong magnetic field, $\vec{L}$ and $\vec{S}$ decouple and can be treated independently. The shift in energy is then

$$\begin{aligned}\vec{\mu}\cdot\vec{B} &= \vec{\mu}_l\cdot\vec{B} + \vec{\mu}_s\cdot\vec{B}\\ &= g_l\frac{\mu_b}{\hbar}\vec{L}\cdot\vec{B} + g_s\frac{\mu_b}{\hbar}\vec{S}\cdot\vec{B}\\ &= \frac{\mu_b}{\hbar}m_l\hbar B + 2\frac{\mu_b}{\hbar}m_s\hbar B \qquad (2.31)\\ &= \mu_b B(m_l + 2m_s)\ . \qquad (2.32)\end{aligned}$$

A given orbital (n, l) will therefore have an energy

$$E = E_n + \mu_b B(m_l + 2m_s)\ , \qquad (2.33)$$

where E_n is the unperturbed energy. This can be seen in Figure 2.3; the same applies to a 1s state[1].

---

[1] Note that since there is a breakdown of the spin-orbit coupling this energy level structure does not require that the fine structure be taken into account.

Table 2.1: *Magnetic levels and the associated energy shifts for a* $2P$ *state (*$n = 2$ *and* $l = 1$*).* m_l *and* m_s *are the orbital and spin magnetic quantum numbers, respectively.*

m_l	m_s	$(m_l + 2m_s)\mu_b B$
-1	-1/2	-2$\mu_b B$
-1	1/2	0$\mu_b B$
0	-1/2	-1$\mu_b B$
0	1/2	1$\mu_b B$
1	-1/2	0$\mu_b B$
1	1/2	2$\mu_b B$

For a $2P$ state ($n = 2$ and $l = 1$), we have

$$\begin{aligned} m_l &= -1, 0, 1 \\ m_s &= -\frac{1}{2}, \frac{1}{2} \\ E_{2,1} &= E_{2,1} + \mu_b B(m_l + 2m_s) \ . \end{aligned}$$

The magnetic levels for this state are given in Table 2.1 and illustrated in Figure 2.4.

In this discussion we have neglected the nuclear spin and hyperfine structure. This has been done in order to simplify the section that follows, in which we look more closely at the interaction between an atom and a weak external magnetic field.

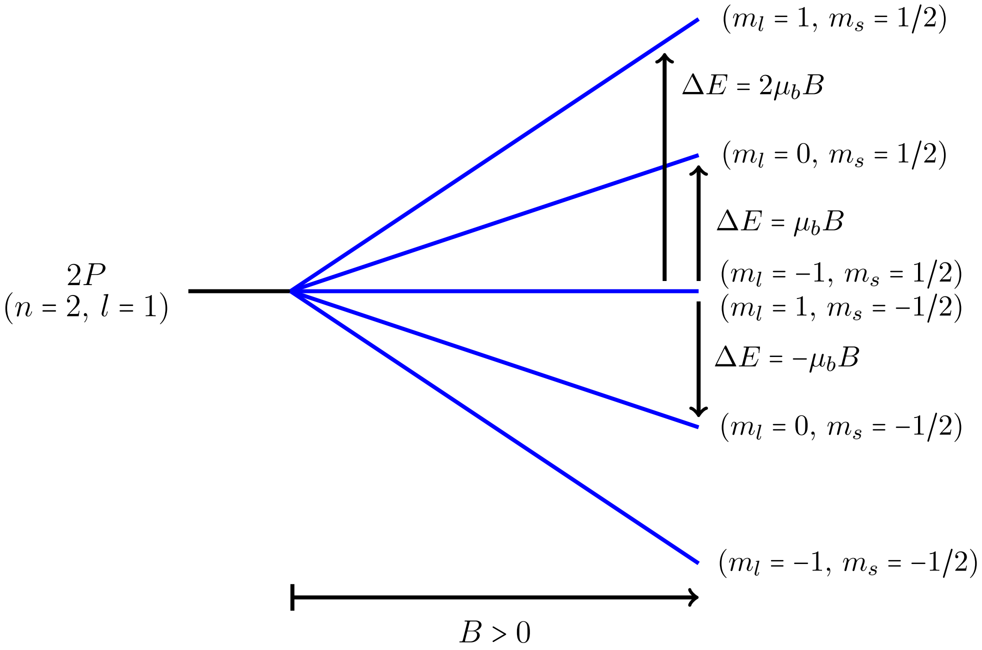

Figure 2.4: *A 2P ($n = 2$, $l = 1$) energy level split into six magnetic sub-levels (blue lines) separated by an energy difference ΔE from the 2P level (solid black line), due to an external magnetic field $\vec{B}$. Two of the six sub-levels are degenerate and have $\Delta E = 0$, this implies that they have the same energy as the 2P energy level when there is no external magnetic field.*

Weak Field

Here the internal field dominates causing the spin-orbit (LS) coupling to take place. The orbital and spin angular momenta couple to form a total angular momentum given by

$$\vec{J}' = \vec{L}' + \vec{S}' \ , \tag{2.34}$$

with $\vec{L}'$ and $\vec{S}'$ being the vector sum of all $\vec{L}$ and $\vec{S}$, respectively, in the case of multi-electron atoms. Contrary to the strong field regime discussed previously, the fine structure must now be taken into account since the LS-coupling is present. To simplify this discussion the nuclear spin and hyperfine structure have not been considered.

For the shift in energy,

$$\Delta E = -\vec{\mu} \cdot \vec{B} \ ,$$

we now need the average component of $\vec{\mu}$ along $\vec{B}$.

Let's examine the behaviour of $\vec{\mu}$. The discussion here follows that given in Eisberg and Resnick (1985b). Figure 2.5 shows the $\vec{L}'$, $\vec{S}'$, and $\vec{J}'$ vectors, these vectors always lie on the same plane. L' and S' precess about J'. The precessional frequency is rapid, and is proportional to the internal magnetic field B_{int}.

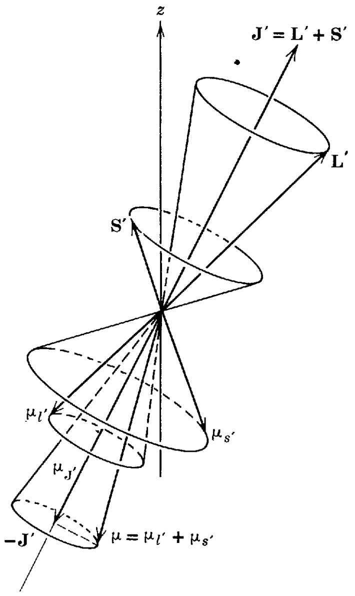

Figure 2.5: *Orbital momentum $\vec{L}'$ and spin $\vec{S}'$ couple to form the total angular momentum $\vec{J}'$ of an atom. Similarly, the dipole moments $\vec{\mu}_{l'}$ and $\vec{\mu}_{s'}$ also couple to form $\vec{\mu}$. (Adapted from Eisberg and Resnick (1985b))*

$\vec{\mu}$ lies in the precessional plane and precesses about J' with a precessional frequency that is proportional to the internal magnetic field. In the presence of an external magnetic field B_{ext}, $\vec{\mu}$ will also precess about the external field. However, this precession is slow since the external field is much smaller than the internal field (i.e. $B_{ext} << B_{int}$).

Recall that

$$\begin{aligned} \Delta E &= -\vec{\mu} \cdot \vec{B} \\ &= -\mu_B B \ , \end{aligned} \tag{2.35}$$

with μ_B being the average component of $\vec{\mu}$ along $\vec{B}$. Since $\vec{\mu}$ precesses rapidly about J', we first find the component of $\vec{\mu}$ along J' ($\mu_{J'}$),

$$\begin{aligned} \mu_{J'} &= \mu \cos\theta \ ... \ \theta = \text{angle between } \vec{\mu} \text{ and } \vec{J}' \\ &= \mu \frac{\vec{\mu} \cdot \vec{J}'}{\mu J'} \ ... \ \vec{\mu} = -\frac{\mu_b}{\hbar}(g_l L' + g_s S') \\ &= -\frac{\mu_b}{\hbar} \frac{(\vec{L}' + 2\vec{S}') \cdot (\vec{L}' + \vec{S}')}{J'} \end{aligned} \tag{2.36}$$

Then μ_B is given by,

$$\begin{aligned}
\mu_B &= \mu_{J'} \cos\theta_z \text{ ... } \theta_z = \text{angle between } \vec{\mu_{J'}} \text{ and } \vec{B} \\
&= \mu_{J'} \frac{\vec{J'} \cdot \vec{B}}{J'B} \\
&= \mu_{J'} \frac{J_z}{J'} && (2.37) \\
&= -\frac{\mu_b}{\hbar} \frac{(\vec{L}' + 2\vec{S}') \cdot (\vec{L}' + \vec{S}')}{J'} \frac{J_z}{J'} \\
&= -\frac{\mu_b}{\hbar} \frac{(\vec{J}' + \vec{S}') \cdot \vec{J}' J_z}{J'^2} \\
&= -\frac{\mu_b}{\hbar} \frac{(\vec{J}'^2 + \vec{J}' \cdot \vec{S}') J_z}{J'^2} && (2.38)
\end{aligned}$$

where

$$\begin{aligned}
J &= L + S \\
J^2 &= L^2 + S^2 + 2\vec{L} \cdot \vec{S} \\
\vec{J} \cdot \vec{S} &= \vec{L} \cdot \vec{S} + S^2
\end{aligned}$$

So

$$\begin{aligned}
\mu_B &= -\frac{\mu_b}{\hbar} \frac{(J'^2 + \vec{L}' \cdot \vec{S}' + S'^2) J_z}{J'^2} \\
&= -\frac{\mu_b}{\hbar} \frac{(J'^2 + (J'^2 - L'^2 - S'^2)/2 + S'^2) J_z}{J'^2} \\
&= -\frac{\mu_b}{\hbar} \frac{(3J'^2 - L'^2 + S'^2) J_z}{2J'^2} && (2.39)
\end{aligned}$$

Therefore

$$
\begin{aligned}
\Delta E &= -\vec{\mu} \cdot \vec{B} \\
&= -\mu_B B \\
&= \frac{\mu_B B}{\hbar} \frac{(3J'^2 - L'^2 + S'^2) J_z}{2J'^2} \\
&= \frac{\mu_B B}{\hbar} \frac{[3j'(j'+1) - l'(l'+1) + s'(s'+1)]\, m_j \hbar^3}{2j'(j'+1)\hbar^2} \\
&= \frac{\mu_B B}{\hbar} \frac{[3j'(j'+1) - l'(l'+1) + s'(s'+1)]\, m_j \hbar^3}{2j'(j'+1)\hbar^2} \\
&= \mu_B B m_j \left[\underbrace{1 + \frac{j'(j'+1) - l'(l'+1) + s'(s'+1)}{2j'(j'+1)}}_{\mathrm{g}} \right] \qquad (2.40)
\end{aligned}
$$

with g being the Landé factor.

A theoretical and computational analysis of the magnetic energy levels of rubidium 85 and rubidium 87 is given in Appendix A; this was done using an advanced technique described in Pethick and Smith (2008). This is a more complete analysis as it includes the nuclear spin and hyperfine structure of the atoms.

2.2.3 Summary of Quantum Numbers

All of the atomic energy levels discussed above can be described using a set of quantum numbers, Table 2.2 summarises the quantum numbers of this discussion.

Table 2.2: *Quantum Numbers used to define an atomic state. Here n is an integer value more than 0, l may be integer values from 0 to $(n-1)$, m_l may be integer values from $-l$ to 0 to $+l$, s is $\frac{1}{2}$, m_s is either $-\frac{1}{2}$ or $+\frac{1}{2}$, J depends on l and s, m_j may be integer values from $-j$ to 0 to $+l$, I depends on the atom, F depends on j and i, and m_f may be integer values from $-F$ to 0 to $+F$.*

Name	Symbol	Description
Principal	n	Energy
Orbital	l	Orbital angular momentum
Orbital magnetic	m_l	Orientation of L
Spin	s	Spin angular momentum
Spin magnetic	m_s	Orientation of S
	j	Total angular momentum of the electron
	I	Total angular momentum of the nucleus
	m_j	Orientation of J
	F	Total angular momentum
	m_f	Orientation of F

2.2.4 Absorption and Emission

An electron is able to undergo electronic transitions from lower to higher states by absorbing energy from particles (i.e. photons) it interacts with. The electron can only exist in an excited state for a finite period before decaying back to a lower state, usually the ground state. When this occurs, the atom releases energy in the form of a photon. These processes are known as absorption and emission. In addition, atoms may undergo stimulated emission whereby an atom interacts with a photon and decays from an excited state to a lower state, emitting a photon in the process.

Due to the quantised energy levels, atoms will only absorb or emit energies which are equal to the difference in energy between any two states. However, absorption could still occur when the energy is not exactly equal to the

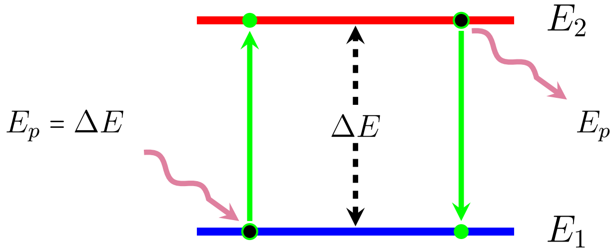

Figure 2.6: *Atom-light interaction of a one-electron atom.* E_p *is the photon energy and* ΔE *is the excitation energy between the* E_1 *and* E_2 *states.*

difference between any two states if Heisenberg's uncertainty principle is satisfied.

2.2.5 Atomic Transition Selection Rules

When atom undergoes a transition between states there are no limits regarding the change in the principal quantum number n, however, any change in the other quantum numbers should satisfy the following conditions:

- the orbital angular momentum quantum number: $\Delta l = \pm 1$
- the magnetic quantum number: $\Delta m_l = 0, \pm 1$
- the total angular momentum quantum number: $\Delta j = 0, \pm 1$
- the total momentum quantum number: $\Delta F = 0, \pm 1$

Transitions which violate the above rules are called forbidden transitions. Forbidden transitions do occur but have a very low probability of occurrence.

2.2.6 Atom-Light Interactions

Atoms are able to interact with particles, we discuss here the interaction with photons in free space. Each photon has an associated energy

$$E = \hbar\omega \tag{2.41}$$

and momentum

$$p = \hbar k\,, \tag{2.42}$$

where ω is the angular frequency $2\pi f$, and k is the wave number $\frac{2\pi}{\lambda}$. Since $f = \frac{c}{\lambda}$, the energy and momentum are dependent only on the frequency of the emitted light.

Figure 2.6 illustrates the light-atom interaction for a one-electron atom when considering only the first two energy states. A photon travels towards an atom that is in the ground state E_1 and the photon is of energy

$$E_p = \Delta E = E_2 - E_1\ , \tag{2.43}$$

thereby meeting the condition that the energy must equal the difference in energy between two levels. The atom now absorbs this photon with its energy and momentum and the electron undergoes a transition into the excited state E_2, while the atom's momentum increases. The atom eventually decays to the ground state, emits a photon of energy ΔE and recoils in a random direction.

2.3 Cooling and Trapping of Atoms

Although the current research does not involve the generation or study of cold atoms, planned future experiments will require cold atoms. These experiments involve the study of quantum systems, such as quantum computers, that are sensitive to decoherence and thermal degradation which can be reduced by cooling the atoms to sub-Kelvin temperatures. We plan to use the Doppler cooling method in future experiments as this is a common starting point for cooling atoms to sub-kelvin temperatures. This section briefly explains the process of Doppler cooling with hydrogen as the atom to be cooled.

A hydrogen atom is constrained to move in one dimension, as shown in figure 2.7. This atom has momentum in the negative direction (to the left)

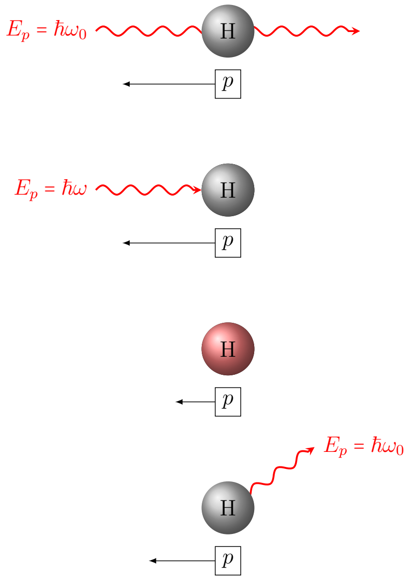

Figure 2.7: *Doppler cooling of the Hydrogen atom, where* p *is the momentum,* E_p *is the photon energy,* $\hbar\omega_0$ *is the resonant frequency of the atom, and* $\hbar\omega$ *is the Doppler shifted resonant frequency of the atom.*

and is at the lowest energy level E_1. A laser produces photons which interact with the atom, these photons have momentum in the positive direction (to the right) and an energy E matching the lowest electronic transition energy $\hbar\omega_0$ of the atom. Since the momenta are in opposing directions, the photon energy is perceived by the atom to be higher than the transition energy due to the Doppler effect

$$f_{photon} = f_{transition}\left(1 + \frac{v_{atom}}{c}\right) \ . \tag{2.44}$$

This apparent increase in energy of the photon disallows the required transition from occurring. To counteract the Doppler shift the photon energy must be adjusted accordingly; this is achieved by decreasing the frequency of the laser away from the atomic resonant frequency and is known as red detuning. Although the laser frequency is lower, the atoms sees a frequency matching its resonant frequency and absorption occurs.

During absorption, the momentum of the atom is reduced by an amount equivalent to the momentum of the photon. Thereafter, the atom undergoes spontaneous emission and experiences a recoil in a random direction. Since this direction is random, the net change in the momentum of the atom due to recoil over multiple absorption cycles is negligible. The momentum of a gas of such atoms is related to the thermal energy by

$$E_{thermal} = \frac{1}{2}Nm\bar{v}^2 = \frac{3}{2}NK_BT \ , \tag{2.45}$$

where N is the number of atoms, $\bar{v}$ is the average velocity of atoms, K_B is the Boltzmann constant, and T is the temperature of the atoms. A reduction in the momentum during absorption is therefore equivalent to a reduction of the temperature of the gas of atoms.

Any reduction in momentum, however, results in a reduction of the Doppler shift. The laser detuning must therefore be reduced continuously in order to maintain matching of the photon and absorption energies.

Specific atomic transitions, known as cooling and repumping transitions must be excited during the process of Doppler cooling atoms. During this process, the atom is exited through the cooling transition. However, there is a probability that the atom will decay to an energy level that is not resonant with the laser frequency. In this case, a secondary laser that is detuned to the frequency of the transition that is not resonant with the primary laser, the repumping transition, is used to excite the atom back to the energy level that is resonant with the primary laser frequency.

2.4 Laser Frequency Locking

To ensure the laser is kept in resonance with an atomic transition during Doppler cooling it is necessary to lock the laser frequency to that transition using a feedback control system. The basic block diagram of the system is shown in Figure 2.8. The system consists of the following:

Laser

This is a diode laser where the current can be modulated, which in turn alters the power and frequency of the laser light. The diode is placed inside a cavity where the length can be controlled via a piezoelectric actuator, which in turn alters the frequency of the light.

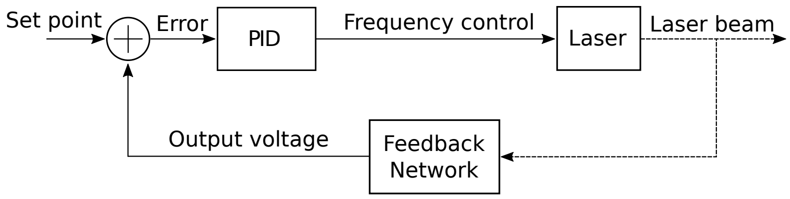

Figure 2.8: *Laser frequency control system. The system consists of a proportional-integral-derivative (PID) controller, a laser, and a feedback network. The solid arrows indicate voltage signals and the dashed arrows represent laser light.*

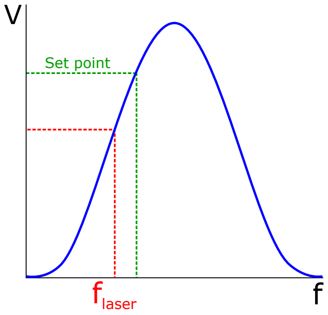

Figure 2.9: *Frequency response of the feedback network (blue curve). The green dashed line indicates the point on the response curve at which the laser frequency should be maintained, corresponding to the set point. The red dashed line indicates the point on the response curve that corresponds to the output voltage of the feedback network due to the laser frequency.*

Feedback Network

A small portion of the laser light is sent to a feedback network where the frequency response is known. The output is a voltage that is proportional to where the frequency of the input light lies on the frequency response curve of the feedback network shown in Figure 2.9. This output signal is compared to a set point signal, which is a point on the frequency response curve where we want the laser frequency to be maintained at, and the difference between the output of the feedback network and set point is known as the error signal.

Proportional-Integral-Derivative Controller

The error signal is fed into a Proportional-Integral-Derivative (PID) controller and the output is used to control the laser in a way which ensures that the output of the feedback network and the set point are the same value, thus reducing the error to zero which means that the laser is locked.

In Chapter 3 we describe the setup of the laser frequency locking system and provide a description of the techniques used to lock the laser frequency.

2.5 Absorption Spectroscopy

In our experiments absorption spectroscopy is used to observe the energy levels of rubidium. By detecting changes in power of the laser beam as it is passed through a sample of rubidium gas, we are able to measure the separation of energy levels. Absorption spectroscopy is critical to the laser locking system and Doppler cooling process, and the understanding of the research as a whole.

Shown in Figure 2.10 is the arrangement for standard absorption spectroscopy, and Figure 2.12 shows a basic arrangement for saturated absorption spectroscopy which is used to counteract the Doppler broadening of the absorption lines due to the thermal motion of atoms.

In the basic absorption spectroscopy experiment setup, a laser beam is directed through the gas and then detected by a photodetector, as shown in Figure 2.10. Since the absorption frequencies of the atom are initially unknown, the laser frequency is swept across a wide range to ensure all

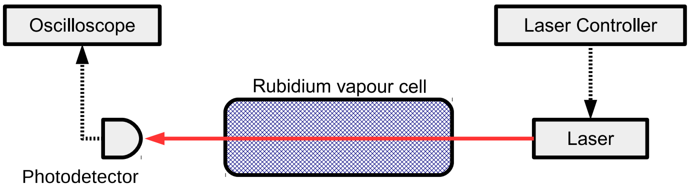

Figure 2.10: *Absorption spectroscopy setup.*

possible resonant frequencies are identified. By detecting changes in beam intensity due to absorption and by knowing the frequency of the photons that are absorbed by the atoms, we can describe the absorption spectrum of an atom. The beam intensity is plotted as a function of frequency which results in the absorption spectrum.

Most spectroscopy experiments involve room-temperature atoms. The atoms therefore have thermal motion and their velocity distribution is given by the Maxwell-Boltzmann probability distribution

$$\rho(v_{atom}) = \sqrt{\frac{m}{2\pi k_B T}}\, e^{\left(\frac{m v_{atom}^2}{2k_B T}\right)} , \tag{2.46}$$

where m is the mass of the atom, K_B is Boltzmann's constant, and T is the temperature in kelvins. The mean velocity of the atoms is described by

$$\bar{v} = \sqrt{\frac{3K_B T}{m}} . \tag{2.47}$$

This thermal motion results in a Doppler broadened spectrum which hides the hyperfine energy levels. The Doppler broadening is due to the velocity dependent absorption by atoms which can be explained as follows.

If all the atoms in a given sample have no velocity component along the

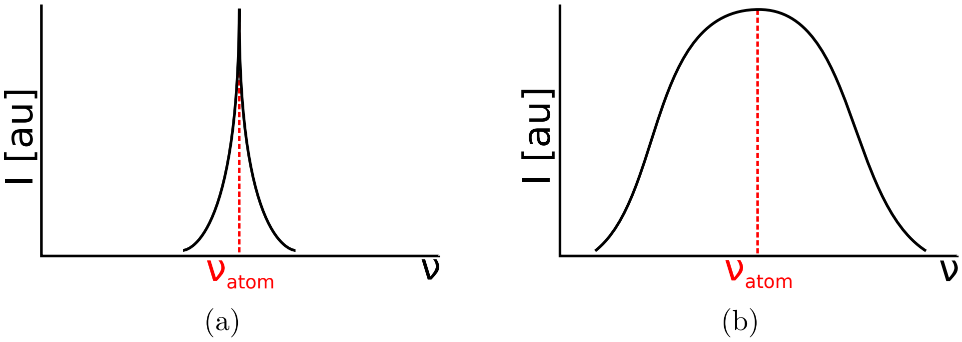

(a) (b)

Figure 2.11: *(a): Absorption spectrum showing natural linewidth of a hyperfine transition. (b): Absorption spectrum showing the broadening of the linewidth due to the Doppler-shifted laser light frequency, to the point where no hyperfine absorption line is visible.*

axis of beam propagation, as the wavelength is modulated from a low frequency to a high frequency, atoms that observe the beam to be in resonance should absorb the photons. The resulting measurement should show absorption only at certain frequencies as shown in Figure 2.11a. However, this is not the case at room temperature; here, atoms have thermal motion and those with motion in the direction of the beam observe an increase in frequency of the beam while atoms moving in the opposing direction observe a decrease in frequency. This Doppler-shifted frequency is given by

$$\nu_{Doppler} = \nu_{laser}(1 - \frac{v_{atom}}{c}) \ , \tag{2.48}$$

where ν_{laser} is the frequency of the beam, v_{atom} is the velocity of the atom in the direction of beam propagation, and c is the speed of light in vacuum. These moving atoms observe the beam to be continuously Doppler shifted into resonance as the frequency is modulated.

The Maxwell-Boltzmann velocity distribution of the atoms results in a Doppler broadened absorption profile as shown in Figure 2.11b. This Doppler broadened curve is centred about the resonant frequency for an energy level transition of an atom ν_{atom} and described by the Gaussian function

$$f = e^{-\frac{(\nu - \nu_{atom})^2}{2\sigma^2}} \,, \tag{2.49}$$

with σ as the reciprocal of the lifetime of the excited state, and ν_{atom} as the resonant frequency for the transition. The full-width half maximum of this Doppler broadened curve is given by

$$\Delta\nu_{Doppler} = 2\nu_{atom}\sqrt{\frac{2k_B T ln2}{mc^2}} \,. \tag{2.50}$$

At room temperature this is approximately 500 MHz for rubidium, which is larger than the total energy level separation for the excited state hyperfine levels, thus hiding the natural absorption lines (Figure 2.11a).

To circumvent Doppler broadening, a technique known as saturated absorption spectroscopy (SAS) is implemented which extracts the absorption spectrum from atoms with zero velocity only. This is achieved by isolating the zero velocity atoms from the background via a strong pump beam, and having a weaker counter-propagating probe beam interact with the zero velocity atoms; the beams are shown in Figure 2.12. The net effect of the pump beam and probe beam is a reduction in absorption, as the laser frequency is swept, corresponding only to the atoms of zero velocity which interact with both beams. This reduction is due to the fact that when the probe beam and pump beam are in resonance with the zero velocity atoms, they interact with the same group of atoms. However, the pump beam being very much stronger causes saturation of the sample which means that the number of atoms in the excited state is equal to the number of atoms in the ground

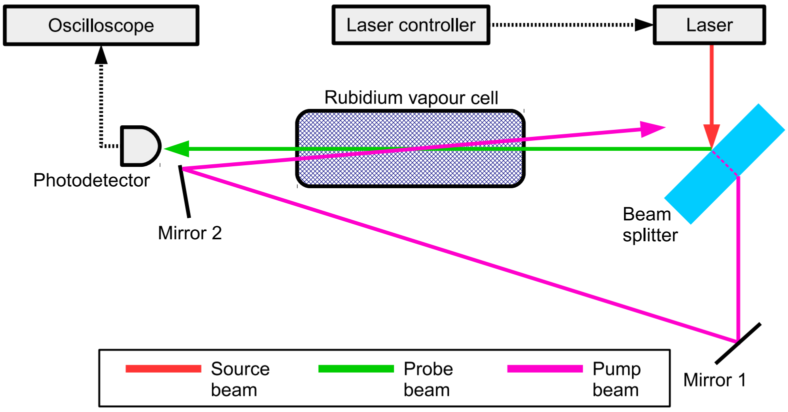

Figure 2.12: *Basic saturated absorption spectroscopy setup*

state. This leaves fewer atoms to interact with the probe beam which results in a reduction in absorption. When the beams are off resonance with the zero velocity atoms, they interact with different groups of atoms since they propagate in opposing directions. The Doppler shift is different for these beams, thus there is no saturation effect observed by the probe beam (Wilson and Hawkes, 1987).

When the probe beam and pump beam are in resonance with the same group of atoms, the resulting saturated absorption spectrum should then have the absorption lines of hyperfine transitions superimposed upon the peak of the Doppler broadened curve as shown in Figure 2.13. These absorption lines approach the natural linewidth of the transition which is given by the Lorentzian function

$$f = \frac{\gamma^2}{(\nu - \nu_{atom})^2 + \gamma^2} \ , \tag{2.51}$$

with γ as the reciprocal of the lifetime of the excited state, and ν_{atom} as the resonant frequency for the transition.

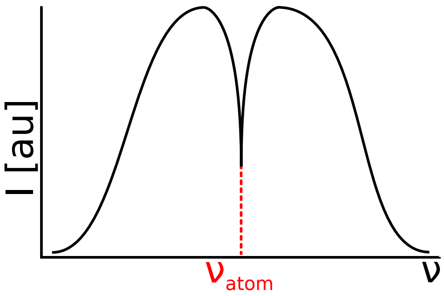

Figure 2.13: *Saturated absorption spectrum showing a hyperfine absorption line superimposed upon the peak of the Doppler-broadened curve.*

Calibration of Absorption Measurements

In saturated absorption spectroscopy we measure the intensity of the probe beam as the laser frequency is varied in time and we obtain a signal from the photodetector as a function of time. In order to quantify absorption measurements, it is necessary to convert the time axis to a frequency axis. The calibration of the time axis of each absorption signal into a frequency axis is performed using the Michelson interferometer in Figure 2.14. The Michelson interferometer is comprised of two mirrors and a beam splitter. Operation of the Michelson interferometer is as follows. A source beam is split using a beam splitter, the resulting beams now travel along separate paths to their respective mirrors and are reflected back to the beam splitter. The beams are then recombined which results in the two beams interfering with each other constructively or destructively.

Considering this process in terms of waves, for constructive interference the beams must be in phase which implies the following relation must be satisfied

$$\Delta d = n\lambda \ , \tag{2.52}$$

where Δd is the difference between the two paths of the interferometer ($2\,(L2 - L1)$ in Figure 2.14), and n is an integer. For destructive interference the beams must be one half of a wavelength out of phase so a similar relation must be satisfied

$$\Delta d = (n + 1/2)\lambda\ . \tag{2.53}$$

Typically, the Michelson interferometer is setup in a manner that allows one of the mirrors to be moved along the axis of beam propagation. This enables the user to vary the difference in distance from the mirror to the beam splitter between the two paths of the interferometer which leads to a variation in the phase offsets of the two beams, resulting in a variable interference. If the mirrors are aligned so that the beams are overlapping in both the vertical and horizontal axes then the interference shows up as a series of light and dark central spots at the output, as seen in Figure 2.14. If not, then the result is a series of light and dark parallel lines; the former being more favourable.

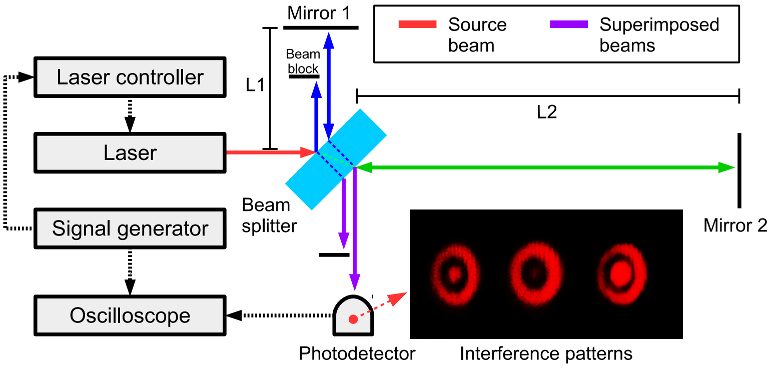

Figure 2.14: *Michelson interferometer setup with the output illustrated using an actual interference pattern produced by our experimental setup.*

By moving the mirror a known displacement and by counting the amount of times that a specific spot or line in the interference pattern has changed from light to dark to light, one can estimate the wavelength of the source beam. The relationship is given by

$$d = m\lambda \ , \tag{2.54}$$

where d is the distance that the mirror has been displaced and m is the amount of times that the spot or line has cycled from light to light.

In the case where the laser frequency is swept linearly, the two beams interfere constructively and destructively without the need for a movable mirror. If the mirrors are aligned so that the beams are overlapping in both the vertical and horizontal axes then the interference shows up as a series of light and dark central spots on the output detector, as seen in Figure 2.14. If not, then the result is a series of light and dark parallel lines; the former being more favourable. The resulting signal is sinusoidal, varying in amplitude as the interference pattern cycles through high and low intensities. The maxima correspond to constructive interference. By measuring the distance between two maxima we can calibrate the time into frequency, as discussed in Chapter 4.

2.6 Properties of Rubidium

Since we will be investigating rubidium, we should highlight some facts about this element. Rubidium is naturally composed of two isotopes, 87 and 85; rubidium 85 is more abundant, making up 72% of the population. It is an alkali metal, placing it in the first column (group 1) of the periodic table. It

Table 2.3: *Physical and optical properties of rubidium for the* $5S_{1/2} \rightarrow 5P_{3/2}$ *transition (Steck, 2015; Steck, 2013).*

Property	Symbol	Value
Atomic mass (^{85}Rb)	m	1.409993199 x 10^{-25} Kg
Atomic mass (^{87}Rb)	m	1.443160648 x 10^{-25} Kg
Atomic Number	Z	37
Nuclear spin (^{85}Rb)	I	5/2
Nuclear spin (^{87}Rb)	I	3/2
Ionisation energy (^{85}Rb)	E_I	4.17712633 eV
Ionisation energy (^{87}Rb)	E_I	4.17712706 eV
Wavelength (^{85}Rb)	λ_{vacuum}	780.241368271 nm
Wavelength (^{87}Rb)	λ_{vacuum}	780.241209686 nm
Lifetime	τ	26.2348 ns

has 37 electrons, one of which is a valence electron in the $5S$ orbital. A more comprehensive characterisation of rubidium is provided in table 2.3.

2.7 Summary

We have discussed all the general theory related to the research in this thesis. Although the theory covered here should be sufficient for readers to follow the chapters going forward, this chapter covers a wide range of topics and so most aspects will be repeated or referenced in the chapters that follow.

Chapter 3

Experimental Setup

3.1 Introduction

This chapter describes the experimental setup used to measure both the hyperfine and magnetic hyperfine absorption spectra of rubidium 85 and rubidium 87. This was achieved using a saturated absorption spectroscopy setup which included a pair of Helmholtz coils for generating a uniform magnetic field across the rubidium vapour cell.

Additionally, a laser locking setup was included to lock the laser at specific transitions in the absorption spectra. To lock the laser we made use of a proportional-integral-derivative controller and a lock-in amplifier.

3.2 Saturated Absorption Spectroscopy Setup

Two different saturated absorption spectroscopy arrangements were used to measure the absorption spectra of rubidium (Rb). Each arrangement consisted of an external cavity diode laser, Rb vapour cell, photodetectors, and optical components to route the beams. A portion of the light from the laser was sent to a Michelson interferometer in order to calibrate the absorption measurements.

To measure the Zeeman spectra of Rb, the Rb vapour cell was placed between a pair of Helmholtz coils. This was only applicable to one of the arrangements that are discussed below.

3.2.1 Saturated Absorption Spectroscopy Arrangements

The key difference between the two arrangements is the way in which the probe and pump beams overlap. Arrangement 2 provides maximum overlap whereas arrangement 1 is partial. As explained in Chapter 2.5, this overlap is crucial in circumventing the Doppler broadening of absorption lines.

Figures 3.1 and 3.2 show arrangement 1 of our saturated absorption spectroscopy (SAS) setup. This arrangement was used initially as we lacked certain optical elements required for more complex arrangements. In fact, many of the mechanical parts used in this arrangement were custom made. For this arrangement a source beam was passed through an optical isolator and split into two beams, one for the SAS setup and one for a Michelson interferometer. The beam for the SAS setup was then split into three beams, two weak probe beams (blue and green) and one intense pump beam (pink). The probe beams are labelled as signal (green) and reference (blue) beams, reasons for the names are discussed in Chapter 2.5.

The green and blue beams pass through the Rb vapour cell and are monitored by a pair of photodetectors. The pink beam is routed in such a way that

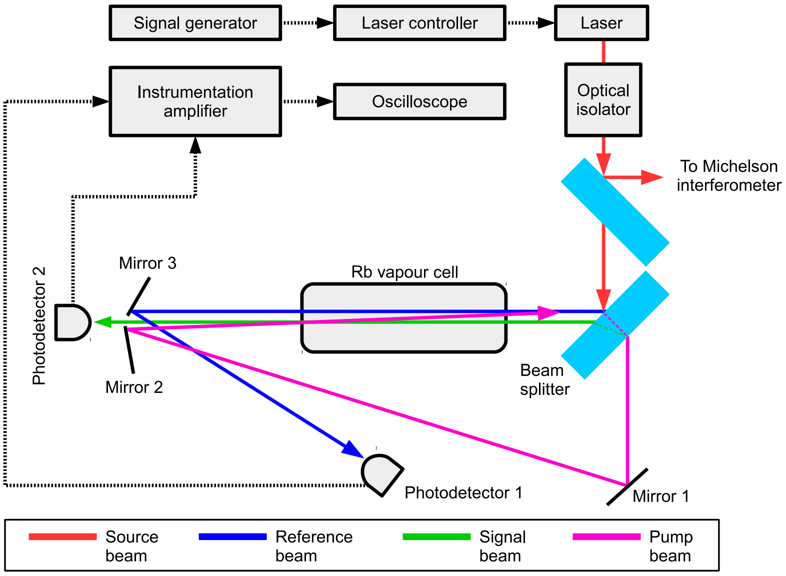

Figure 3.1: *Arrangement 1 of our saturated absorption spectroscopy setup. Pump and probe (reference and signal) beams overlap within a small region of the rubidium vapour cell.*

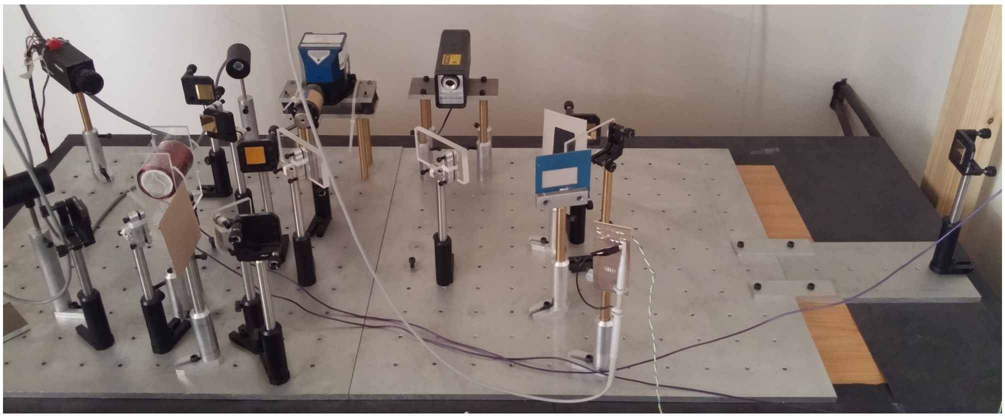

Figure 3.2: *Arrangement 1 of our saturated absorption spectroscopy (SAS) setup in the laboratory. Two aluminium base plates are seen: the left plate is the SAS setup and the right is the Michelson interferometer. A helium-neon laser is included in the setup to perform beam alignment.*

it overlaps and counter-propagates the green beam within the Rb vapour cell.

Figures 3.3 and 3.4 show arrangement 2 of our SAS setup. In this ar-

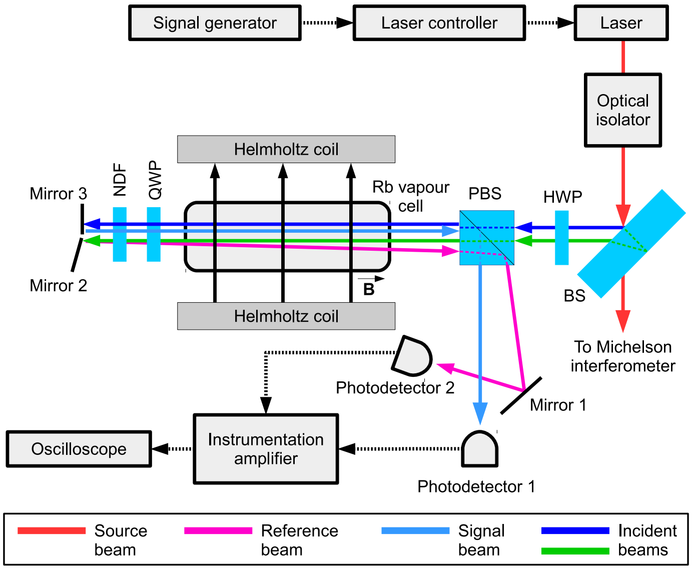

Figure 3.3: *Arrangement 2 of our saturated absorption spectroscopy setup. Pump and probe beams overlap throughout the rubidium vapour cell. The direction of the magnetic field $\vec{B}$ is indicated by the arrows across the Rb vapour cell. Abbreviations: half-wave plate (HWP), beam splitter (BS), polarising beam splitter (PBS), quarter-wave plate (QWP), and neutral density filter (NDF).*

rangement a source beam was passed through an optical isolator and split into three beams, two incident beams (dark blue and green) for the SAS setup and one beam for a Michelson interferometer (red).

A half-wave plate (HWP) in conjunction with a polarising beam splitter (PBS) was used to pick out the linearly polarised component of the dark blue and green beams. These beams then pass through the Rb vapour cell, undergo a 45 degree rotation of the polarisation via the quarter-wave plate (QWP), and get attenuated by a neutral density filter (NDF). Both beams are then reflected which results in further attenuation and another 45 degree rotation of the polarisation. The beam reflected by mirror 3 now acts as a signal beam (light blue) which overlaps the dark blue beam throughout

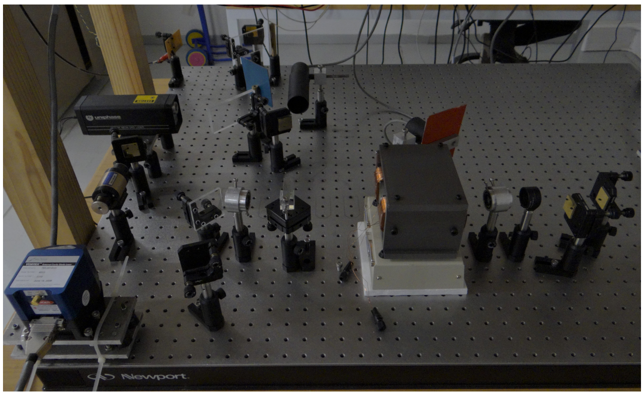

Figure 3.4: *Arrangement 2 of our saturated absorption spectroscopy setup in the laboratory. A helium-neon laser is included in the setup to perform beam alignment.*

the Rb vapour cell. This is identical to the pump (pink) and signal (green) beams which overlap in arrangement 1 (Figure 3.1). The beam reflected by mirror 2 acts as a reference beam (pink) and is offset to ensure it does not overlap the green beam inside the Rb vapour cell. The light blue and pink beams have opposite polarisations to the dark blue and green beams. The blue and pink beams are thus reflected by the polarising beam splitter toward photodetectors for monitoring.

For the Zeeman study, arrangement 2 had the Rb vapour cell placed between a pair of Helmholtz coils. These coils were used to generate a uniform magnetic field in the region of the Rb vapour cell.

3.2.2 Michelson Interferometer

Figure 3.5 shows a diagram of our Michelson interferometer setup. Here we have a portion of the light from the saturated absorption spectroscopy setup split into two beams by a beam splitter. The two beams travel along paths of different lengths before being reflected back to the beam splitter. The beams

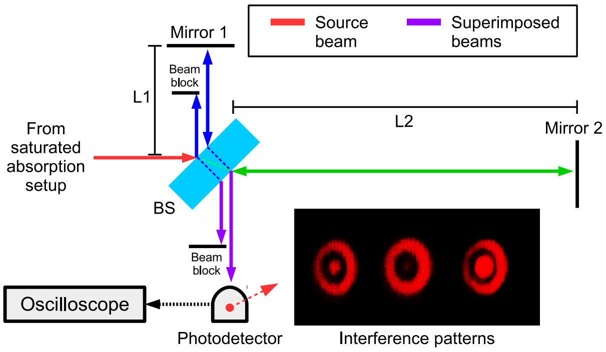

Figure 3.5: *A Michelson interferometer setup. The output is illustrated using photographs of interference patterns that have been observed in our lab. Changes in the pattern are due to variations in the wavelength of the beam, or acoustic vibrations which change the length of each path.*

are then recombined and the resulting beam is monitored by a photodetector. The monitored beam is an interference pattern dependent on the wavelength of the source beam; if the wavelength varies, the resulting beam will undergo constructive and destructive interference. Variations in path length due to acoustic vibration will result in wave interference as well.

For optimal performance the Michelson interferometer must have the mirrors aligned such that the two beams combine and propagate along the same line in the vertical and horizontal planes. The resulting interference pattern is a set of rings as seen in Figure 3.5. As we will discuss later, this interference pattern is used in calibrating the absorption measurements.

Before discussing the operation of the SAS experiment, a description of the major components is given.

3.2.3 External Cavity Diode Laser

An external cavity diode laser (ECDL) is a tunable diode laser with an external cavity that allows for fine adjustments of the output wavelength, the ECDL is shown in figure 3.6. Wavelength tuning is achieved using a piezoelectric actuated mirror and a diffraction grating. The piezoelectric actuator is controlled using an external modulation signal. The effect of the piezoelectric actuator is to alter the cavity length thus altering the resonant frequency. This mechanism allows for fine control of the wavelength but the tuning range is narrow. Due to this method of tuning being mechanical, it is generally best to use this method for reducing low frequency changes in wavelength.

Additional tuning is possible by modulating the current supplied to the laser diode. This is useful for finer and faster adjustments to the wavelength when compared to piezoelectric actuator modulation, and is thus more suited

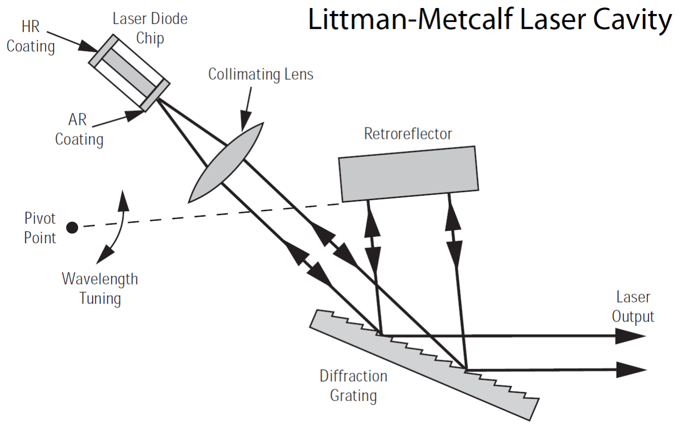

Figure 3.6: *A Littman-metcalf type external cavity diode laser as used in our setup. The retroreflector and grating are used to tune the wavelength of the emitted light. HR and AR coatings refer to highly-reflective and anti-reflective coatings respectively. (Adapted from* User's Guide 7000/6000 Series Tunable Diode Laser *n.d.).*

to reducing high frequency changes in wavelength. The diode current is controlled using an external modulation signal.

The central wavelength of the laser used in our experiment is 780.24 nanometres (nm) and the tuning range is less than one nanometre. This laser is used to probe electronic transitions within the $5S_{1/2}$ and $5P_{3/2}$ states of rubidium 85 ^{85}Rb and rubidium 87 ^{87}Rb.

We measured the power of the beam from the laser at various laser diode current settings, over the full current range. The power meter was positioned approximately 6 cm from the aperture on the laser head, after an optical isolator. The resulting laser beam power versus laser diode current curve is given in Figure 3.7.

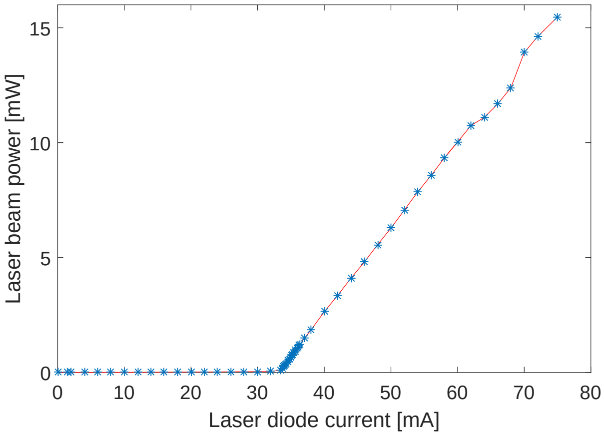

Figure 3.7: *Laser beam power measured at various laser diode current settings. At approximately 33 mA the laser begins to lase and the curve remains linear thereafter.*

3.2.4 Optical Isolator

An optical isolator (OI) is used to prevent optical feedback into the cavity of the ECDL. Light returning to the laser cavity disturbs the operation of the laser resulting in an unstable output. The operation of the OI results in an output beam that has a well defined polarisation state.

The optical isolator consists of two polarisers and a Faraday rotator, as shown in figure 3.8. If we take a randomly polarised source beam as an example, the polariser in Figure 3.8 allows only the vertically polarised (0°) components of the beam to pass. The beam is then rotated 45 degrees by the Faraday rotator and passed through an output polariser which allows only the vertical components that have been rotated by 45 degrees to pass. The beam is passed straight through the output polariser since it was polarised and rotated as required. If this beam returns on the same path and enters the output side of the optical isolator, only the vertical components that were rotated by 45 degrees will pass. The beam is then rotated a further 45 degrees by the Faraday rotator, resulting in a beam that is horizontally polarised (90°). The polariser therefore rejects the beam since it only allows

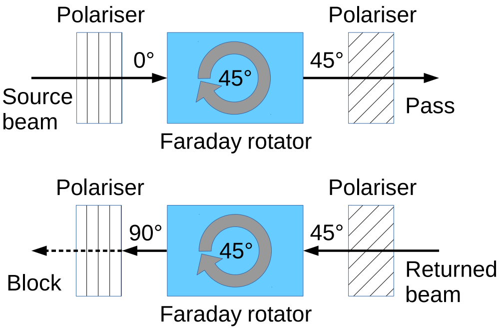

Figure 3.8: *A block diagram of an optical isolator. The source beam is allowed to pass through. The returned beam is blocked, preventing optical feedback.*

for vertically polarised (0°) beams to pass.

The output efficiency of the isolator depends on the polarisation of the input beam relative to the input polariser and the rejection efficacy is dependent on the polarisation of the returned beam relative to the output polariser.

3.2.5 Photodetector

For this experiment we measured the intensities of three beams: two beams from the saturated absorption spectroscopy setup and one from the Michelson interferometer. Photodetectors were used to measure these intensities. These devices operate using the photoelectric effect in which photons that are incident on the photodetector cause a current to flow proportionally. This current is converted to a voltage and recorded by a digital oscilloscope.

3.2.6 Rubidium Vapour Cell

The rubidium vapour cell in Figure 3.9 is a pressurised tube containing natural rubidium. The pressure is approximately 10^{-7} Torr and the isotopic

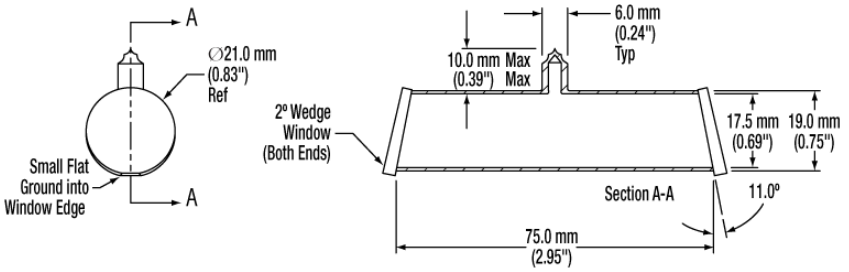

Figure 3.9: *Diagram of the rubidium vapour cell. (Adapted from* GC19075-RB - Rubidium Quartz Reference Cell *2017)*

composition of the gas is 72.2% ^{85}Rb and 27.8% ^{87}Rb.

Assuming the rubidium gas is at room temperature, the average speed of the atoms is then approximately 300 meters per second ($m{\cdot}s^{-1}$). The average speed given by

$$\bar{v} = \sqrt{\frac{3K_BT}{m}} \ , \tag{3.1}$$

where m is the mass of the atom, K_B is Boltzmann's constant, and T is the temperature in Kelvins. It is this thermal motion that causes the broadening of absorption lines as described in Chapter 2.5.

3.2.7 Helmholtz Coils

In our study of the Zeeman effect, we measured certain magnetic sub-levels of rubidium. To do this it was necessary to generate a uniform magnetic field in the region of the rubidium vapour cell. A pair of Helmholtz coils was fabricated in order to generate this field.

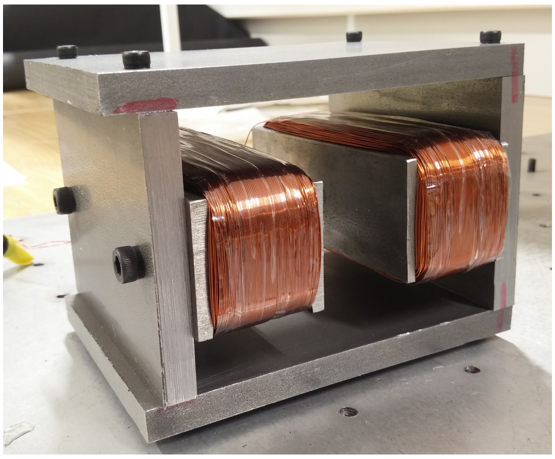

Figure 3.10: *Helmholtz coils used to generate a uniform magnetic field in the region of the rubidium vapour cell.*

The direction of the field is set to be perpendicular to the propagation of the laser beams through the rubidium vapour cell. Therefore, only the transitions which satisfy the $\Delta m = 0$ selection rule are allowed. These transitions, as well as the calibration of the Helmholtz coils, are discussed in Chapter 5.

3.3 Operation of the SAS Setup

The operation of the saturated absorption spectroscopy setup is as follows. When the laser is tuned to certain wavelengths the atoms in the Rb vapour cell will absorb photons and the light at the output side of the Rb cell will drop in intensity. The photodetectors in both arrangements measure the intensity of the signal and reference beams, these signals are then fed into an instrumentation amplifier which outputs the difference between the two beams as shown in figure 3.11. The output corresponds to the absorption profile for the energy states being probed. We record this output with a digital oscilloscope and calibrate the recording using the Michelson interferometer.

To ensure we measure the full absorption spectrum we sweep the laser frequency linearly over a wide range. This modulation is achieved by having a signal generator produce a ramp signal of variable amplitude for precise control of the modulation range. This signal is then fed to the laser controller that adjusts the angle of laser cavity mirror via a piezoelectric actuator, which in turn modulates the frequency of the light.

To measure the Zeeman levels we wired the Helmholtz coils to a power supply where the voltage could be varied. During measurements the current

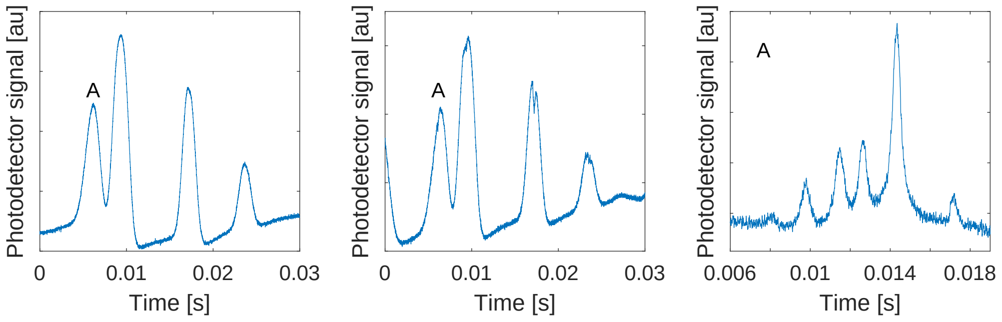

(a) (b) (c)

Figure 3.11: *Photodetector outputs from the saturated absorption spectroscopy experiment. (a): photodetector output of the reference beam. (b): photodetector output of the signal beam. (c): the difference between the two photodetector outputs. This plot shows the resulting signal only for peak **A** of plots (a) and (b).*

was recorded and related to the magnetic field strength by the calibration of the Helmholtz coils.

3.4 Laser Locking Setup

In order to perform laser cooling of atoms, it is necessary to lock the laser to specific atomic transitions in the absorption spectrum of rubidium. This is achieved using a feedback system, as described in Chapter 2.5, which we refer to as the laser locking system. Although this section provides a description of the operation of the laser locking setup, certain aspects of the discussion on feedback systems given in Chapter 2.5 are repeated where necessary.

The laser locking setup consisted of a proportional-integral-derivative (PID) controller, an external cavity diode laser (ECDL), a saturated absorption spectroscopy (SAS) setup (Chapter 3.2), and a lock-in amplifier. The PID controller was a pre-built unit and the lock-in amplifier was developed by our research group. We investigated two techniques for locking an ECDL, these techniques are commonly referred to as side locking and peak locking.

Side Locking

Figure 3.12a shows a block diagram of the side locking arrangement of the laser locking system. Figure 3.12b indicates the set point (green dashed line) and measured value (red dashed line) along the frequency response of the SAS setup (blue line). The set point is chosen to be a point along a side of

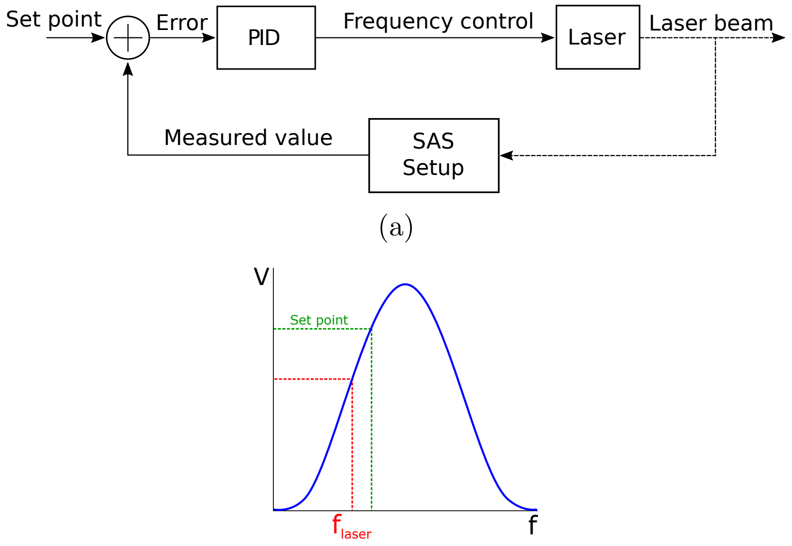

(a)

(b)

Figure 3.12: *(a): Laser frequency control system, setup to perform side locking. The system consists of a proportional-integral-derivative (PID) controller, a laser, and a saturated absorption spectroscopy (SAS) setup. The solid arrows indicate voltage signals and the dashed arrows represent laser light. (b): Frequency response of the SAS setup (blue curve). The green dashed line indicates the point on the response curve at which the laser frequency should be maintained, corresponding to the set point. The red dashed line indicates the point on the response curve that corresponds to the output voltage of the SAS setup due to the laser frequency.*

one of the absorption peaks and the measured value corresponds to a point along a side of one of the absorption peaks due to the laser frequency (i.e. the the absorption signal from the SAS setup). If the laser frequency deviates, the measured value and set point will no longer match. By monitoring the absorption signal from the SAS setup, the control system can determine if the laser frequency is deviating and correct for the deviation accordingly. This correction is performed by varying the voltage supplied to the frequency modulation inputs on the laser controller in such a way that error tends to zero.

Peak Locking

Figure 3.13a shows a block diagram of the peak locking setup arrangement of the laser locking system which sees the addition of a lock-in amplifier. It is called peak locking as the net effect of modulating the laser frequency and the lock-in amplifier is equivalent to finding the derivative (Figure 3.13b) of the hyperfine peak (Figure 3.13c) which effectively allows us to lock onto the maximum of the hyperfine peak if the output of the lock-in amplifier is maintained at zero.

As with the side locking setup described earlier, a PID controller is used to adjust the frequency of the laser in such a way that the error term approaches zero. The only difference with peak locking is that the set point is no longer a point on the hyperfine peak but rather the zero-crossing of the derivative of the hyperfine peak. Due to time constraints we were unable to test the laser frequency control system in the peak locking setup, however, we did test the lock-in amplifier. More information and test results on the lock-in amplifier are given in Appendix B.

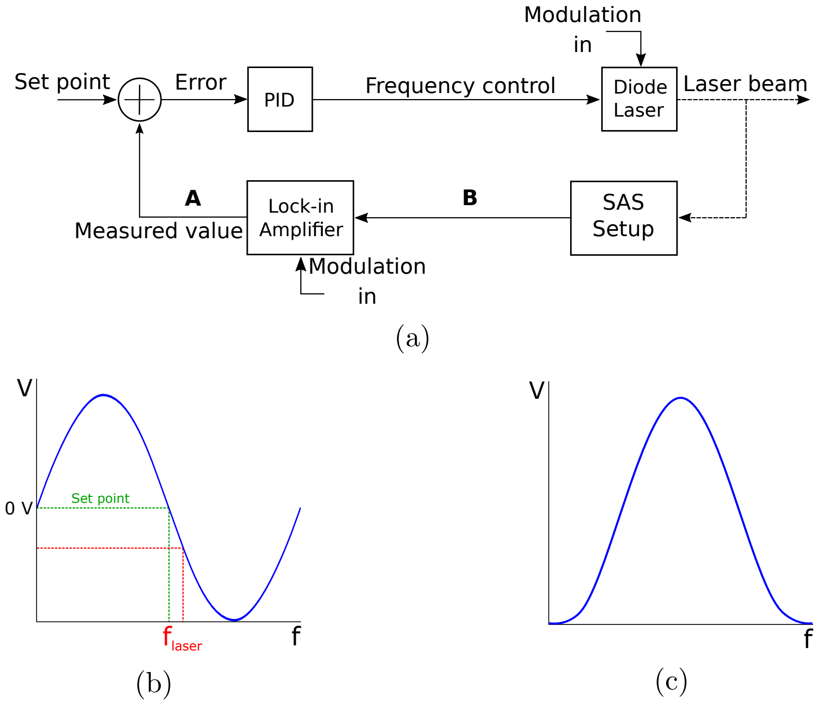

(a)

(b)

(c)

Figure 3.13: *(a): Laser frequency control system, setup to perform peak locking. The system consists of a proportional-integral-derivative (PID) controller, laser, SAS setup, and a lock-in amplifier. The solid arrows indicate voltage signals and the dashed arrows represent laser light.* ***A*** *and* ***B*** *correspond to the plots (b) and (c), respectively, beneath diagram (a). (b): Frequency response of the SAS setup (blue curve). The green dashed line indicates the point on the response curve at which the laser frequency should be maintained, corresponding to the set point. The red dashed line indicates the point on the response curve that corresponds to the output voltage of the SAS setup due to the laser frequency. (c): "Differentiated" frequency response of the SAS setup (blue curve).*

3.5 Summary

We have described the saturated absorption spectroscopy setup, diagrams of the two saturated absorption spectroscopy arrangements were given as well as an overview of their operation. A similar description of the Michelson interferometer was provided. Measurements of the hyperfine spectra and magnetic hyperfine spectra, using the saturated absorption spectroscopy setup, can be found in Chapters 4 and 5 respectively.

Additionally, a discussion of the laser locking setup was provided, diagrams of the side and peak locking setups are given as well as an overview of their operation. A characterisation of the side locking setup is given in Chapter 6.

Chapter 4

Saturated Absorption Spectroscopy Results

4.1 Introduction

In this chapter we present the measurement results of the saturated absorption spectroscopy experiment in which we investigated the electronic transitions between the $5S_{1/2}$ and $5P_{3/2}$ energy levels of rubidium 85 (^{85}Rb) and rubidium 87 (^{87}Rb). We measured both the Doppler broadened and hyperfine absorption spectra using a saturated absorption spectroscopy setup, and calibrated the measurements using a Michelson interferometer. We compare the energy separation between states and the lifetime of each state to accepted values in the literature.

4.2 Theory

Figure 4.1 shows the energy level structure of the ground and first excited states of ^{85}Rb and ^{87}Rb. Here the ground state is represented in spectroscopic

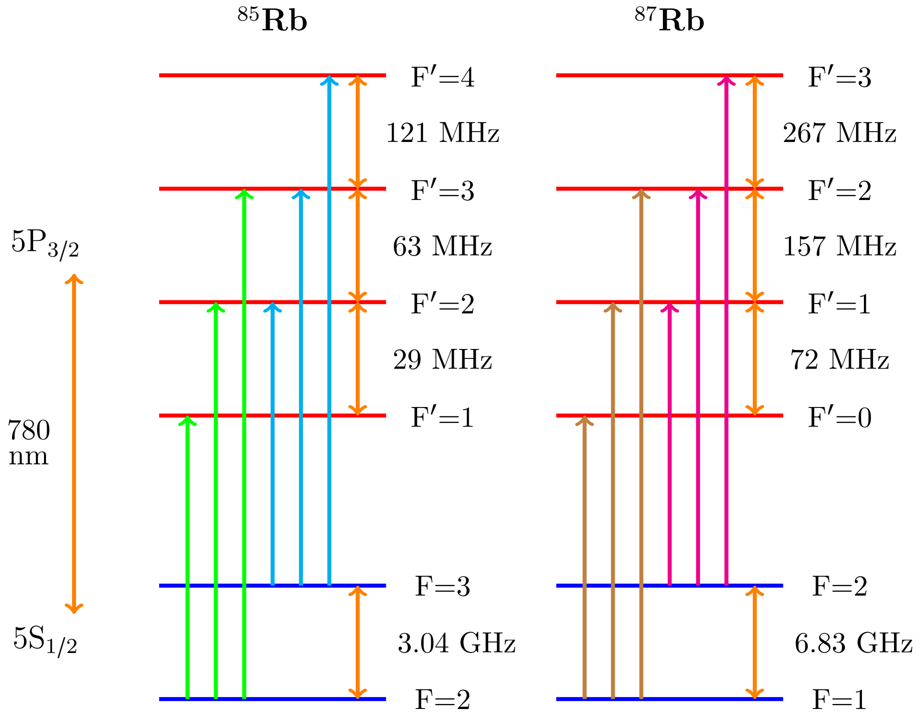

Figure 4.1: *Energy level diagram of the $5S_{1/2}$ to $5P_{3/2}$ hyperfine structure of rubidium 85 and rubidium 87. The energy level separations are given in units of frequency.*

notation as 5S$_{1/2}$ and the excited state as 5P$_{3/2}$. The transition from 5S$_{1/2}$ to 5P$_{3/2}$ has a resonant frequency of approximately 384.23 THz, corresponding to a wavelength of 780.24 nm when using the relation $c = f\lambda$. The ground state of each isotope is split into two hyperfine states, denoted by F, and the excited state of each isotope is split into four hyperfine states, denoted by F′. The allowed transitions between hyperfine states are those for which the $\Delta F = 0, \pm 1$ selection rule is satisfied.

Figure 4.1 excludes crossover resonances that are visible in the measured absorption spectra. These resonances are a consequence of the beam configuration in the saturated absorption setup and occur when the laser is detuned exactly halfway between two excited states that share a ground state. The frequency of each crossover resonance is therefore

$$\nu_c = \frac{|\nu_f - \nu_i|}{2} \ , \tag{4.1}$$

with ν_f and ν_i being the frequencies of the excited states that share a ground state. When the laser is at the crossover frequency ν_c, it is in resonance with two opposing velocity groups. Thus, atoms moving in the direction opposing beam propagation see the frequency to be blue shifted towards the higher resonant frequency, while atoms moving in the same direction as beam propagation see the frequency to be red shifted towards the lower resonant frequency. Since absorption occurs within two velocity groups, crossover resonances could be identified by large peaks in the absorption spectra.

4.3 Data Processing

The signals from the saturated absorption spectroscopy experiment were recorded using a digital oscilloscope. Three signals are recorded: the signal from the saturated absorption spectroscopy experiment, the signal from the Michelson interferometer, and the laser frequency modulation ramp signal from a signal generator. Multiple measurements were carried out using the same experimental parameters in order to reduce random errors.

A sample of the recorded signals are plotted in Figure 4.2. Figure 4.2(a) shows the ramp signal used to modulate the laser frequency. Figure 4.2(b) shows an output signal from the saturated absorption spectroscopy setup. This signal is characterised by peaks that are due to changes in beam intensity when absorption occurs as the laser frequency is swept linearly by the

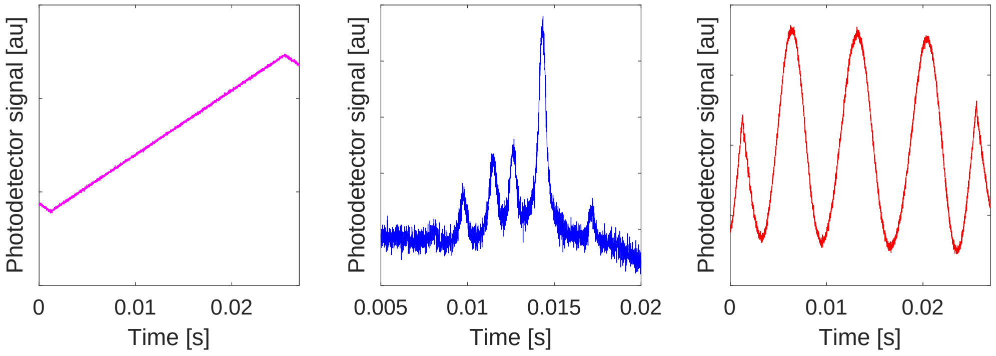

(a) (b) (c)

Figure 4.2: *Signals recorded from the saturated absorption spectroscopy experiment. (a): laser frequency modulation ramp signal (pink trace). (b): output signal from the saturated absorption spectroscopy setup (blue trace). (c): output signal from the Michelson interferometer (red trace).*

ramp signal in (a). Figure 4.2(c) shows the output signal from the Michelson interferometer. The output of the interferometer is sinusoidal, corresponding to bright and dark fringes as the laser frequency is swept linearly by the ramp signal in (a).

After recording the signals, the time scale of each absorption measurement was converted to a frequency scale and the absorption measurements were plotted as spectra. The spectra were characterised by analysing each absorption peak in terms of its relative frequency and lifetime, and compared to the literature and theory.

4.3.1 Calibration of Absorption Measurements

In order to plot the absorption as a function of frequency (i.e. a spectrum), we needed to calibrate the time axis of each recording into a frequency axis. The calibration was performed using the Michelson interferometer described in Chapter 3, the calibration process is described below.

As the laser frequency is swept, the two beams interfere constructively and destructively at the output of the Michelson interferometer. This shows up as a series of light and dark central spots on the photodetector, resulting in a sinusoidal pattern of high and low intensity as the output signal. The time between two consecutive maxima in the Michelson interferometer output signal, and the change in laser frequency are related by

$$\Delta f_{laser} = \frac{c}{2\Delta d} \cdot \frac{T_{sample}(n_2 - n_1)}{T_{Michelson}} , \tag{4.2}$$

where Δf_{laser} is the change in the laser frequency, c is the speed of light in vacuum, Δd is the difference in length between the two paths of the Michelson interferometer (doubled because the beams are reflected), T_{sample} is the sampling period of the recorded data, $n_2 - n_1$ is the amount of samples over which the change in frequency is to be calculated, and $T_{Michelson}$ is the period of the signal from the Michelson interferometer.

By performing a fast Fourier transform (FFT) of the output signal from the Michelson interferometer (Figure 4.3a) we can estimate the period of the signal and thus calculate the change in laser frequency using Equation (4.2). The FFT spectrum, and the relationship between the laser frequency and time for a given data set is plotted in Figures 4.3b and 4.3c respectively.

During our investigation we noticed that the ^{85}Rb absorption signal required a very small laser frequency ramp in order to get a reasonable resolution of the absorption lines. The small ramp signal resulted in less than one full cycle of the Michelson interferometer output signal. Since the pe-

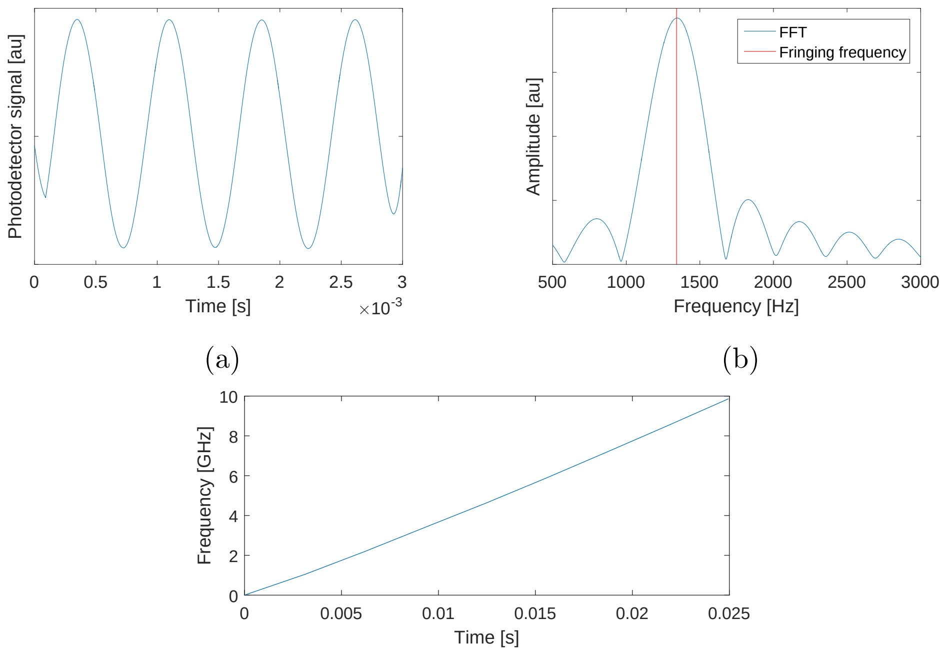

(a) (b)

(c)

Figure 4.3: *(a): output signal from the Michelson interferometer. (b): fast Fourier transform derived spectrum of (a). (c): calculated change in laser frequency over the measurement period.*

riod of the Michelson interferometer signal is required to calibrate the time axis of each absorption measurement, it had to be estimated using a method other than the FFT. The period was estimated by finding a relationship between the amplitude of the ramp signal and the period of the signal from the Michelson interferometer. A range of amplitudes of the ramp signal were recorded and the corresponding period of the signal from the Michelson interferometer was calculated. A curve fitting routine was performed on the data to find the function with the best fit. The period of the output signal from the Michelson interferometer was then estimated from the function, for very low frequencies of the Michelson interferometer output signal, and Equation (4.2) was used to find the change in frequency of the laser. The frequency

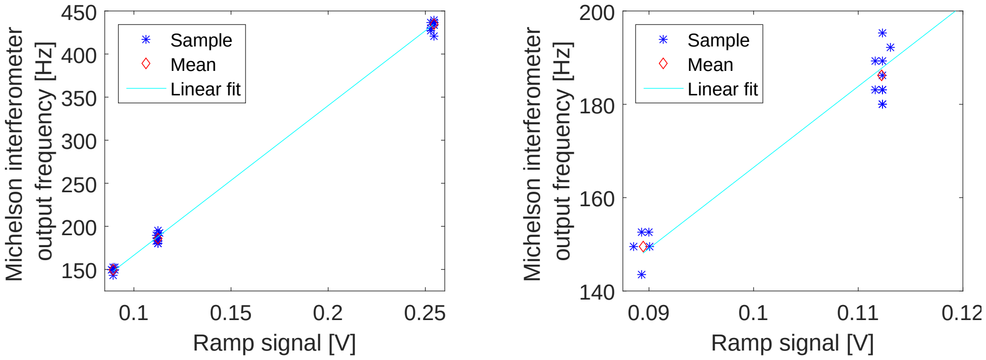

(a) (b)

Figure 4.4: *(a): Michelson interferometer output signal frequency as a function of the amplitude of the laser frequency modulation ramp signal. (b): An expanded view of (a).*

of the output signal from the Michelson interferometer as a function of the ramp signal amplitude is shown in Figure 4.4.

After the calculating the change in laser frequency we plotted the absorption as a function of frequency. Figure 4.5 shows an absorption signal that is plotted as a function of time and as a function of frequency in order to demonstrate the x-axis calibration.

4.3.2 Characterisation of Absorption Spectra

We now look at how we characterised the absorption spectra in terms of the change in energy between excited states and the associated excited state lifetimes. Since the centre of each peak in a given spectrum corresponds to the resonant frequency of that transition, the distance between any two peaks is therefore a measure of the change in energy between any two excited states. The lifetime of an excited state is related to the width of the peak corresponding to that transition. The process of characterising peaks by their

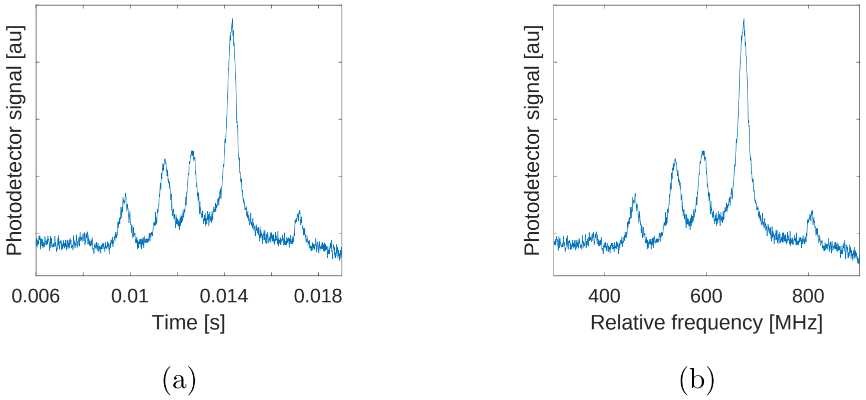

Figure 4.5: *An absorption signal that is plotted as: (a) a function of time and (b) a function of frequency*

resonant frequency and width is given below.

When locating the peaks, we first smoothed the data using a moving average filter to reduce or eliminate erroneous detection of peaks. Figure 4.6a shows how noise in the unfiltered signal does not lead to the detection of a true peak, and Figure 4.6b illustrates how this issue is avoided after the signal is filtered. This method also avoids the detection of false peaks. We will refer to this as a rough location of peaks.

After filtering the signal and performing a rough location of peaks, we fitted a curve to each of the peaks. Curve fitting allows for a finer location of the peaks, which improves estimations of the distances between peaks; additionally, it allows for calculation of the peak width, which is related to the lifetime of the state. The Doppler broadened absorption peaks are characterised by the Gaussian function

$$f = e^{-\frac{(\omega-\omega_0)^2}{2\sigma^2}} \;, \tag{4.3}$$

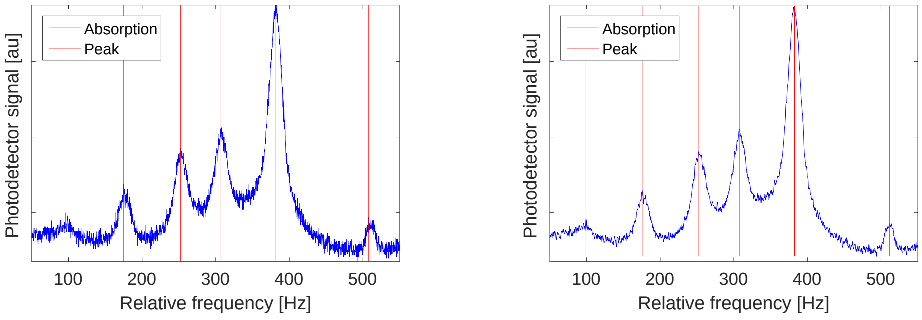

(a) (b)

Figure 4.6: *Detected peak locations for unfiltered data (a) and for filtered data (b).*

where ω_0 is the resonant frequency for the transition and σ is the reciprocal of the lifetime of the excited state. The hyperfine absorption peaks are characterised by the Lorentzian function

$$f = \frac{\gamma^2}{(\omega - \omega_0)^2 + \gamma^2} , \tag{4.4}$$

with γ as the reciprocal of the lifetime of the excited state, and ω_0 as the resonant frequency for the transition.

Shown in Figures 4.7 and 4.8 are the Doppler broadened and hyperfine absorption spectra, respectively. Included in each plot are the fitted curves and the maximum locations obtained using the rough and fine methods.

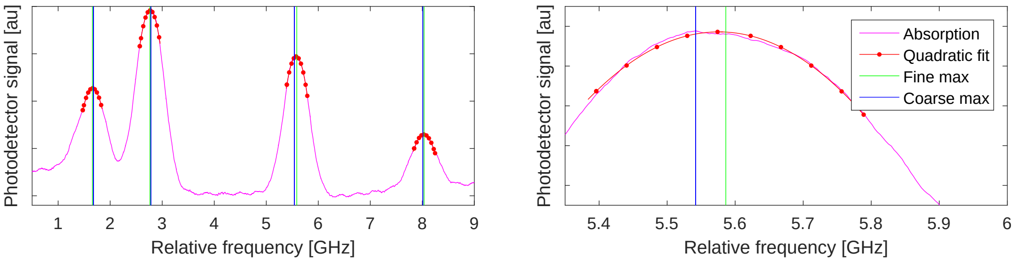

(a)

(b)

Figure 4.7: *(a): Doppler broadened absorption spectrum of ^{85}Rb and ^{87}Rb with peak locations indicated by vertical lines. (b): An expanded section of the Doppler broadened absorption spectrum showing the difference in the coarse and fine peak locations for one peak. The legend applies to both plots.*

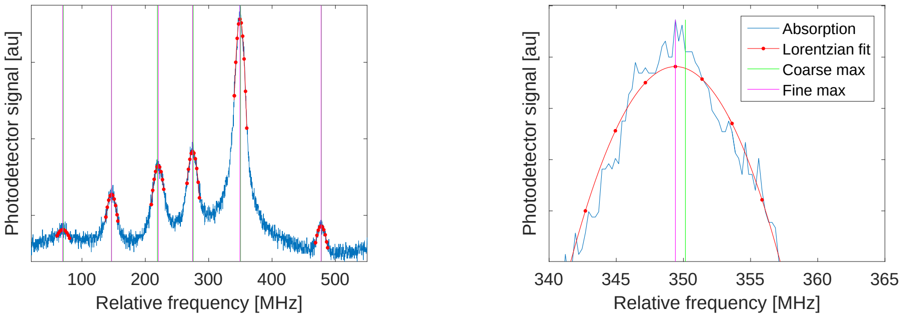

(a)

(b)

Figure 4.8: *(a): Hyperfine absorption spectrum of ^{87}Rb $F = 2$ to $F' = 1, 2, 3$ with peak locations indicated by vertical lines. (b): An expanded section of the hyperfine spectrum which shows the difference in the coarse and fine peak locations for one peak. The legend applies to both plots.*

Three methods were used to calculate the peak separations and excited state lifetimes:

- **Method A** takes each recording and characterises the spectra individually before calculating the average ΔE and Γ values, and their respective uncertainties.

- **Method B** calculates the average calibration factor for the frequency axis conversion, applies this factor to all recordings, and then proceeds to calculate the average ΔE and Γ values per recording.

- **Method C** was used when there was less than one full cycle in the output signal of the Michelson interferometer. It estimates the calibration factor for the conversion of the frequency axis using a linear function that fits previously recorded values, the process is described in Section 4.3.1. The method then follows the same procedure as **Method A**.

4.4 Results and Discussion

In this section we discuss the measurements of the absorption spectra of rubidium. The absorption spectra were measured using a saturated absorption spectroscopy setup arranged in two ways, arrangement 1 is shown in Figure 3.1 and arrangement 2 is shown in Figure 3.3. Calibration of these measurements was performed using a Michelson interferometer (Figure 3.5). The resulting energy level separations were compared with accepted values in the literature. The energy level separations are given in units of frequency (MHz) and the lifetime of the excited states are given in units of time (ns).

We begin this discussion with the Doppler broadened spectrum and then progress through the hyperfine spectra.

4.4.1 Doppler Broadened Absorption Spectrum

The Doppler broadened absorption spectrum is observed when an absorption spectroscopy setup is used, like the one in Figure 2.10. In our saturated

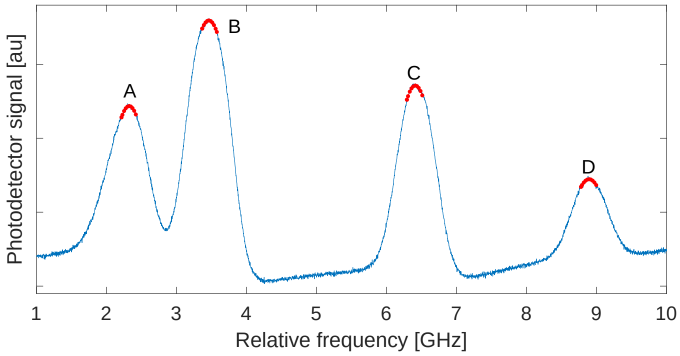

Figure 4.9: *A Doppler broadened absorption spectrum that was obtained by blocking the pump beam in the saturated absorption spectroscopy setup, both the saturated absorption spectroscopy setup arrangements produced the same spectrum. The peaks labelled* ***A*** *to* ***D*** *correspond to the following transitions.* ***A****:* $^{87}Rb\ F = 2$ *to* $F' = 1, 2, 3$*.* ***B****:* $^{85}Rb\ F = 3$ *to* $F' = 2, 3, 4$*.* ***C****:* $^{85}Rb\ F = 2$ *to* $F' = 1, 2, 3$*.* ***D****:* $^{87}Rb\ F = 1$ *to* $F' = 0, 1, 2$*.*

absorption spectroscopy setup (Figures 3.1 and 3.3) we block one of the photodetectors to mimic an absorption spectroscopy setup, thus allowing us to observe the absorption spectrum in Figure 4.9.

The following transitions are allowed:

A ^{87}Rb $F = 2$ to $F' = 1, 2, 3$

B ^{85}Rb $F = 3$ to $F' = 2, 3, 4$

C ^{85}Rb $F = 2$ to $F' = 1, 2, 3$

D ^{87}Rb $F = 1$ to $F' = 0, 1, 2$

These transitions are illustrated in figure 4.1, and the measured energy level separations are given in table 4.1. In this table the mean value of the measurement data is given as the final result, and the standard deviation is given as the uncertainty of the measurement.

Table 4.1: *Ground state energy level separation of* ^{85}*Rb and* ^{87}*Rb, in units of frequency (MHz).* ***A*** *to* ***D*** *correspond to the peaks labelled in Figure 4.9.*

SAS arrangement	Ground states	Measured separation	Accepted value
Arrangement 2	^{85}Rb F=3 (**B**) to F=2 (**C**)	2876±15	3036
	^{87}Rb F=2 (**A**) to F=1 (**D**)	6506±39	6835

It was noted that the measured energy level separations were underestimated when compared to the literature. This was investigated and is discussed in the next section.

Revision of Ground State Energy Separations

Our underestimation of the energy separation was likely due the fact that the maxima of the Doppler broadened peaks are not the correct reference points for measuring the ground state separations. The correct points to use should be the hyperfine peaks for which the quantum number F' is equal.

We make corrections to the previous estimate as follows. We fitted Gaussian curves to the ^{87}Rb Doppler broadened absorption spectra containing the hyperfine peaks as shown in Figures 4.10a and 4.10b. Using the fitted Gaussian curves and the hyperfine peaks, we calculated the separation between the Gaussian peak and a particular hyperfine peak for both F=2 to F′=1,2,3 and F=1 to F′=0,1,2 transitions (vertical lines in Figures 4.10a and 4.10b). We then add these to the previous estimates of the separation for the F=2 to F′=1,2,3 and F=1 to F′=0,1,2 transitions of ^{87}Rb. A similar analysis is done for the F=3 to F′=2,3,4 and F=2 to F′=1,2,3 transitions of ^{85}Rb.

The revised ground state energy separations are given in Table 4.2. For

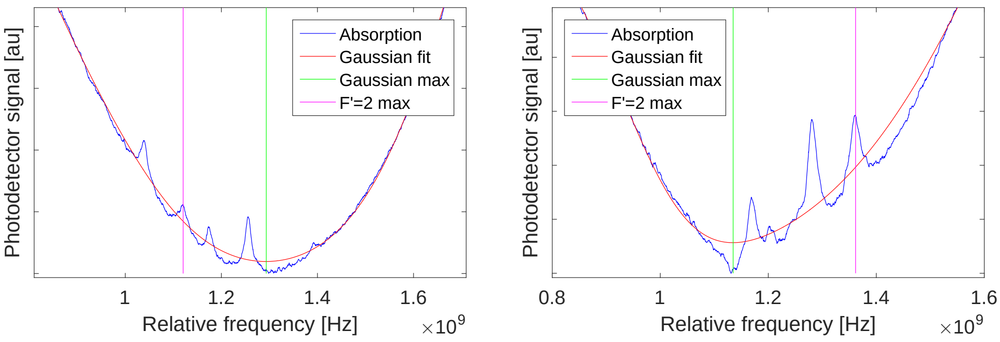

(a) (b)

Figure 4.10: *(a): Hyperfine absorption spectrum of the* ^{87}*Rb F=2 to F′=1,2,3 transitions; the location of the Doppler maximum (green line) and the* $F = 2$ *to* $F' = 2$ *transition (pink line) is given. (b): Hyperfine absorption spectrum of the* ^{87}*Rb F=1 to F′=0,1,2 transitions, the location of the Doppler maximum (green line) and the* $F = 1$ *to* $F' = 2$ *transition (pink line) is given.*

the ^{87}Rb F=2 to F′=1,2,3 and ^{87}Rb F=1 to F′=0,1,2 transitions, the separation was calculated between the Gaussian maxima and peaks for which F′=2. For the ^{57}Rb F=3 to F′=2,3,4 and F=2 to F′=1,2,3 transitions, the separation was calculated between the Gaussian maxima and peaks for which F′=3.

These values show an improved agreement with the literature and theory. It must be noted that the hyperfine absorption peaks are shifted to the outside of the Doppler broadened peaks. From the revised results it is clear that this has the effect of increasing the energy separation between ground states. A more thorough investigation is recommended.

Table 4.2: *Revised ground state energy level separation of ^{85}Rb and ^{87}Rb, in units of frequency (MHz).* ***A*** *to* ***D*** *correspond to the peaks labelled in Figure 4.9.*

SAS arrangement	Ground states	Measured separation	Accepted value
Arrangement 2	^{85}Rb F=3 (**B**) to F=2 (**C**)	3087	3036
	^{87}Rb F=2 (**A**) to F=1 (**D**)	6905	6835

4.4.2 Hyperfine Absorption Spectra

The hyperfine absorption spectra are observed when a saturated absorption spectroscopy setup is used. Our setup was arranged in two ways, arrangement 1 is shown in Figure 3.1 and arrangement 2 is shown in Figure 3.3. The spectral measurements are presented in ascending order of frequency, i.e. from **A** to **D** in Figure 4.9.

^{87}Rb F=2 to F′=1,2,3 Absorption Spectrum

The ^{87}Rb $F = 2$ to $F' = 1, 2, 3$ absorption spectrum shown in Figure 4.11 is observed at the low frequency end of the $5S_{1/2}$ to $5P_{3/2}$ hyperfine transitions.

The following transitions are allowed:

a $F = 2$ to $F' = 1$

b $F = 2$ to $F' = c1$, a crossover between states $F' = 1$ and $F' = 2$

c $F = 2$ to $F' = 2$

d $F = 2$ to $F' = c2$, a crossover between states $F' = 1$ and $F' = 3$

e $F = 2$ to $F' = c3$, a crossover between states $F' = 2$ and $F' = 3$

f $F = 2$ to $F' = 3$

These transitions are illustrated in Figure 4.12. The measured energy level separations are given in Table 4.3, and the lifetime of the excited states is given in Table 4.4.

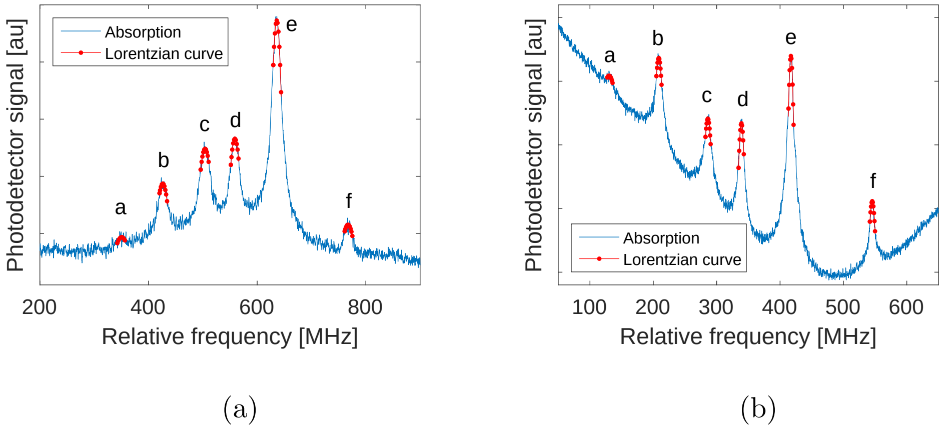

(a) (b)

Figure 4.11: *Absorption spectrum of the* ^{87}*Rb* $F = 2$ *to* $F' = 1, 2, 3$ *transitions measured using arrangement 1 (a) and arrangement 2 (b) of the SAS setup. The hyperfine transitions are as follows.* ***a****:* $F = 2$ *to* $F' = 1$*.* ***b****:* $F = 2$ *to* $F' = c1$*, a crossover between* $F' = 1$ *and* $F' = 2$*.* ***c****:* $F = 2$ *to* $F' = 2$*.* ***d****:* $F' = c2$*, a crossover between* $F' = 1$ *and* $F' = 3$*.* ***e****:* $F = 2$ *to* $F' = c3$*, a crossover between* $F' = 2$ *and* $F = 3$*.* ***f****:* $F = 2$ *to* $F' = 3$*.*

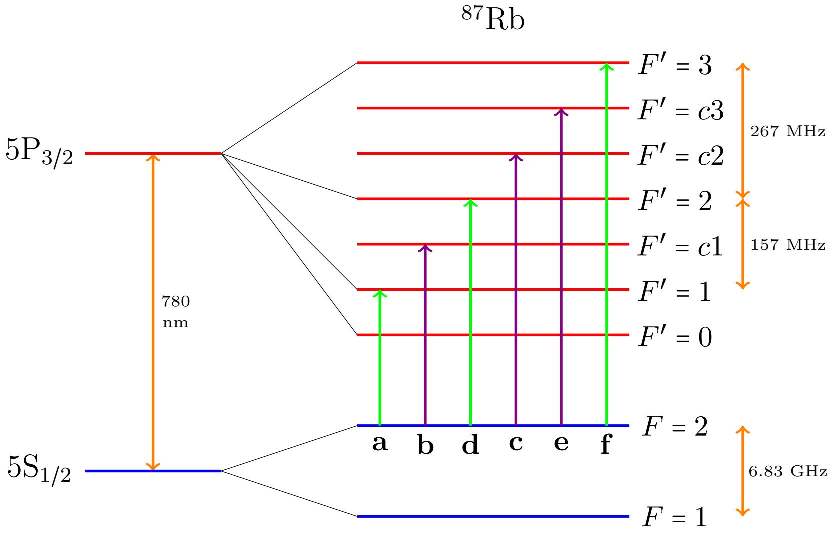

Figure 4.12: *Energy level diagram showing the* ^{87}*Rb* $F = 2$ *to* $F' = 1, 2, 3$ *transitions. Green arrows indicate normal transitions and purple arrows indicate crossover transitions. Transitions have been labelled* ***a*** *to* ***f*** *in accordance with the labels in Figure 4.11. Excited states* $F' = c1$, $F' = c2$ *and* $F' = c3$ *are crossover resonances.*

Table 4.3: *Excited state energy separation in units of frequency (MHz). Excited states **a** to **f** correspond to the peaks labelled in Figure 4.11.*

SAS arrangement	Peaks	Measured separation:			Accepted value
		Method A	Method B	Method C	
Arrangement 1	**a–b**	77±4	75±3	77±2	79
	b–c	77±3	77±1	77±1	79
	c–d	54±2	54±1	54±1	55
	d–e	77±2	77±1	77±1	79
	e–f	131±4	131±1	132±2	133
Arrangement 2	**a–b**	80±3	76±1	81±1	79
	b–c	77±1	72±1	78±1	79
	c–d	54±2	50±1	54±1	55
	d–e	79±1	74±1	79±1	79
	e–f	130±4	122±1	131±1	133

Table 4.4: *Excited state lifetime in units of time (ns). Excited states **a** to **f** correspond to the peaks labelled in Figure 4.11.*

SAS arrangement	Peak	Excited state lifetime:		
		Method A	Method B	Method C
Arrangement 1	**a**	5±1	4±2	4±1
	b	10±1	10±1	10±1
	c	11±1	11±1	11±1
	d	12±1	12±1	12±1
	e	20±1	19±1	20±1
	f	9±1	9±1	9±1
Arrangement 2	**a**	10±1	9±1	9±2
	b	21±1	22±2	21±1
	c	18±1	20±1	19±1
	d	26±3	26±3	25±3
	e	32±4	33±4	30±4
	f	19±4	21±4	19±4

^{85}Rb F=3 to F′=2,3,4 Absorption Spectrum

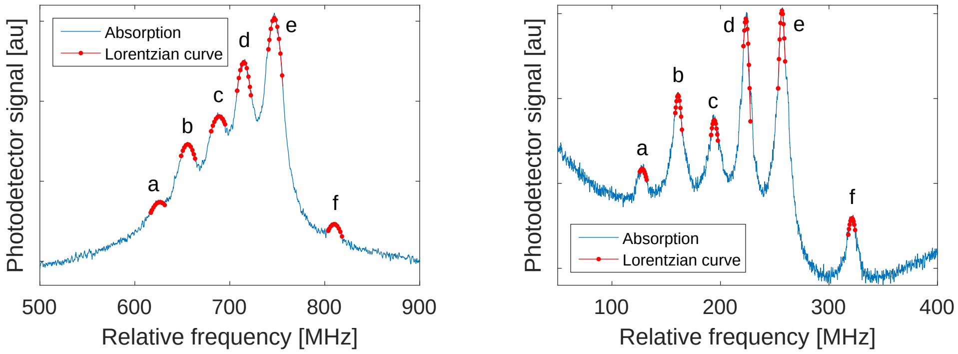

(a) (b)

Figure 4.13: *Absorption spectrum of the* ^{85}*Rb* $F = 3$ *to* $F' = 2, 3, 4$ *transitions measured using arrangement 1 (a) and arrangement 2 (b) of the SAS setup. The hyperfine transitions are as follows.* ***a****:* $F = 3$ *to* $F' = 2$*.* ***b****:* $F = 3$ *to* $F' = c1$*, a crossover between states* $F' = 2$ *and* $F' = 3$*.* ***c****:* $F = 3$ *to* $F' = 3$*.* ***d****:* $F = 3$ *to* $F' = c2$*, a crossover between states* $F' = 2$ *and* $F' = 4$*.* ***e****:* $F = 3$ *to* $F' = c3$*, a crossover between states* $F' = 3$ *and* $F' = 4$*.* ***f****:* $F = 3$ *to* $F' = 4$*.*

The ^{85}Rb $F = 3$ to $F' = 2, 3, 4$ absorption spectrum is shown in Figure 4.13.

The following hyperfine transitions are allowed:

a $F = 3$ to $F' = 2$

b $F = 3$ to $F' = c1$, a crossover between states $F' = 2$ and $F' = 3$

c $F = 3$ to $F' = 3$

d $F = 3$ to $F' = c2$, a crossover between states $F' = 2$ and $F' = 4$

e $F = 3$ to $F' = c3$, a crossover between states $F' = 3$ and $F' = 4$

f $F = 3$ to $F' = 4$

These transitions are illustrated in Figure 4.14. The measured energy level separations are given in Table 4.5, and the lifetime of the excited states is given in Table 4.6.

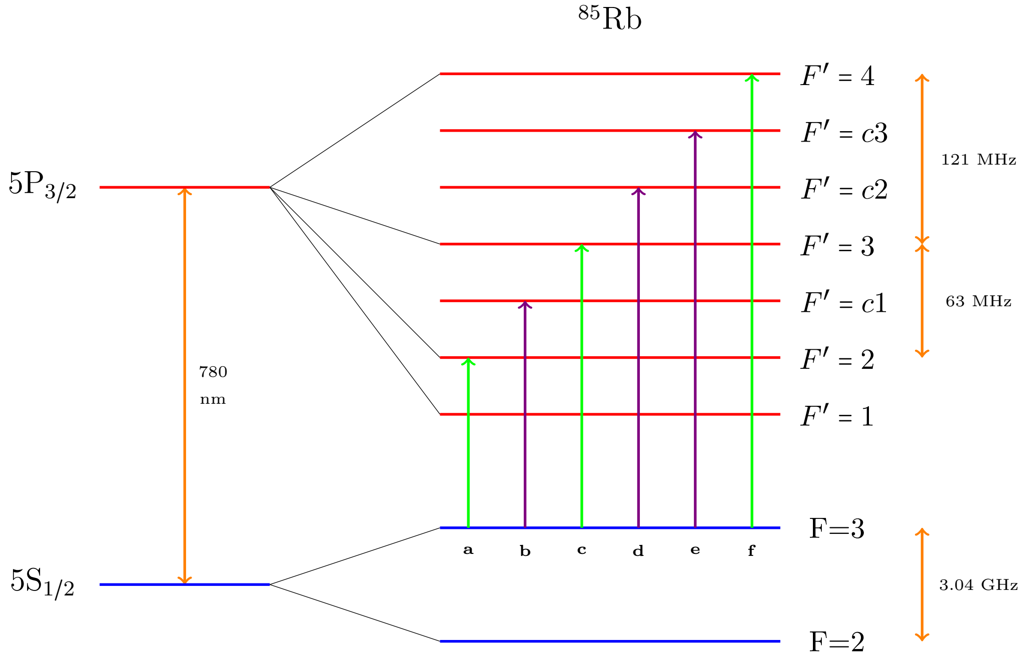

Figure 4.14: *Energy level diagram showing the ^{85}Rb $F = 3$ to $F' = 2, 3, 4$ transitions. Green arrows indicate normal transitions and purple arrows indicate crossover transitions. Transitions have been labelled **a** to **f** in accordance with the labels in Figure 4.13. Excited states $F' = c1$, $F' = c2$ and $F' = c3$ are crossover resonances.*

Table 4.5: *Excited state energy separation in units of frequency (MHz). Excited states **a** to **f** correspond to the peaks labelled in Figure 4.13.*

SAS arrangement	Peaks	Measured separation: Method A	Measured separation: Method B	Measured separation: Method C	Accepted value
Arrangement 1	**a–b**	26±2	25±5	22±5	32
	b–c	32±1	32±1	32±1	32
	c–d	27±1	27±1	26±1	29
	d–e	31±1	31±1	30±1	30
	e–f	61±2	61±1	59±1	60
Arrangement 2	**a–b**	31 ±1	36±1	30±1	32
	b–c	33 ±1	38±1	32±1	32
	c–d	28 ±1	32±1	28±1	29
	d–e	32 ±1	36±1	31±1	30
	e–f	61 ±2	71±1	60±1	60

Table 4.6: *Excited state lifetime in units of time (ns). Excited states **a** to **f** correspond to the peaks labelled in Figure 4.13.*

SAS arrangement	Peak	Excited state lifetime: Method A	Excited state lifetime: Method B	Excited state lifetime: Method C
Arrangement 1	**a**	6±2	6±2	5±2
	b	13±1	14±1	14±1
	c	13±1	13±1	13±1
	d	19±1	19±1	20±1
	e	24±1	24±1	24±1
	f	9±1	9±1	10±1
Arrangement 2	**a**	12±1	12±1	14±2
	b	24±2	20±3	25±2
	c	19±3	16±4	18±4
	d	35±2	34±3	37±3
	e	35±3	31±3	37±4
	f	21±2	16±2	21±2

^{85}Rb F=2 to F′=1,2,3 Absorption Spectrum

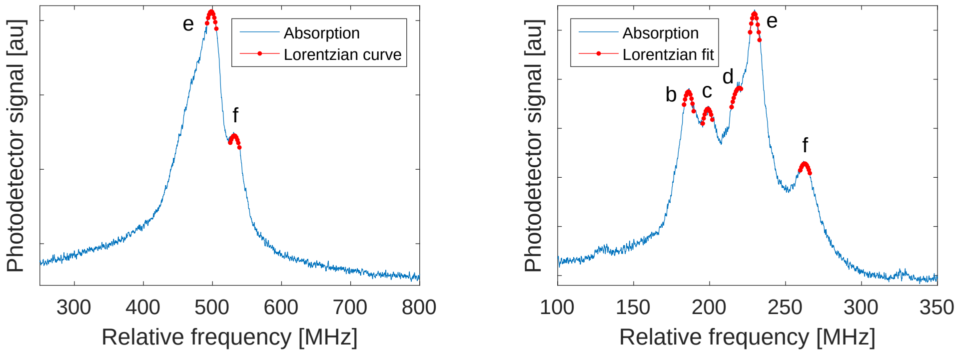

(a) (b)

Figure 4.15: *Absorption spectrum of the ^{85}Rb $F = 2$ to $F' = 1, 2, 3$ transitions measured using arrangement 1 (a) and arrangement 2 (b) of the SAS setup. The hyperfine transitions are as follows.* ***b****: $F = 2$ to $F' = c1$, a crossover between states $F' = 1$ and $F' = 2$.* ***c****: $F = 2$ to $F' = 2$.* ***d****: $F = 2$ to $F' = c2$, a crossover between states $F' = 1$ and $F' = 3$.* ***e****: $F = 2$ to $F' = c3$, a crossover between states $F' = 2$ and $F' = 3$.* ***f****: $F = 2$ to $F' = 3$.*

The ^{85}Rb $F = 2$ to $F' = 1, 2, 3$ absorption spectrum is shown in Figure 4.15.

The following hyperfine transitions are allowed:

a $F = 2 \rightarrow F' = 1$

b $F = 2 \rightarrow F' = c1$, a crossover between states $F' = 1$ and $F' = 2$

c $F = 2 \rightarrow F' = 2$

d $F = 2 \rightarrow F' = c2$, a crossover between states $F' = 1$ and $F' = 3$

e $F = 2 \rightarrow F' = c3$, a crossover between states $F' = 2$ and $F' = 3$

f $F = 2 \rightarrow F' = 3$

These transitions are illustrated in Figure 4.16. The measured energy level separations are given in Table 4.7, and the lifetime of the excited states is given in Table 4.8; dashes in these tables indicate peaks that were not observed.

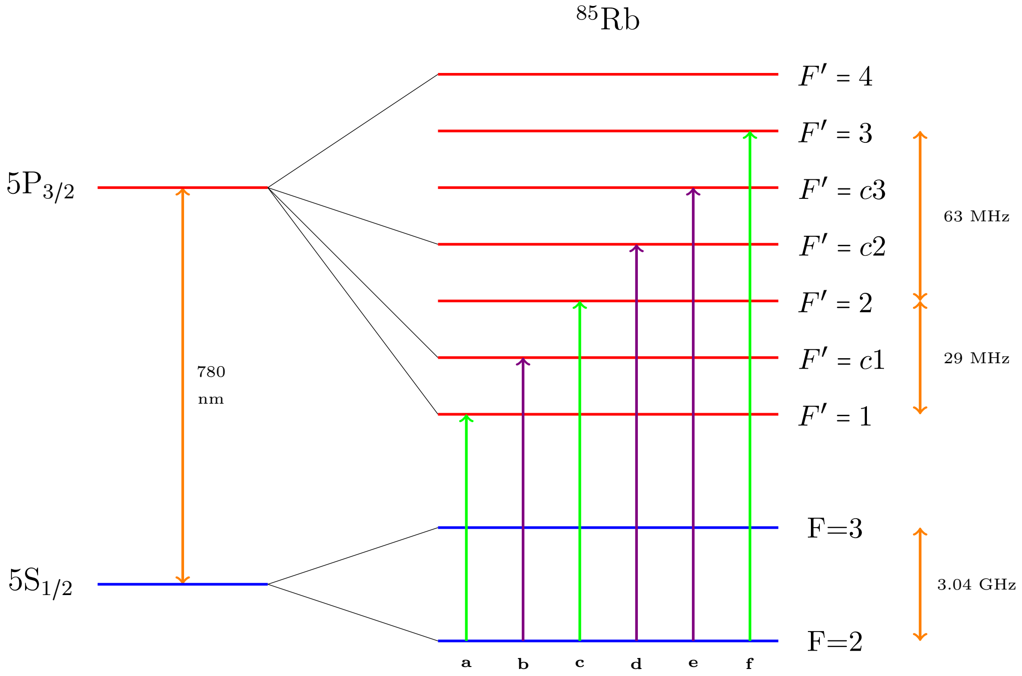

Figure 4.16: *Energy level diagram showing the* ^{85}Rb $F = 2$ *to* $F' = 1, 2, 3$ *transitions. Green arrows indicate normal transitions and purple arrows indicate crossover transitions. Transitions have been labelled* ***a*** *to* ***f*** *in accordance with the labels in Figure 4.15. Excited states* $F' = c1$, $F' = c2$ *and* $F' = c3$ *are crossover resonances.*

Table 4.7: *Excited state energy separation in units of frequency (MHz). Excited states **a** to **f** correspond to the peaks labelled in Figure 4.15.*

SAS arrangement	Peaks	Measured separation: Method A	Method B	Method C	Accepted value
Arrangement 1	**a–b**	–	–	–	15
	b–c	–	–	–	15
	c–d	–	–	–	17
	d–e	–	–	–	17
	e–f	32±1	32±3	32±1	32
Arrangement 2	**a–b**	–	–	–	15
	b–c	14±1	16±1	13±1	15
	c–d	22±1	24±5	21±4	17
	d–e	10±1	12±4	10±3	17
	e–f	31±1	35±1	30±1	32

Table 4.8: *Excited state lifetime in units of time (ns). Excited states **a** to **f** correspond to the peaks labelled in Figure 4.15.*

SAS arrangement	Peak	Excited state lifetime: Method A	Method B	Method C
Arrangement 1	**a**	–	–	–
	b	–	–	–
	c	–	–	–
	d	–	–	–
	e	16±2	16±2	16±2
	f	12±1	11±1	11±1
Arrangement 2	**a**	–	–	–
	b	24±5	22±3	26±1
	c	22±3	20±1	23±2
	d	15±3	9±7	7±9
	e	33±2	29±1	34±1
	f	21±3	19±3	22±2

^{87}Rb F=1 to F′=0,1,2 Absorption Spectrum

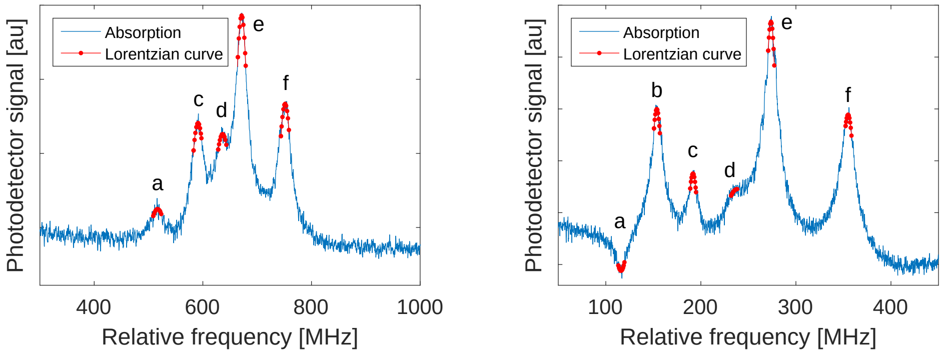

(a)

(b)

Figure 4.17: *Absorption spectrum of the* ^{87}*Rb* $F = 1$ *to* $F' = 0, 1, 2$ *transitions measured using arrangement 1 (a) and arrangement 2 (b) of the SAS setup. The hyperfine transitions are as follows.* ***a****:* $F = 1$ *to* $F' = 0$*.* ***b****:* $F = 1$ *to* $F' = c1$*, a crossover between* $F' = 0$ *and* $F' = 1$*.* ***c****:* $F = 1$ *to* $F' = 1$*.* ***d****:* $F = 1$ *to* $F' = c2$*, a crossover between* $F' = 0$ *and* $F' = 2$*.* ***e****:* $F = 1$ *to* $F' = c3$*, a crossover between* $F' = 1$ *and* $F = 2$*.* ***f****:* $F = 1$ *to* $F' = 2$*.*

The ^{87}Rb $F = 1$ to $F' = 0, 1, 2$ absorption spectrum is shown in Figure 4.17.

The following hyperfine transitions are allowed:

a $F = 1$ to $F' = 0$

b $F = 1$ to $F' = c1$, a crossover between states $F' = 0$ and $F' = 1$

c $F = 1$ to $F' = 1$

d $F = 1$ to $F' = c2$, a crossover between states $F' = 0$ and $F' = 2$

e $F = 1$ to $F' = c3$, a crossover between states $F' = 1$ and $F' = 2$

f $F = 1$ to $F' = 2$

These transitions are illustrated in Figure 4.18. The measured energy level separations are given in Table 4.9, and the lifetime of the excited states is given in Table 4.10; dashes in these tables indicate peaks that were not observed.

Transition **b** was not observed, we have therefore omitted the **a**–**b** energy level separation from Table 4.9. Instead we have provided the **a**–**c** energy level separation which is, according to the crossover resonance theory, twice the energy level separation of **a**–**b**.

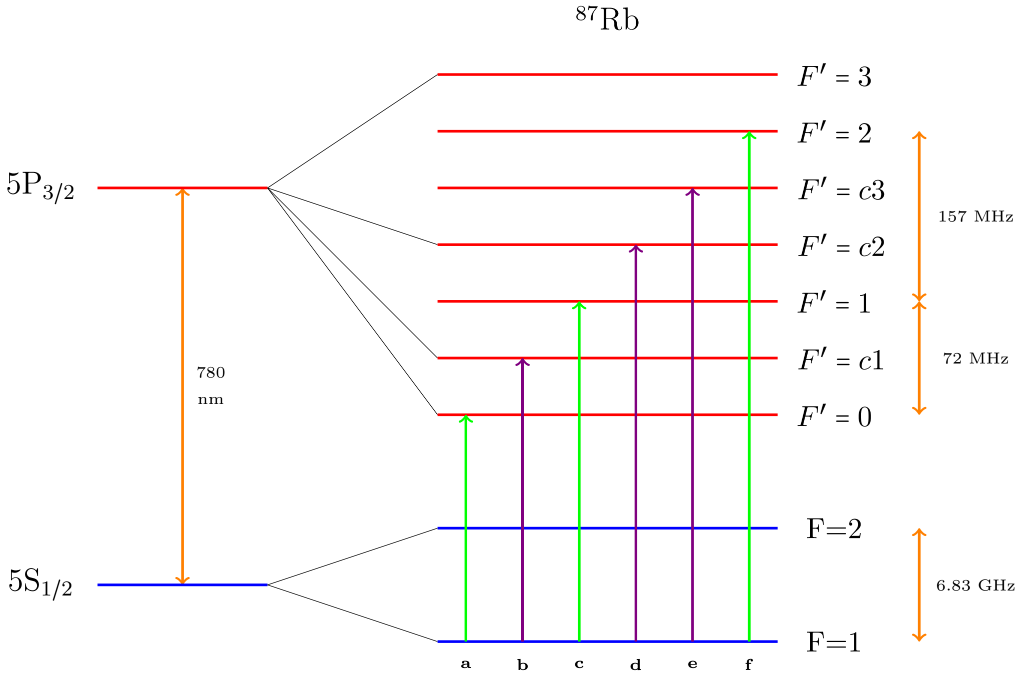

Figure 4.18: *Energy level diagram showing the* ^{87}*Rb* $F = 1$ *to* $F' = 0, 1, 2$ *transitions. Green arrows indicate normal transitions and purple arrows indicate crossover transitions. Transitions have been labelled* ***a*** *to* ***f*** *in accordance with the labels in Figure 4.17. Excited states* $F' = c1$, $F' = c2$ *and* $F' = c3$ *are crossover resonances.*

Table 4.9: *Excited state energy separation in units of frequency (MHz). Excited states **a** to **f** correspond to the peaks labelled in Figure 4.17.*

SAS arrangement	Peaks	Measured separation: Method A	Method B	Method C	Accepted value
Arrangement 1	**a–c**	72±3	73±1	72±1	72
	c–d	44±1	44±1	44±1	43
	d–e	34±2	34±1	33±1	36
	e–f	79±2	79±1	77±1	79
Arrangement 2	**a–b**	38±1	42± 1	34±2	36
	b–c	39±1	43±1	36±1	36
	c–d	49±5	54±1	43±5	43
	d–e	33±5	38±1	34±5	36
	e–f	81±1	91±1	77±1	79

Table 4.10: *Excited state lifetime in units of time (ns). Excited states **a** to **f** correspond to the peaks labelled in Figure 4.17.*

SAS arrangement	Peak	Excited state lifetime: Method A	Method B	Method C
Arrangement 1	**a**	6±1	5±1	6±1
	b	–	–	–
	c	11±1	11±1	11±1
	d	7±1	7±1	7±1
	e	15±1	15±1	15±1
	f	12±1	11±1	11±1
Arrangement 2	**a**	10±2	10±1	9±6
	b	21±1	18±2	21±1
	c	18±1	15±2	18±1
	d	4±4	5± 5	3±3
	e	23±3	21±2	24±2
	f	17±2	15±2	18±3

4.5 Summary

We have demonstrated a functional saturated absorption spectroscopy setup. The setup was arranged in two ways and measurements were carried out using each arrangement. Additionally, a Michelson interferometer was set up and used to calibrate all spectral measurements.

A few transitions were not observed due to broadening of spectral line widths, however, our measurements of the hyperfine energy level separations show good agreement with accepted values from literature (Steck, 2015; Steck, 2013). Initially it was noted that our estimations of the ground state separations were underestimated. These measurements were revised and the resulting estimations showed an improved agreement with the literature.

Although it is unclear as to what excited state lifetime the literature refers to, we have provided estimations of the lifetime of each excited state. Our estimations vary widely between excited states (4-37 ns) but the average lifetime for the $5S_{1/2}$ to $5P_{3/2}$ transitions was approximately 21±2 ns. This average is in agreement with the accepted value which is 26 ns. Since the inverse of the lifetime gives the linewidth, our estimations of the lifetime translates to an average linewidth of appropriately 47 MHz.

Our results prove that the techniques used in the acquisition and processing of the recorded data are suitable for future experiments of this nature.

Chapter 5

Zeeman Study

5.1 Introduction

In this chapter we present measurements of the Zeeman splitting of the $5S_{1/2}$ and $5P_{3/2}$ hyperfine energy levels of rubidium 85 and 87 (Wyngaard et al., 2018a; Wyngaard et al., 2018b).

To study the Zeeman effect we constructed a set of Helmholtz coils and added them to arrangement 2 of the saturated absorption spectroscopy setup described in Chapter 3. This was done to generate a uniform magnetic field in the region where the rubidium vapour cell was placed.

We measured the magnetic hyperfine spectra and estimated the energy separation between certain peaks. Additionally, theoretical values for the energy shifts that each magnetic hyperfine energy level undergoes were obtained by finding the eigenvalues of the the atomic and interaction energy Hamiltonian discussed in Chapter 2 (section 2.2.2). We used these energy shifts to find theoretical estimations for the peak separations and compared our experimental estimations to the theory.

We begin this chapter with a brief recap of atomic physics, followed by a discussion of the generation and calibration of the magnetic field. Results of the measurements of the Zeeman splitting are given thereafter.

5.2 Theory

As explained in Chapter 2 (section 2.2), energy levels at the hyperfine stage are specified by the F quantum number and these energy levels have associated magnetic energy levels, specified by the magnetic quantum number m. These magnetic levels are degenerate in the absence of an external magnetic field $\vec{B}$. In the presence of an external magnetic field this degeneracy is removed and each of the F levels then split into $2F + 1$ distinct magnetic levels, denoted by m_F, which have energies that are a function of the external magnetic field $\vec{B}$. This is known as the Zeeman effect. The splitting of the F energy levels results in a magnetic hyperfine structure. This structure is shown in Figure 5.1 for the $F = 1$ ground state and $F' = 1$ excited states of a hypothetical atom.

In our study of the Zeeman effect we exposed a rubidium vapour cell to an external magnetic field $\vec{B}$ using a pair of Helmholtz coils. A saturated absorption spectroscopy setup and linearly polarised light was used to probe the magnetic hyperfine energy levels of Rb, further details of the setup are given in Chapter 3. The use of linearly polarised light implies that only those transitions which satisfy the transition rule $\Delta m_F = 0$ are allowed (Svanberg, 2003b). These transitions are illustrated by solid arrows in Figure 5.1. The

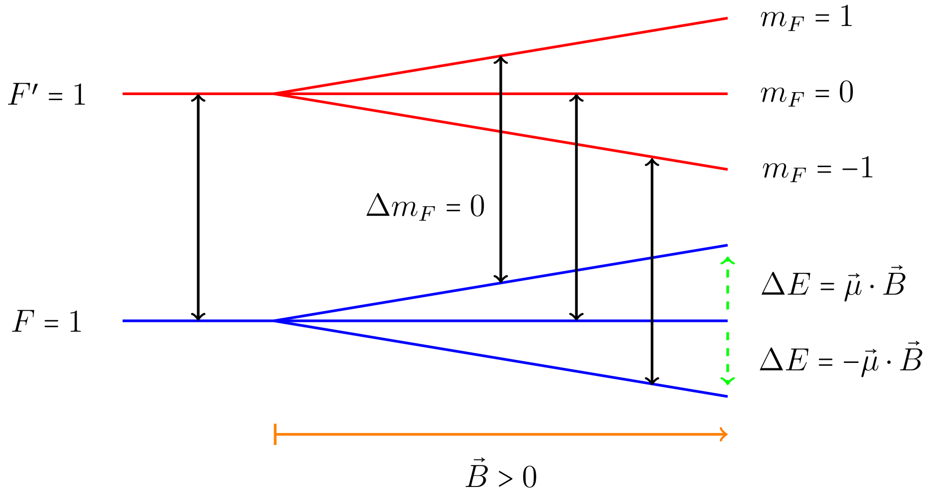

Figure 5.1: *The magnetic hyperfine structure of a ground* ($F = 1$) *and excited* ($F' = 1$) *energy level for a hypothetical atom. Due to an external magnetic field* $\vec{B}$, *each energy level splits into three* ($2F+1$) *magnetic sub-levels denoted by* m_F. *These levels are separated by an energy difference* ΔE *of* $\pm\vec{\mu} \cdot \vec{B}$ *(dashed green arrows), where* $\vec{\mu}$ *is the magnetic dipole moment of the atom. The solid black arrows indicate the allowed transitions when using linearly polarised light.*

occurrence of these transitions are dependent on the polarisation of the light and direction of the external magnetic field. In the case of linearly polarised light the direction of $\vec{B}$ must be perpendicular to the propagation of the light. Since the energy of the magnetic levels are dependent on the magnetic field strength, it is very important that the magnetic field be uniform across the rubidium vapour cell.

5.3 External Magnetic Field

The generation of a uniform external magnetic field was achieved using a pair of Helmholtz coils. We fabricated the coils by winding approximately 700 turns of copper wire around a block of mild steel of dimensions 100 millimetres (mm) in length and 40 mm in height and width. These coils were

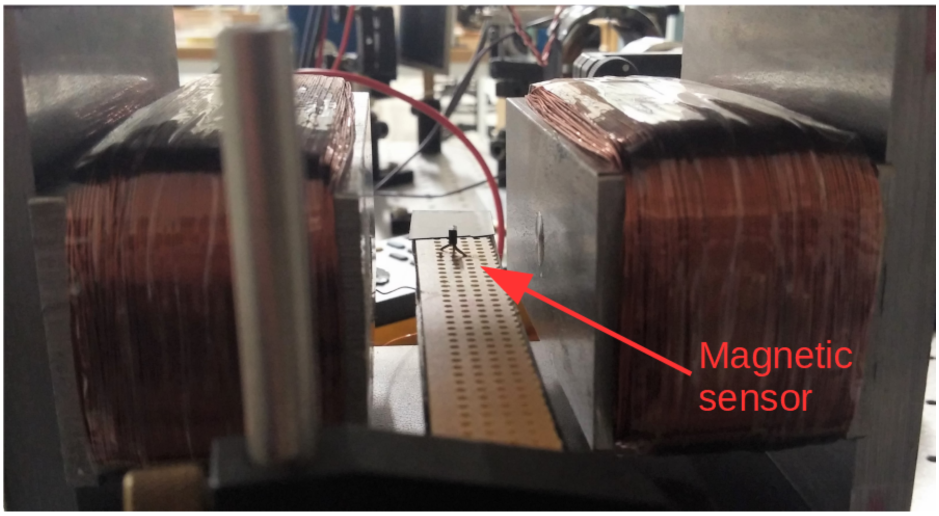

Figure 5.2: *Helmholtz coils pictured with an Allegro A1301 linear Hall-effect sensor that was used to calibrate the device. The sensor is positioned in the cavity between the coils.*

then enclosed by four plates of the same material. The coils are shown in Figure 5.2. The coils were designed to ensure that the magnetic field covers the entire rubidium vapour cell which is 72 mm in length and 25 mm in diameter[1].

Calibration of the Helmholtz coil was performed using an Allegro A1301 linear Hall-effect sensor[2] (in Figure 5.2). This sensor outputs a voltage that is linearly proportional to the magnetic field. The device is said to have an error of ±3%, this is indicated in the results section of this chapter by means of error bars in relevant plots. Before measuring the magnetic field between the Helmholtz coils, the magnetic field was measured approximately one metre away from the coils as well as outside of the laboratory. The magnetic field was found to be roughly 4 gauss at both measurement locations[3].

---

[1] These dimensions exclude the tip used to fill the cell. A diagram of the rubidium vapour cell is provided in Figure 3.9.

[2] (*A1301 and A1302: Continuous-Time Ratiometric Linear Hall Effect Sensor ICs* 2017)

[3] Since the geomagnetic field should be in region of 0.25 to 0.6 gauss, we accept that

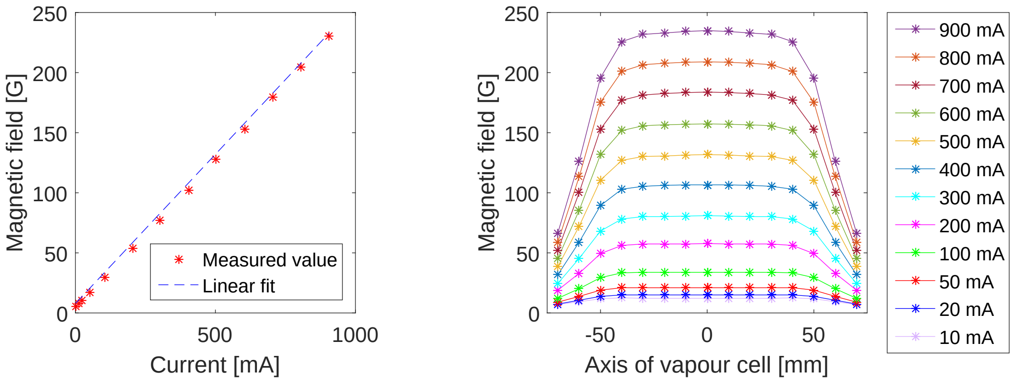

(a) (b)

Figure 5.3: *Magnetic field calibration results. (a): Magnetic field strength in gauss as a function of the current in milliamperes. (b): Magnetic field strength in gauss as a function of the position in millimetres along the axis of the rubidium vapour cell.*

The magnetic field was then measured at 10 mm intervals between the two coils, in the region where the rubidium vapour cell would be. We performed this measurement at several current settings, up to a magnetic field of roughly 230 gauss at a current of 900 milliamperes. Figure 5.3 gives the calibration results; Figure 5.3a shows the magnetic field as a function of current and Figure 5.3b shows the magnetic field as a function of position. As required, the field is uniform in the region of the rubidium vapour cell (-40 mm to 40 mm).

---

our current method for measuring the magnetic field is inaccurate and the sensor should be calibrated for future measurements. All measurements are therefore based on the total magnetic field which includes the geomagnetic field, applied field, and the accuracy of the sensor.

5.4 Data Processing

For this study we only recorded the absorption signal and the current passing through the Helmholtz coils, as opposed to Chapter 4 (section 4.3.2) where we recorded the ramp signal as well as the output from the Michelson interferometer. The reason for only recording the absorption signal is that observations of the magnetic hyperfine peaks required a laser frequency ramp signal that was very small, more so than what was required in the measurement of the ^{85}Rb hyperfine peaks. As a result, when calibrating the time axis of the magnetic hyperfine measurements the techniques described in Chapter 4 (section 4.3.2) failed to provide accurate results. The Michelson interferometer and ramp signals were therefore of no use. To get around this issue we set the ramp to a level which allowed us to capture at least two hyperfine peaks while retaining reasonable resolution of the magnetic hyperfine peaks. Since the distance between two hyperfine peaks (with no external magnetic field) is not only well documented but was measured in our saturated absorption spectroscopy experiment which preceded this study, we were able to perform the x-axis calibration by relating the peak separation in units of frequency to the peak separation in units of time. This is seen in Figure 5.4, where Figure 5.4a is the uncalibrated measurement and Figure 5.4b is the same measurement after calibration, note the differing x-axes.

A consequence of the small ramp signal was that the absorption signal had a very low signal-to-noise ratio. Multiple recordings had to be taken in order to reduce the noise. As shown in Figure 5.5, the signal-to-noise ratio was improved significantly after the recordings were averaged and filtered. We noted no significant improvement in the uncertainty of locating peaks, it remained at $\approx \pm 1\%$, however, the visibility of the peaks was very much

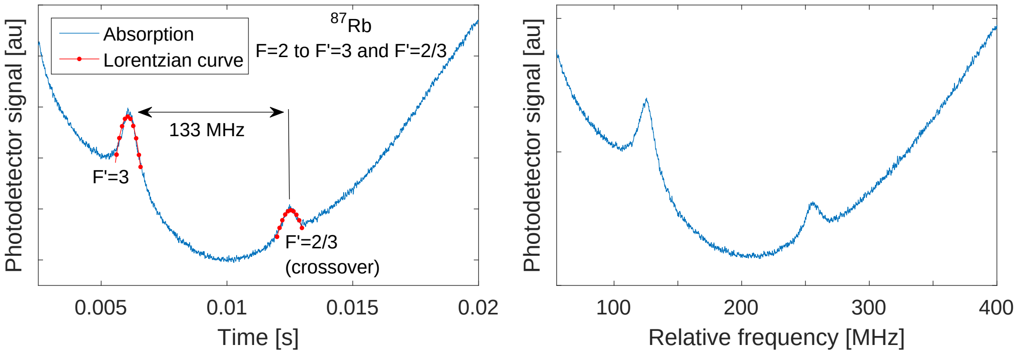

(a) (b)

Figure 5.4: *Uncalibrated (a) and calibrated (b) measurements of the* ^{87}*Rb* $F = 2$ *to* $F' = 3$ *and* $F' = {}^{2}/_{3}$ *(crossover resonance) hyperfine energy level transitions. The distance between the peaks is given in units of frequency and the dotted red lines correspond to Lorentzian curves that have been fitted to characterise the peaks.*

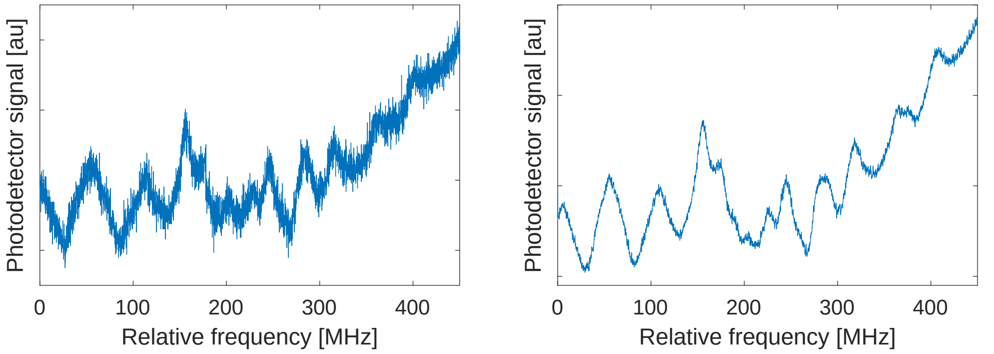

(a) (b)

Figure 5.5: *Single (a) versus averaged and filtered (b) measurement of the magnetic hyperfine energy levels of Rb. The average was obtained using 5 measurements.*

improved. The uncertainty is indicated as error bars in the relevant plots of the results section in this chapter.

The process for determining the distance between two peaks is similar to that of the hyperfine measurements. We first located the relevant peaks by eye and then fitted the peaks with Lorentzian curves. From the Lorentzian function we obtained estimates of the energy separation as a function of the magnetic field. As we will discuss in the next section, measuring the energy separation between two peaks does not translates directly to the Zeeman shift of the excited states, since there is also a Zeeman shift occurring in the ground state.

5.5 Results

We now compare the experimentally measured Zeeman shift to the predicted shift. The measured shifts were estimated by tracking two magnetic sublevels as $\vec{B}$ was increased linearly. The predicted shifts were computed by finding the eigenvalues of the atomic plus interaction energy Hamiltonian and then determining the energy difference between various magnetic hyperfine energy levels as a function of the magnetic field.

5.5.1 Computational Results

The figures that follow are plots of the computed values for the theoretical shift in energy that each magnetic hyperfine energy level undergoes. These values were found by finding the eigenvalues of the atomic and interaction energy Hamiltonian. The shifts in energy have been computed for a magnetic field that ranges from 0 to 180 gauss in order to keep in-line with the magnetic field range we used for the experimentally measured shift in energy. A derivation of the Zeeman splitting of the hyperfine energy levels is given in Appendix A, the calculations follow that of Pethick and Smith (2008).

Figure 5.6 shows the shift in energy for the $5S_{1/2}$ (a) and $5P_{3/2}$ (b) magnetic hyperfine levels of rubidium 85. Due to the higher F quantum number associated with rubidium 85 energy levels, the number of magnetic energy levels is larger than that of rubidium 87. The higher F quantum number results from the higher nuclear spin quantum number $I = 5/2$.

Figure 5.7 shows the shift in energy for the $5S_{1/2}$ (a) and $5P_{3/2}$ (b) magnetic hyperfine levels of rubidium 87 which has a lower nuclear spin quantum number $I = 3/2$ than rubidium 85.

From the computation we found that certain magnetic energy levels originating from one hyperfine energy level would shift to the point where they crossed with magnetic energy levels originating from a different hyperfine energy level. This was difficult to investigate since we observe normal as well as crossover resonances in the spectra that are discussed in the next section. However, the theory suggests that this level crossing is allowed as long as the value of the magnetic quantum number of the levels involved are not the same (Svanberg, 2003c).

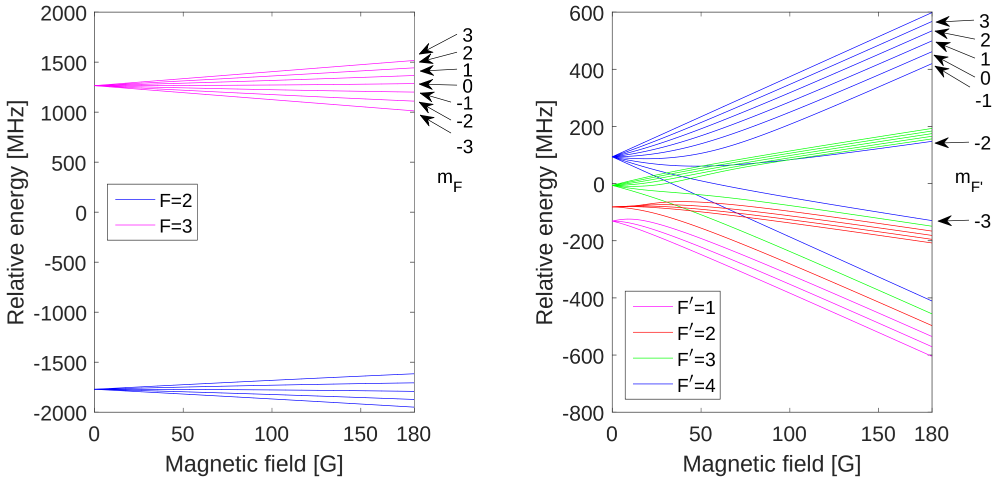

(a) (b)

Figure 5.6: *Theoretical Zeeman shifts for the* $5S_{1/2}$ *(a) and* $5P_{3/2}$ *(b) magnetic hyperfine levels of rubidium 85. The energy level from which each set of magnetic sub-levels originates is given by the line colour associated with the F quantum number in the legend. Only the transitions which we have analysed experimentally have been labelled.*

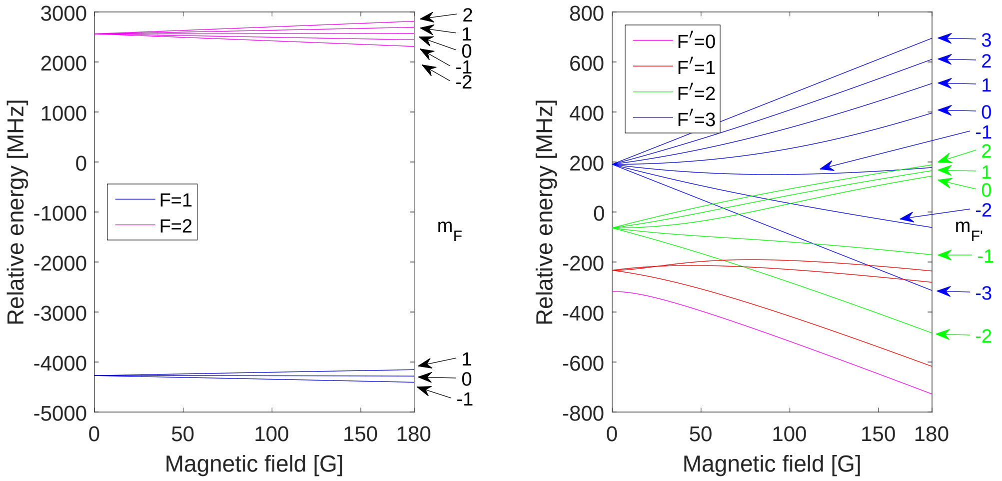

(a) (b)

Figure 5.7: *Theoretical Zeeman shifts for the* $5S_{1/2}$ *(a) and* $5P_{3/2}$ *(b) magnetic hyperfine levels of rubidium 87. The energy level from which each set of magnetic sub-levels originates is given by the line colour associated with the F quantum number in the legend. Only the transitions which we have analysed experimentally have been labelled.*

5.5.2 Experimental Results

Recall that we measure the spectra by sweeping the laser frequency over the region of resonance and measure the absorption of the laser. To understand the measurement we have made, consider the energy levels shown in Figure 5.1; for a fixed magnetic field we get the sequence of plots in Figure 5.8. In the figure when $B = 0$ (no external magnetic field) we get a single absorption peak corresponding to a transition from $F = 1$ to $F' = 1$. For $B > 0$ we get three peaks corresponding to transitions from $m_F = 1$ to $m_{F'} = 1$ (peak **a**), $m_F = 0$ to $m_{F'} = 0$ (peak **b**), and $m_F = -1$ to $m_{F'} = -1$ (peak **c**) assuming that the level splitting are all different.

We then measure the spacing between the peaks. It is this spacing that we compare with the theory. The magnetic shifting of both the ground and excited state will affect the spacing between absorption peaks. Thus in order to compare our measurements to theory we had to extract the same information from the theoretical plots in Figure 5.6 and 5.7.

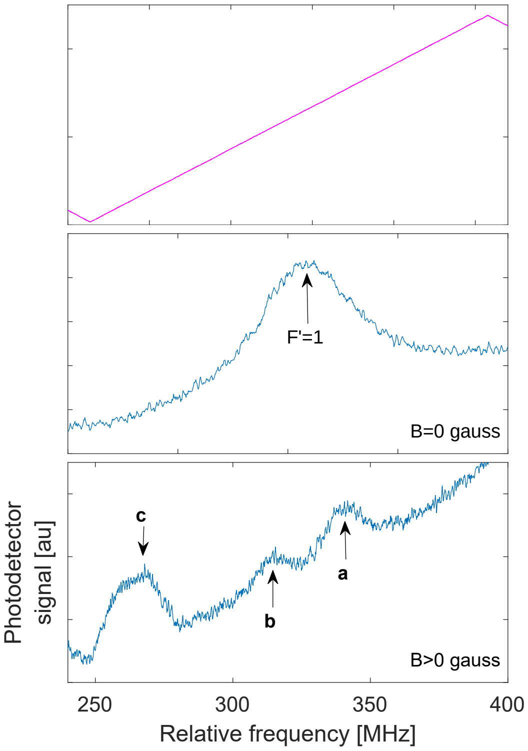

Figure 5.8: *The top plot shows the laser frequency sweep. The middle shows the hyperfine peak corresponding to a transition between a ground* ($F = 1$) *and excited* ($F' = 1$) *energy level in a hypothetical atom when the external magnetic field* $\vec{B}$ *is zero. The bottom plot shows the magnetic hyperfine peaks corresponding to a transition between a ground* ($F = 1$) *and excited* ($F' = 1$) *energy level in a hypothetical atom when the external magnetic field* $\vec{B}$ *is non-zero, three peaks are observed.*

Rubidium 87 F=1 to F'=2 Magnetic Hyperfine Structure

Figure 5.9 shows the energy level structure for the ^{87}Rb $F = 1$ to $F' = 2$ transition. As the magnetic field increases the $F' = 2$ hyperfine peak splits into its magnetic sub-levels as shown. The arrows show the transitions that we observe, which are the allowed transitions for linearly polarised light, i.e. $\Delta m_F = 0$.

Figure 5.10 shows a sequence of measurements of the ^{87}Rb $F = 1$ to $F' = 2$ magnetic hyperfine absorption spectrum at various magnetic fields. The labels **a** and **c** correspond to the transitions labelled in Figure 5.9. Peak $F' = 1/2$ is due to a crossover resonance which occurs as a consequence of the saturated absorption spectroscopy setup, explained in Chapter 2 (section 2.5). The separation between the $F' = 1/2$ and $F' = 2$ peaks at $B = 0$ (no magnetic field) was used to calibrate the x-axis, since we know this from previous studies (Chapter 4). At higher magnetic fields we noted that a magnetic peaks arising from both the $F' = 1/2$ and $F' = 2$ peaks had shifted towards each other to the point where we were unable to resolve them, best illustrated

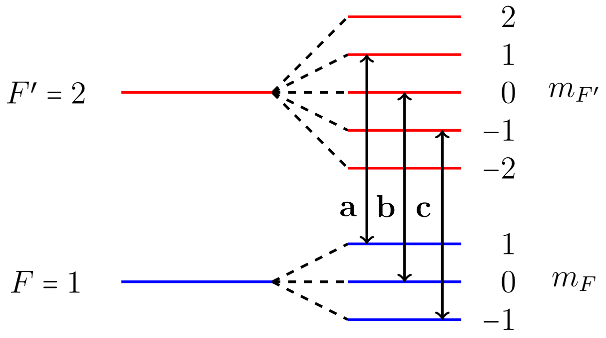

Figure 5.9: *Transitions (black arrows) between magnetic energy levels within the $F = 1$ and $F' = 2$ magnetic hyperfine structure of rubidium 87, when there is no change in the magnetic quantum number ($\Delta m_F = 0$).*

in Figure 5.14. As the magnetic field was increased further the two peaks separated, however, it was difficult to determine whether the two peaks had passed each other or returned to where they originated. For this analysis we

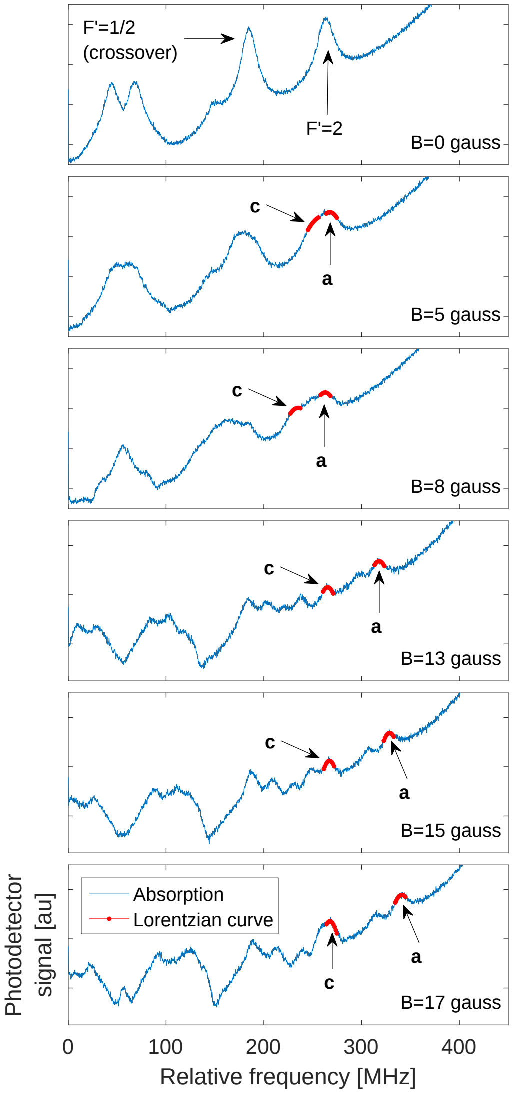

Figure 5.10: *Magnetic hyperfine absorption spectrum corresponding to the* ^{87}Rb $F = 1$ *to* $F' = 2$ *transition. The red lines correspond to Lorentzian curves fitted to the peaks which correspond to the* $F = 1$ $m_F = 1$ *to* $F' = 2$ $m_{F'} = 1$ *(peak* ***a****) and* $F = 1$ $m_F = -1$ *to* $F' = 2$ $m_{F'} = -1$ *(peak* ***c****) transitions in order to track their shift in energy. The legend and axes labels at the bottommost plot apply to each plot above it.*

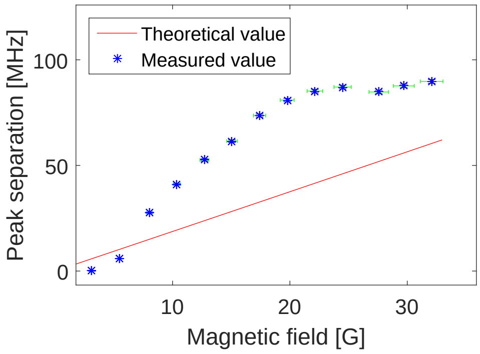

Figure 5.11: *Peak separation as a function of the magnetic field. The blue stars represent the experimentally obtained separation between peaks **a** and **c** in Figure 5.10, and the vertical and horizontal green bars indicate the uncertainty in the measurement. The red curve represents the theoretically obtained difference between transitions **a** and **c** in Figure 5.9.*

do not make measurements at magnetic fields beyond this level.

We tracked the peaks corresponding to the ^{87}Rb $F = 1$ $m_F = 1$ and $m_F = -1$ to $F' = 2$ $m_{F'} = 1$ and $m_{F'} = -1$ transitions (**a** and **c** in Figure 5.9) respectively, and estimated their separation as a function of the magnetic field. Figure 5.11 shows the estimated and theoretical peak separation. The theory appears to underestimate the shift in the energy that separates these magnetic levels.

Rubidium 87 F=2 to F'=3 Magnetic Hyperfine Structure

Figure 5.12 shows the energy level structure for the ^{87}Rb $F = 2$ to $F' = 3$ transition. As the magnetic field increases the $F' = 3$ hyperfine peak splits into its magnetic sub-levels as shown. The transitions that we observe are those indicated by the arrows in Figure 5.12, these are the allowed transitions for linearly polarised light, i.e. $\Delta m_F = 0$.

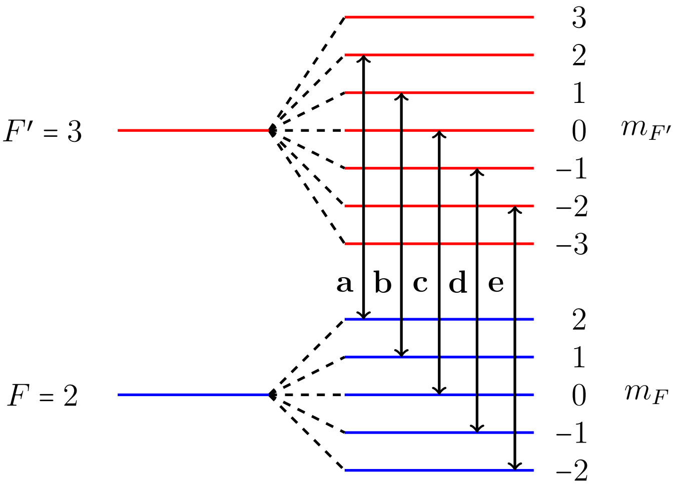

Figure 5.12: *Transitions (black arrows) between magnetic energy levels within the* $F = 2$ *and* $F' = 3$ *magnetic hyperfine structure of rubidium 87, where there is no change in the magnetic quantum number* ($\Delta m_F = 0$)*.*

Figure 5.13 shows a sequence of measurements of the ^{87}Rb $F = 2$ to $F' = 3$ magnetic hyperfine absorption spectrum at various magnetic fields. Labels **a** to **e** correspond to the labelled transitions in Figure 5.12. Peak $F' = {}^{2}\!/\!{}_{3}$ is due to a crossover resonance. The separation between the $F' = {}^{2}\!/\!{}_{3}$ and $F' = 3$ peaks at $B = 0$ (no magnetic field) was used to calibrate the x-axis, as previously done. Similarly to the spectrum discussed earlier, higher magnetic fields showed magnetic peaks arising from both the $F' = {}^{2}\!/\!{}_{3}$ and $F' = 3$ peaks shifting towards each other to the point where we were unable to resolve them. This is shown in Figure 5.14 where we see that peak **e** merges with peak **1** at lower magnetic fields and then separates at higher magnetic fields.

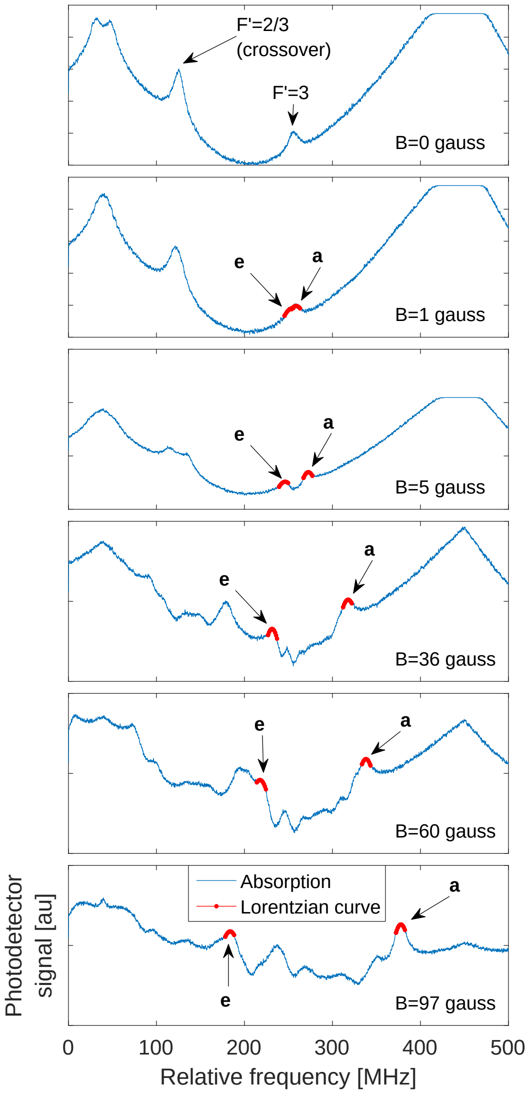

Figure 5.13: *Magnetic hyperfine absorption spectrum corresponding to the* ^{87}Rb $F = 2$ *to* $F' = 3$ *transition. The red lines correspond to Lorentzian curves fitted to the peaks which correspond to the* $F = 2$ $m_F = 2$ *to* $F' = 3$ $m_{F'} = 2$ *(peak* ***a****) and* $F = 2$ $m_F = -2$ *to* $F' = 3$ $m_{F'} = -2$ *(peak* ***e****) transitions in order to track their shift in energy. The legend and axes labels at the bottommost plot apply to each plot above it.*

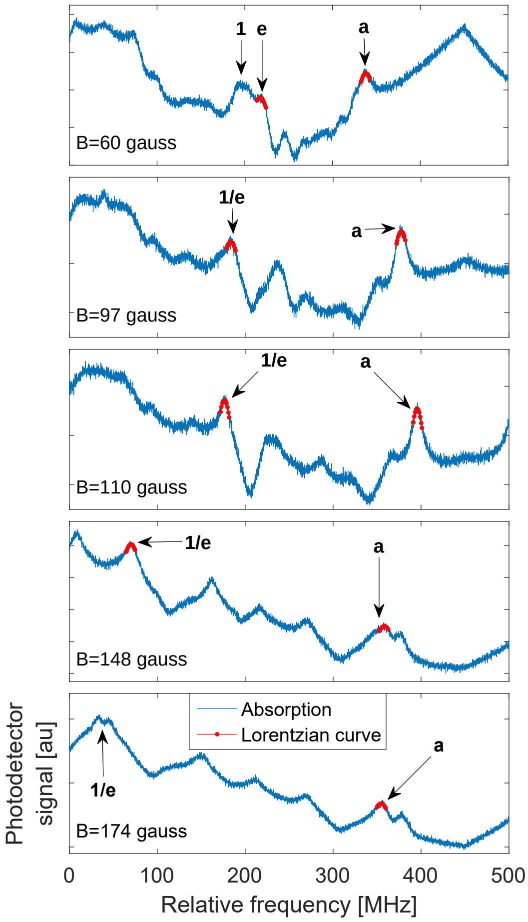

Figure 5.14: *Continuation of Figure 5.13 demonstrating the merging and possible separation of two peaks,* ***e*** *and* ***1*** *from different hyperfine magnetic energy level transitions at intermediate and high magnetic fields respectively. The legend and axes labels at the bottommost plot apply to each plot above it.*

It was noted that there are more peaks originating from the $F' = 3$ hyperfine peak than the theory suggests, we have labelled them numerically in Figure 5.15a. This anomaly has yet to be investigated but the extra peaks may be due crossover resonances which occur as a consequence of the saturated absorption spectroscopy setup.

Figure 5.15a shows the peaks we have tracked for our analysis; alphabetically labelled peaks are the magnetic hyperfine transitions that were tracked for a comparison with our theoretical analysis, and numerical labels have been assigned to peaks which we assumed were not part of the magnetic sub-levels. The alphabetically labelled peaks have been chosen in a way that tends to better match the experimental measurements with the theory; these labels correspond to the transitions in Figure 5.12.

Figure 5.15b and 5.15c shows the estimated and theoretical peak separation. Figure 5.15b corresponds to the peak separation of the $F = 2$ $m_F = 2$ and $m_F = -2$ to $F' = 3$ $m_{F'} = 2$ and $m_{F'} = -2$ transitions (peaks **a** and **e** in Figure 5.15a) and Figure 5.15c corresponds to the $F = 2$ $m_F = 1$ and $m_F = -1$ to $F' = 3$ $m_{F'} = 1$ and $m_{F'} = -1$ transitions (peaks **b** and **d** in Figure 5.15a). In both cases the theory seems to overestimate the shift in the energy that separates these magnetic levels.

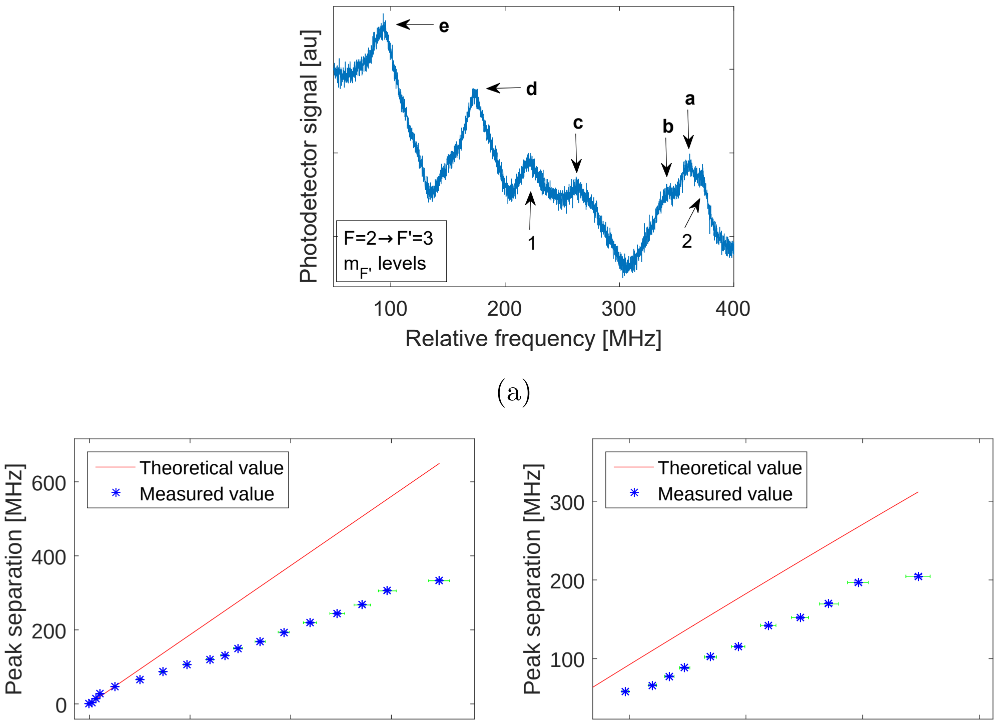

(a)

(b)

(c)

Figure 5.15: *(a):* $^{87}Rb\ F = 2$ *to* $F' = 3$ *magnetic hyperfine absorption spectrum at a magnetic field of 86 gauss. The peaks which we believe do not correspond to the normally allowed transitions have been labelled numerically. (b): Peak separation as a function of the magnetic field for transitions* $^{87}Rb\ F = 2\ m_F = 2$ *to* $F' = 3\ m_{F'} = 2$ *(peak* ***a****) and* $F = 2\ m_F = -2$ *to* $F' = 3\ m_{F'} = -2$ *(peak* ***e****). (c): Peak separation as a function of the magnetic field for transitions* $^{87}Rb\ F = 2\ m_F = 1$ *to* $F' = 3\ m_{F'} = 1$ *(peak* ***b****) and* $F = 2\ m_F = -1$ *to* $F' = 3\ m_{F'} = -1$ *(peak* ***d****). The blue stars represent the experimentally obtained peak separation, the red line represents the theoretically obtained separation, and the vertical and horizontal green bars are uncertainties.*

After analysing the plots in Figure 5.15 more carefully, we compared the measurements of the separation between peaks **a** and **e**[4] in Figure 5.15a to other possible transitions in the theoretical calculation. Figure 5.16 shows the measurements (blue stars) as well as the theoretical difference between the ^{87}Rb $F = 2$ $m_F = 2$ to $F' = 3$ $m_{F'} = 2$ and $F = 2$ $m_F = -2$ to $F' = 3$ $m_{F'} = -2$ transitions (red curve) and the ^{87}Rb $F = 2$ $m_F = 1$ to $F' = 3$ $m_{F'} = 1$ and $F = 2$ $m_F = -1$ to $F' = 3$ $m_{F'} = -1$ transitions (green curve). As seen in the figure, the measurements match up very well with the green curve. This leaves us with the question as to what the other peaks between **a** and **e** in Figure 5.15a are. At this stage we are unable to answer this without more investigation.

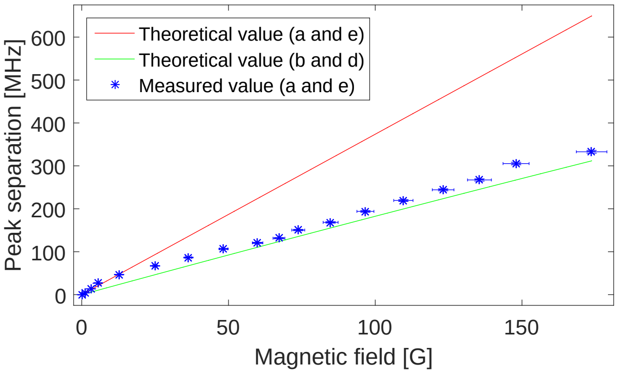

Figure 5.16: *Peak separation as a function of the magnetic field. The blue stars represent the experimentally obtained separation between peaks* ***a*** *and* ***e*** *in Figures 5.15a, and the vertical and horizontal bars indicate the uncertainty in the measurements. The red curve represents the theoretically obtained difference between the* ^{87}*Rb* $F = 2$ $m_F = 2$ *to* $F' = 3$ $m_{F'} = 2$ *and* $F = 2$ $m_F = -2$ *to* $F' = 3$ $m_{F'} = -2$ *transitions,* ***a*** *and* ***e*** *respectively in Figure 5.12. The green curve represents the theoretically obtained difference between the* ^{87}*Rb* $F = 2$ $m_F = 1$ *to* $F' = 3$ $m_{F'} = 1$ *and* $F = 2$ $m_F = -1$ *to* $F' = 3$ $m_{F'} = -1$ *transitions,* ***b*** *and* ***d*** *respectively in Figure 5.12.*

---

[4] Peaks **a** and **e** here should not be confused with **a** and **e** in Figure 5.12.

Rubidium 85 F=3 to F'=4 Magnetic Hyperfine Structure

Figure 5.17 shows the energy level structure for the ^{85}Rb $F = 3$ to $F' = 4$ transition. As the magnetic field increases the $F' = 4$ hyperfine peak splits into its magnetic sub-levels as shown. The arrows show the observed transitions, which correspond to transitions allowed when using linearly polarised light, i.e. $\Delta m_F = 0$.

Figure 5.18 shows a sequence of measurements of the ^{87}Rb $F = 3$ to $F' = 4$ absorption spectra at various magnetic fields. The peaks labelled **a** through **g** correspond to the transitions labelled in Figure 5.17. The separation between the $F' = {}^{3}\!/\!_{4}$ and $F' = 4$ peaks at $B = 0$ (no magnetic field) was used to calibrate the x-axis, peak $F' = {}^{3}\!/\!_{4}$ is due to a crossover resonance. Higher magnetic

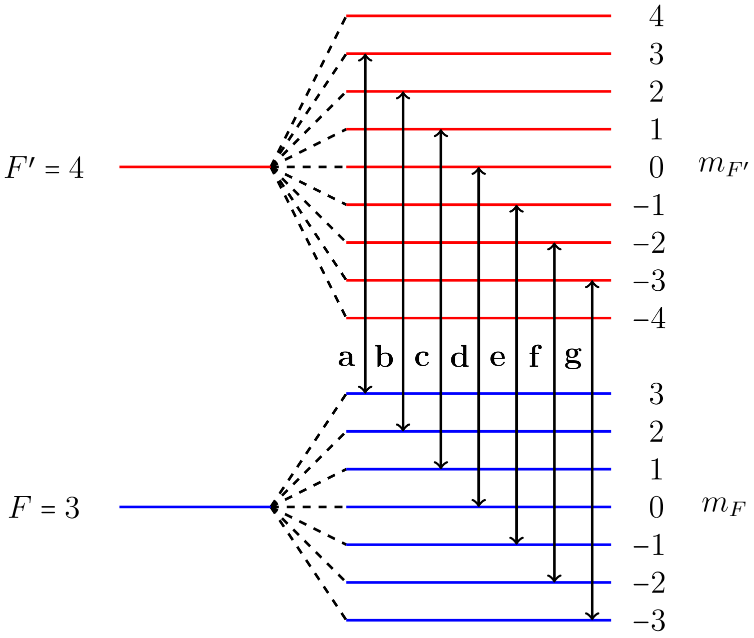

Figure 5.17: *Transitions (black arrows) between magnetic energy levels within the $F = 3$ and $F' = 4$ magnetic hyperfine structure of rubidium 85, where there is no change in the magnetic quantum number ($\Delta m_F = 0$).*

fields again showed merging of magnetic peaks arising from both the $F' = {}^{3}\!/\!{}_{4}$ and $F' = 4$ peaks similar to that of Figure 5.14.

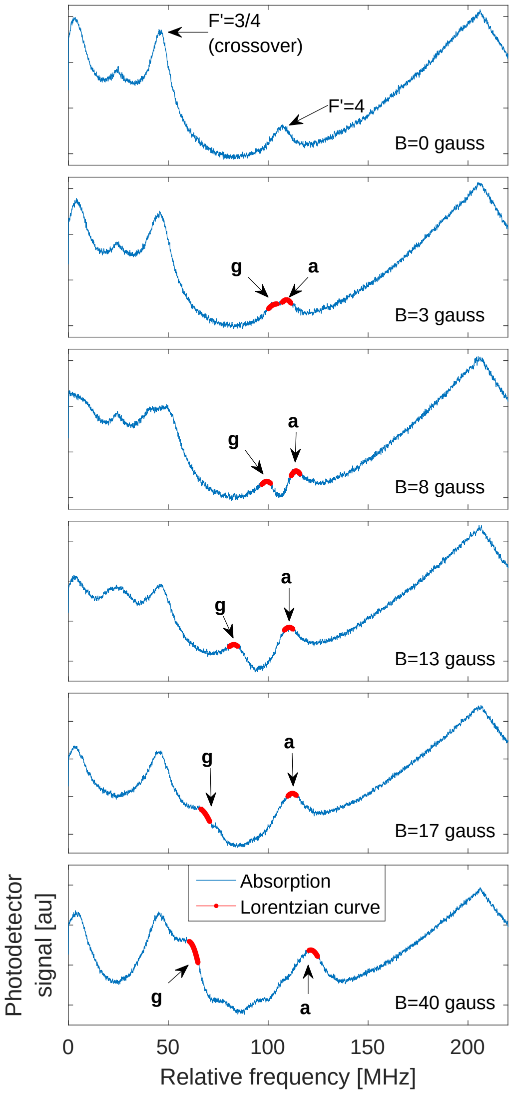

Figure 5.18: *Magnetic hyperfine absorption spectrum corresponding to the* ^{85}Rb $F = 3$ *to* $F' = 4$ *transition. The red lines correspond to Lorentzian curves fitted to the peaks corresponding to the* $F = 3$ $m_F = 3$ *to* $F' = 4$ $m_{F'} = 3$ *(peak* ***a****) and* $F = 3$ $m_F = -3$ *to* $F' = 4$ $m_{F'} = -3$ *(peak* ***g****) transitions in order to track their shift in energy. The legend and axes labels at the bottommost plot apply to each plot above it.*

Figure 5.19a shows the peaks we have tracked for our analysis, these peaks correspond to the alphabetically labelled transitions in Figure 5.17. We tracked these peaks and estimated their separation as a function of the magnetic field. Figure 5.19 shows the estimated and theoretical peak separation. Figure 5.19b corresponds to the peak separation of the $F = 3$ $mF = 3$ and $mF = -3$ to $F' = 4$ $mF' = 3$ and $mF' = -3$ transitions (peaks **a** and **g** in Figure 5.19a), Figure 5.19c corresponds to the $F = 3$ $mF = 2$ and $mF = -2$ to $F' = 4$ $mF' = 2$ and $mF' = -2$ transitions (peaks **b** and **f** in Figure 5.19a), and Figure 5.19d corresponds to the $F = 3$ $mF = 1$ and $mF = -1$ to $F' = 4$ $mF' = 1$ and $mF' = -1$ transitions (peaks **c** and **e** in Figure 5.19a). All of our measurements suggest that the theory overestimates the shift in the energy that separates these magnetic levels.

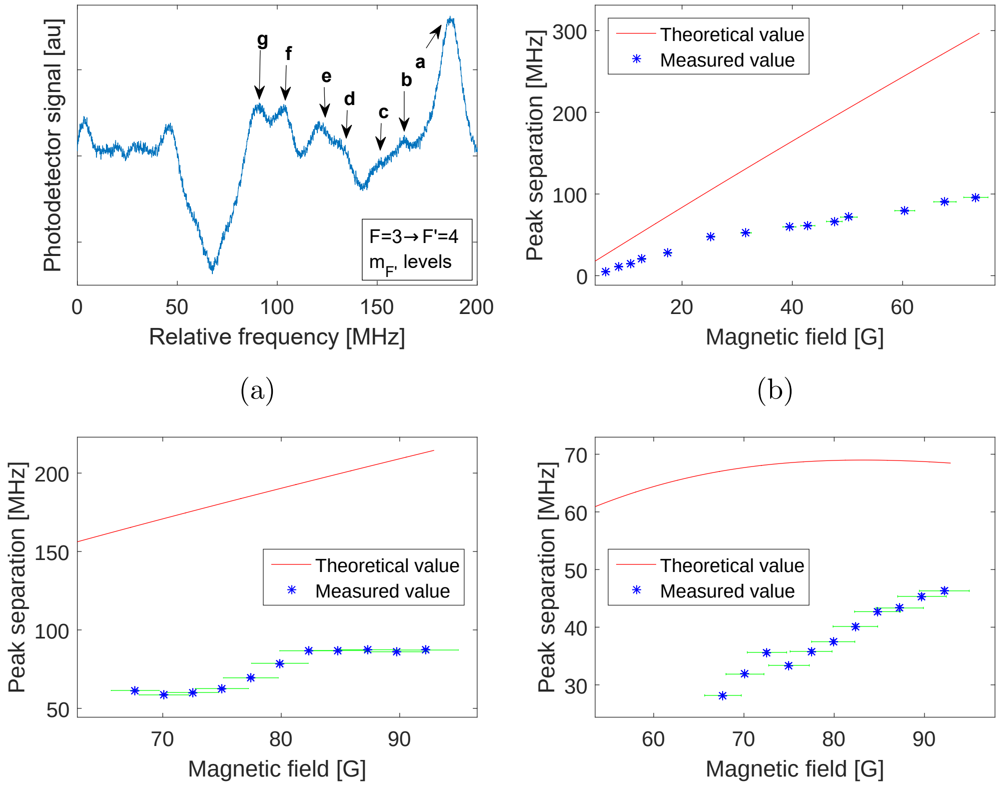

(a) (b)

(c) (d)

Figure 5.19: *(a): ^{85}Rb $F = 3$ to $F' = 4$ magnetic hyperfine absorption spectrum at a magnetic field of 81 gauss. (b): Peak separation as a function of the magnetic field between transitions ^{85}Rb $F = 3$ $m_F = 3$ to $F' = 4$ $m_{F'} = 3$ (peak **a**) and $F = 3$ $m_F = -3$ to $F' = 4$ $m_{F'} = -3$ (peak **g**). (c): Peak separation as a function of the magnetic field between transitions ^{85}Rb $F = 3$ $m_F = 2$ to $F' = 4$ $m_{F'} = 2$ (peak **b**) and $F = 3$ $m_F = -2$ to $F' = 4$ $m_{F'} = -2$ (peak **f**). (d): Peak separation as a function of the magnetic field between transitions ^{85}Rb $F = 3$ $m_F = 1$ to $F' = 4$ $m_{F'} = 1$ (peak **c**) and $F = 3$ $m_F = -1$ to $F' = 4$ $m_{F'} = -1$ (peak **e**). The blue stars represent the experimentally obtained peak separation, the red line represents the theoretically obtained separation, and the vertical and horizontal green bars are uncertainties.*

As with Figure 5.16, we analysed the plots in Figure 5.19 and compared the measurements of the separation between peaks **a** and **g**[5] in Figure 5.19a to other possible transitions in the theoretical calculation. Figure 5.20 shows the measurements (blue stars) as well as the theoretical difference between the ^{85}Rb $F = 3$ $m_F = 3$ to $F' = 4$ $m_{F'} = 3$ and $F = 3$ $m_F = -3$ to $F' = 4$ $m_{F'} = -3$ transitions (red curve), the ^{85}Rb $F = 3$ $m_F = 2$ to $F' = 4$ $m_{F'} = 2$ and $F = 3$ $m_F = -2$ to $F' = 4$ $m_{F'} = -2$ transitions (green curve), and the ^{85}Rb $F = 3$ $m_F = 1$ to $F' = 4$ $m_{F'} = 1$ and $F = 3$ $m_F = -1$ to $F' = 4$ $m_{F'} = -1$ transitions (pink curve). From the figure we see that the measurements are best matched with the pink curve. Again, this leaves us questioning what the other peaks between **a** and **g** in Figure 5.19a are; further investigation is required.

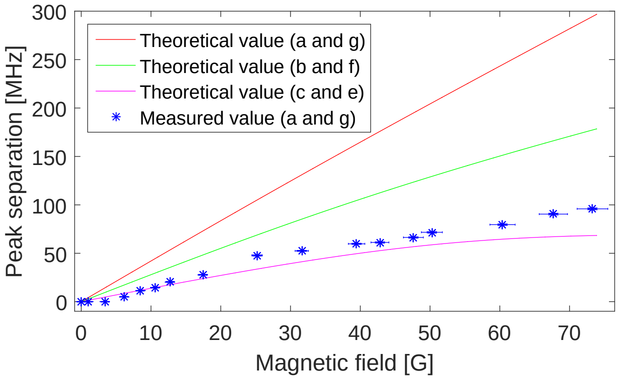

Figure 5.20: *Peak separation as a function of the magnetic field. The blue stars represent the experimentally obtained separation between peaks* ***a*** *and* ***g*** *in Figure 5.19a, and the uncertainty in the measurements is indicated by vertical and horizontal bars. The red curve represents the theoretically obtained difference between transitions* ***a*** *and* ***g*** *in Figure 5.17, the green curve represents the theoretically obtained difference between transitions* ***b*** *and* ***f*** *in Figure 5.17, and the pink curve represents the theoretically obtained difference between transitions* ***c*** *and* ***e*** *in Figure 5.17.*

---

[5] Peaks **a** and **g** here should not be confused with **a** and **g** in Figure 5.17.

5.6 Summary

We have demonstrated an experiment which was used to investigate the Zeeman effect by measuring the magnetic hyperfine spectra of rubidium 85 and 87. From our calibration of the Helmholtz coils we see that the magnetic field was uniform in the region of the rubidium cell, as intended.

Our calculation of the theoretical shift in energy of the magnetic hyperfine levels shows agreement with calculations performed by various authors. Our initial estimations of the energy separation between magnetic hyperfine energy levels show large variations when compared to the theoretical values. Measurements of the energy separation between magnetic hyperfine energy levels of rubidium 85 show the widest variation. However, by comparing a measurement of the peak separation between a specific pair of transitions with the theoretical difference between other pairs of transitions that differed to our initial assumptions we observed some agreement between the theory and our experiment.

Additionally, magnetic hyperfine energy levels that were not predicted by the theory have been observed. These show up as extra peaks which may be due to crossover resonances that occur as a consequence of the saturated absorption spectroscopy setup.

In summary, a more thorough analysis is required in order to properly compare peak separations and to better understand the level crossings between normal and crossover resonances as this may explain the extra peaks.

Chapter 6

Laser Frequency Locking Results

6.1 Introduction

In this chapter we discuss the experimental investigation of techniques for locking the frequency of the light from a tunable external cavity diode laser to an atomic transition of rubidium. A theoretical analysis of the same experiment was done by Opeolu et al. (2018). Their simulations were based on our saturated absorption spectroscopy results given in Chapter 4.

Locking the frequency of the light from a laser is required for laser cooling of atoms, and Doppler cooling is a commonly used technique for cooling a gas down to the sub-Kelvin temperature range. Recall from Chapter 2 (Section 2.3) that this technique uses the velocity-dependent absorption of room temperature atoms to reduce the average velocity of the atoms as the laser light frequency is tuned toward resonance. The reduction in velocity reduces the kinetic energy which translates to a lower temperature, hence the name Doppler cooling. Thus crucial in Doppler cooling is keeping the laser frequency detuned to a precise value and this is where locking the frequency of the light from the laser is required.

In Section 6.2 a brief description of feedback control of our system is given, followed by the locking procedure in Section 6.3. Results are given in Section 6.4.

6.2 Theory of Feedback Control

Figure 6.1 shows the complete setup of the control system for side locking. It consists of an external cavity diode laser (ECDL), a saturated absorption spectroscopy (SAS) setup as the feedback network, and a proportional-integral-derivative (PID) controller. The PID controller contains an amplifier block (proportional), integrator block (integral), and a differentiator block (derivative); the differentiator block in our case is set to one and has no effect. The ECDL contains a piezoelectric actuator, this is a second-order system. The transfer function of each block is also given in Figure 6.1.

The frequency response of the feedback path is the absorption spectra of rubidium and consists of a number of Lorentzian peaks as observed in the two preceding chapters. We want to lock the frequency of the light from the laser to the side of one of these peaks. A single Lorentzian peak is shown in Figure 6.2.

The control system operates as follows. A portion of the light from the ECDL is directed through the SAS setup where the light interacts with room

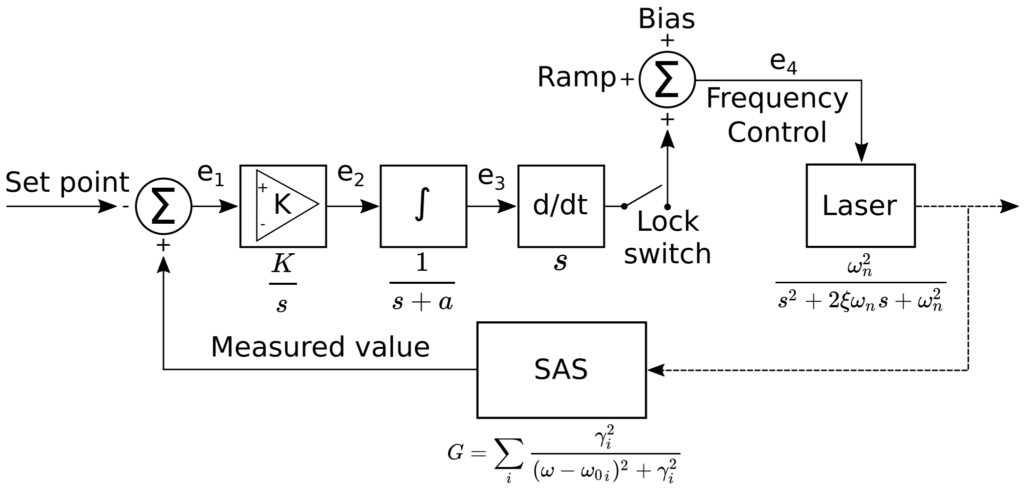

Figure 6.1: *Laser frequency control system, setup to perform side locking. The system consists of a proportional-integral-derivative (PID) controller, a laser, and a saturated absorption spectroscopy (SAS) setup. The solid arrows indicate voltage signals and the dashed arrows represent laser light.*

temperature rubidium (Rb) atoms. The output of the SAS setup is a voltage that is related to where the frequency of the light from the ECDL (dashed red line) lies on the frequency response curve (blue line), see Figure 6.2. The output of the SAS setup (measured value) is fed to the PID controller which compares it to a voltage that corresponds to a point on the frequency response curve where we want the laser to be locked; this voltage (set point) is indicated by green dashed lines in Figure 6.2. The difference between the measured value and set point (error) is used to adjust the piezoelectric actuator of the ECDL in such a way that the frequency of the light from the ECDL approaches the set point and is then maintained at that point.

6.2.1 Feedback Control Parameters

The dynamics of the system are governed firstly by the piezoelectric actuator, then by the parameters of the PID controller. In the PID controller we are able to vary parameters such as the gain and integration time, corre-

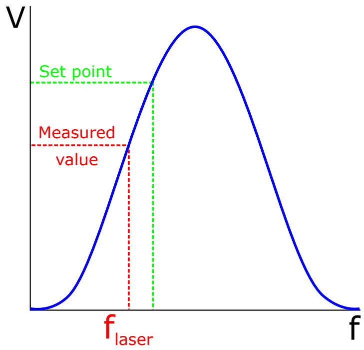

Figure 6.2: *Frequency response of the feedback network (blue curve). The green dashed line indicates the point on the response curve at which the laser frequency should be maintained, corresponding to the set point. The red dashed line indicates the point on the response curve that corresponds to the output voltage of the saturated absorption spectroscopy setup due to the laser frequency.*

sponding to the proportionality constant **K** and time constant **a** in Figure 6.1.

The gain scales the error in order for the output of the PID controller to adjust the ECDL so that the measured value approaches the set point. Usually this will cause an oscillation about the set point since the error can never remain exactly at zero. These oscillations will depend on the total transfer function[1] of the closed loop system. The poles of the transfer function in the S-plane will determine the type of response. For a damped system these oscillations will decay with time, and for an over-damped system there will be practically no oscillation in the output for step changes in the set point. The system can be made to be damped by choosing a large integration time constant.

The integrator takes the average of errors over a period and adjusts the

---

[1] The transfer function describes, mathematically, the relationship between the input and output of a system such as the feedback control system in our experiment.

output of the PID controller so that the resulting error does not oscillate about zero but instead settles approximately at zero. The integration time is usually set in such a way that it does allow for a very brief oscillation before settling.

We investigated experimentally how the gain and integration time affected the system by examining the following: how long the system remained locked, the response to a step change in set point, and the response to an impulse disturbance by applying a shock to the optical table. Minor analysis was performed on the test data, however tests were mainly for validating the systems ability to lock the frequency of the light from the laser to an atomic transition of rubidium.

6.3 Laser frequency Locking Procedure

The procedure for locking the frequency of the laser is as follows. We follow a similar procedure as we did for the spectral measurements of rubidium. Figure 6.3 shows plots of the input and output signals of the feedback control system as we progressed through the procedure.

- Set the lock switch on the PID controller to be in the off position.

- Monitor the laser frequency ramp signal and SAS output signal on an oscilloscope. A large enough ramp amplitude is chosen in order to observe all the hyperfine absorption peaks on the oscilloscope screen. (Figure 6.3a)

- The piezoelectric actuator voltage bias signal is then adjusted so that one of the hyperfine absorption peaks is positioned at the centre of the ramp-up time and oscilloscope screen (Figure 6.3b). The bias is then carefully adjusted so that a value along the side of the hyperfine peak lies at the centre of the ramp-up time and oscilloscope screen, this is where we want to lock the laser.

- The set point is adjusted to overlap the hyperfine absorption peak at the centre of the ramp-up time and oscilloscope screen, i.e. at the value where we want to lock the laser. (Figure 6.3c)

- The ramp signal amplitude is now gradually reduced, ensuring the desired point along the side of the hyperfine peak stays centred at the middle of the ramp-up time and oscilloscope screen. Eventually the SAS signal will be reduced to an almost flat line overlapping the set point on the oscilloscope screen. (Figure 6.3d)

- The lock switch on the PID controller is then set to the on position.

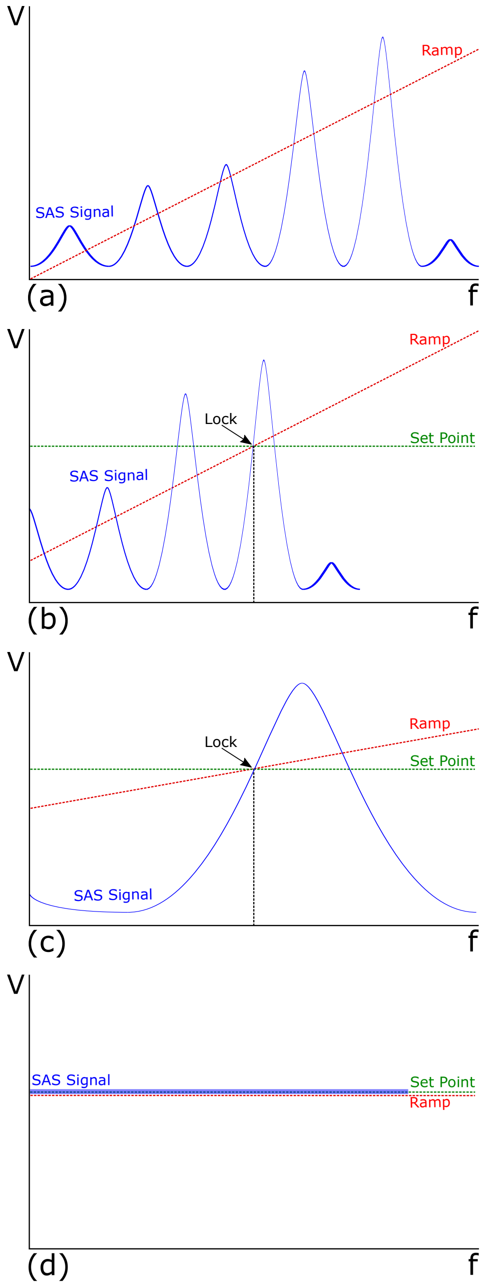

Figure 6.3: *Illustrations of the laser locking procedure. Plot* ***(a)*** *shows a large ramp that allows all the hyperfine absorption peaks (SAS signal) to be observed; the feedback system is disabled here. In plot* ***(b)*** *we shift a specific peak to the centre of the ramp and adjust the set point to overlap a point along the peak. Plot* ***(c)*** *shows the ramp amplitude reduced. In plot* ***(d)*** *the ramp has been reduced to zero and the peak has become a nearly flat line that overlaps the set point; at this point the feedback system is activated.*

6.4 Results

In this experiment we recorded the following signals: the SAS output, the set point, the ramp signal (laser frequency sweep). These signals were recorded using an oscilloscope and a computer software package called LabVIEW. The oscilloscope was used to record signals over short periods of less than 10 seconds, and LabVIEW was used for longer periods. These recorded signals were then normalised and filtered before analysis.

The goal of this experiment was to investigate the performance of the locking system from a qualitative perspective as a quantitative analysis was beyond the scope of the research. We investigated the long- and short-term stability of the system; the long-term test involved locking the laser frequency to the cooling transition of rubidium 87 for roughly one hour, whereas the short-term involved testing the response to a disturbance while locked to the same transition. The system was subjected to a step change in the set point in the form of an offset that was added to the set point using a digital-to-analog converter and LabVIEW, as well as an impulse disturbance that was produced by striking the optical table. All measurements were performed at night in order to minimise uncontrolled disturbances.

Initially the feedback control system was unable to maintain the frequency of the laser. We tracked the problem down and found that the feedback control system, which was a pre-built unit, had a slight design flaw. The integrator was not operating as required due to it being configured as an ideal integrator. We corrected this by adding two resistors to the integrator circuit: one in parallel with the capacitor (C1), and one between the positive input on the operational amplifier (pin 10, IC1C) and ground; the circuit diagram is given in Appendix C. It is worth noting that the design has the integrator output as the input to the gain amplifier, this is an unusual configuration for a PID controller as the error is usually amplified before the integrator.

6.4.1 Long-term Stability

Figure 6.4 shows the signals recorded during the long-term test of the feedback control system in which we used a gain of ≈ 0.52 and an integration time constant of 50×10^{-3} seconds. The system was able to able to maintain the frequency of the laser for one hour. Near the end of this hour we subjected the system to disturbances in the form of a change in the laser diode current as well as a change in the piezoelectric actuator voltage, both of which change the frequency of the light from the laser. These disturbances can be seen in Figure 6.5 which is a zoomed version of Figure 6.4 between 350 and 370 seconds. Note that the laser frequency is inversely proportional to the frequency control signal (piezoelectric actuator voltage). The feedback control system was able to maintain the frequency of the laser throughout these disturbances.

To obtain Figure 6.4 the following procedure was carried out. In Figure 6.6a the feedback control system is disabled and we have positioned a point along the hyperfine peak at the middle of the ramp-up time, coinciding with the set point. Hereafter the ramp is reduced to zero and the feedback control system is enabled.

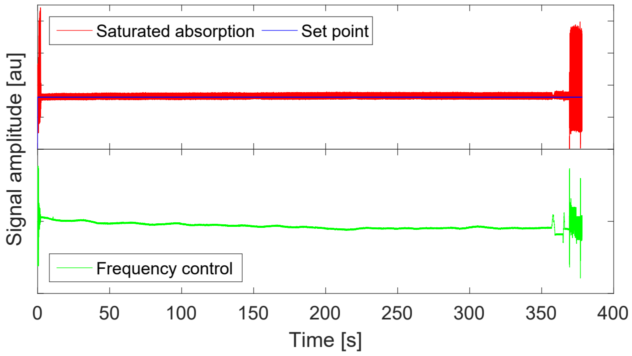

Figure 6.4: *Signals recorded during the long-term test of the laser frequency feedback control system. The green trace represents a signal to the laser which adjusts the piezoelectric actuator voltage and thus the laser frequency. The feedback system maintained the frequency of the light from the laser for one hour before it was manually disabled.*

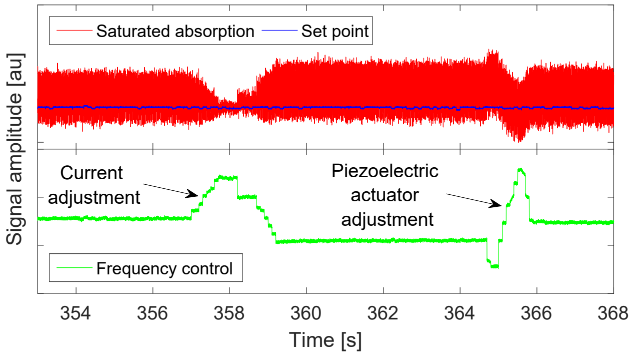

Figure 6.5: *Zoomed version of Figure 6.4, showing that the system was subjected to disturbances in the form of manual diode current and piezoelectric actuator changes on the laser controller.*

After an hour had passed the feedback control system was disabled. We then increased the ramp to view the hyperfine absorption peaks. In Figure 6.6b where we see that the point on the hyperfine which coincides with the set point and middle of the ramp-up time is approximately equivalent to what we started with in Figure 6.6a.

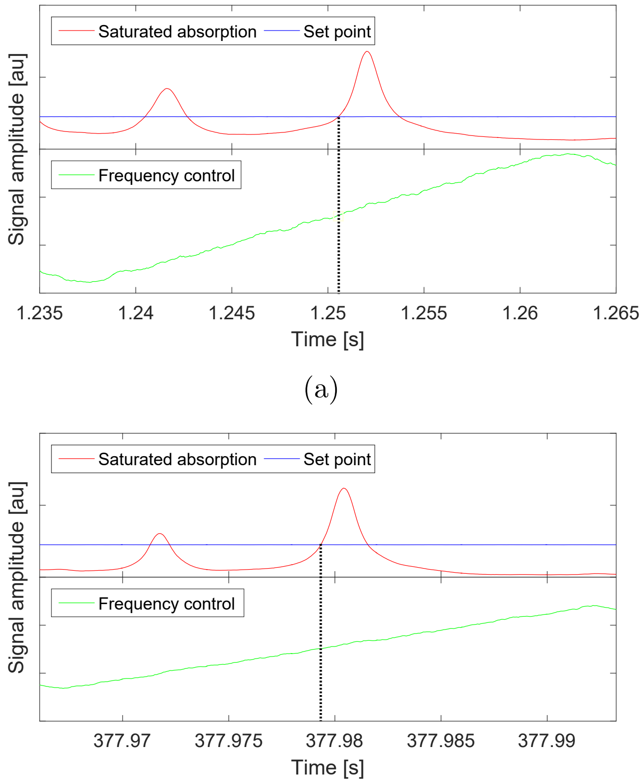

(a)

(b)

Figure 6.6: *Comparison of the position of the hyperfine absorption peak in our one hour test of the feedback control system. Plot (a) shows the peak position before enabling the feedback control system and plot (b) shows the position after disabling the feedback control system.*

6.4.2 Short-term Stability

Two types of tests were carried out: in the first the system was subjected to a set point step change of 400 millivolts, and in the second the optical table was struck in order to generate an impulse disturbance. During both types of tests the laser frequency was maintained at a point along a hyperfine absorption peak of 700 millivolts amplitude.

When testing the response to a step change in the set point, the gain and integration parameters of the PID controller were varied. These parameters are given in Table 6.1 along with test numbers that correspond to the plots in Figure 6.7; Figures 6.7a to 6.7d show samples of the signals recorded during the short-term tests, not all tests are shown. The dotted lines in Figures 6.7a to 6.7d show the region where the settling time of each test was calculated as this region is where the system was subjected to a disturbance.

Figures 6.7a to 6.7c show step changes in the set point value. As can be seen, the saturated absorption signal follows the set point as changes are made, and the control system now uses the new set point to which it follows. Figure 6.7d shows the situation where an impulse disturbance is applied by striking the optical table. Note that by striking the table the disturbance is applied directly to the laser head which contains the laser cavity. The cavity has a second-order response therefore we see oscillations in the saturated absorption and frequency control signals. The frequency of the oscillations was estimated to be ≈ 2.1 KHz. From these oscillations we infer the undamped natural frequency ω_n of the laser head to be ≈ 3.8 MHz, and the damping ratio ξ to be ≈ 0.9. This damping ratio implies that the system has an under-damped response to a disturbance.

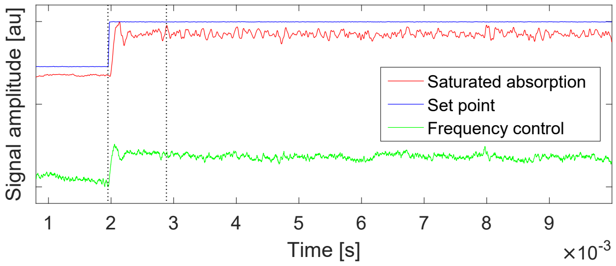

(a) Step response with a gain of 0.5 and an integration time of 50×10^{-3} seconds.

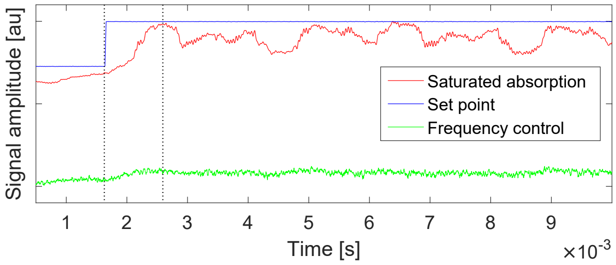

(b) Step response with a gain of 0.5 and an integration time of 610×10^{-3} seconds.

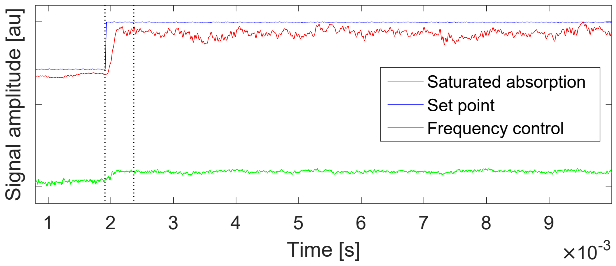

(c) Step response with a gain of 2.6 and an integration time of 610×10^{-3} seconds.

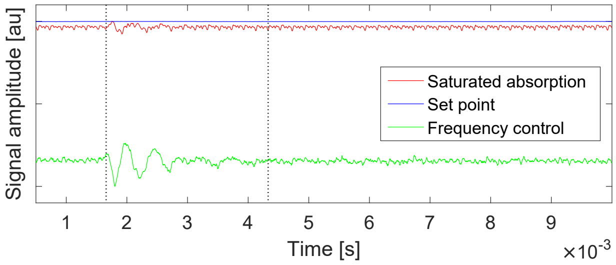

(d) Impulse response with a gain of 0.5 and an integration time of 50×10^{-3} seconds.

Figure 6.7: *Plots of the step and impulse response tests as is numbered in Table 6.1. The dotted lines in each plot correspond to the region we used to analyse the settling time of the feedback control systems output in each test. Plots (a) to (c) show the step response in tests 1,6, and 7, and plot (d) shows the impulse response in Test 10. The settling times in each test are given in Table 6.1.*

Table 6.1: *Parameters of the step and impulse response tests. The test numbers correspond to the plots in Figure 6.7, and the settling time corresponds to the dotted lines in Figures 6.7a to 6.7d.*

Test	Disturbance type	Gain	Integration time (s)	Settling time (s)
1	Set point step	0.5	50x10^{-3}	936x10^{-6}
2		0.5	101x10^{-3}	1.040x10^{-3}
3		0.5	147x10^{-3}	1.142x10^{-3}
4		0.5	204x10^{-3}	1.462x10^{-3}
5		0.5	371x10^{-3}	1.842x10^{-3}
6		0.5	610x10^{-3}	982x10^{-6}
7		2.6	610x10^{-3}	462x10^{-6}
8		4.6	610x10^{-3}	328x10^{-6}
9		6.8	610x10^{-3}	250x10^{-6}
10	Impulse	0.5	50x10^{-3}	2.670x10^{-3}

More details about the undamped natural frequency and damping ratio can be found in books that discuss measurement systems or control systems, such as Bentley (1995) and Kuo (1981).

6.5 Summary

We have examined both the long and short-term stability of the laser frequency feedback control system. The general agreement from both tests is that the laser frequency feedback control system operates as required, although we did have to make some minor corrections to the design of the system. Initially the integrator circuit had a design flaw that resulted in no integration taking place, thus the laser frequency was not maintained as expected. The addition of two resistors to the integrator circuit resolved this issue and the system then functioned as expected.

The long-term test showed how the system was able to maintain the laser frequency at the set point. When the control system was disabled we were able to confirm that the laser frequency was at the correct value by noting that the side of the peak to which we locked onto was still at the middle of the ramp-up time when the ramp was increased.

In the short-term tests the gain and integration time constants of the proportional-integral-derivative controller were varied to allow for observation of the response to a step change and an impulse disturbance. This step change was generated by adding an offset to the value of the set point and the system was subjected to an impulse disturbance by striking the optical table.

The aforementioned tests have shown that the system operates as required for experiments that will involve locking the frequency laser to an atomic transition of rubidium, specifically future laser cooling experiments.

Chapter 7

Summary and Conclusion

In this thesis the experimental study of the absorption spectra of rubidium, including the analysis of the Zeeman effect, has been presented. Also included in this study is an investigation of a feedback control system used to lock the laser frequency to a specific atomic transition of rubidium. This study represents an essential step towards developing the necessary laboratory infrastructure for laser cooling of rubidium.

A theoretical background required for carrying out the research was given and included atomic physics, absorption spectroscopy, and some basic feedback control theory. The atomic physics covered the energy level structure of the atom and quantum numbers in detail as this was very important in analysing the absorption spectra. A brief discussion on the process of Doppler cooling was provided since this research was done in preparation for experiments where Doppler cooling will be used to generate cold atoms. Understanding absorption spectroscopy is compulsory for the research since measuring the absorption spectra was one of the objectives. The feedback control theory is important for understanding the operation of the control system used to lock the laser frequency to the cooling and repumping atomic transitions of rubidium. Locking the laser to these transitions is crucial to the Doppler cooling process.

We have presented our study of the absorption spectra of room temperature rubidium using a saturated absorption spectroscopy setup. The study involved measuring the Doppler broadened and Doppler free absorption spectra of rubidium 85 and rubidium 87, as well as the Zeeman effect on the Doppler free absorption spectra.

The absorption spectra were measured using a non-polarised pump-probe spectroscopy arrangement and these measurements were improved upon by polarising the beam which allowed for better overlap between the pump and probe beams; a Michelson interferometer was used to calibrate all measurements. Our estimations of the excited state lifetimes and energy level separations show good agreement with the literature.

Additionally, adding a set of Helmholtz coils to the polarised saturated absorption spectroscopy setup allowed us to measure the Zeeman effect on the absorption spectra rubidium. A theoretical analysis of the energy level splitting was performed for both the ground and excited hyperfine energy levels of rubidium and we compared this with the measurement data. Initially we saw a discrepancy between the theoretical prediction and our measurements, thereafter, an more in-depth analysis showed an improved agreement between the theoretical predictions and measurements of the energy difference between certain transitions. The analysis of these measurements was made difficult by the fact that there are crossover resonances which also show splitting as the magnetic field is increased. In future, a more thorough theoretical analysis of the energy level splitting is to be completed. This in conjunction with a more accurately calibrated magnetic field should yield a better agreement between theory and experiment.

We investigated techniques for locking the frequency of the light from a tunable external cavity diode laser to a specific atomic transition of rubidium. We looked at side locking and peak locking techniques, however, only the feedback control system used for side locking was tested in our experimental setup. Due to time constraints, the peak locking system was tested using controlled inputs, the test results are given as an appendix. We recommend that this system be tested in the experimental setup in future.

From the above we conclude that all of the objectives identified in order to complete the research have been met. Furthermore, the theoretical knowledge and practical experience gained in setting up a laboratory while doing this research provides a good foundation for future experiments which will involve cold atoms.

Appendix A

Zeeman Energy Level Analysis of Rubidium 85 and 87

We present here a theoretical analysis of the magnetic energy levels in the hyperfine structure of rubidium 85 and 87 (^{85}Rb and ^{87}Rb). We follow the approach used by Pethick and Smith (2008). The full Hamiltonian of the atom is given by

$$H = \underbrace{\left[H_0' + \zeta(r)\vec{L}\cdot\vec{S}\right]}_{H_0} + A\vec{I}\cdot\vec{J} + \frac{\mu_B}{\hbar}\left(g_J\vec{J} + g_I\vec{I}\right)\cdot\vec{B} \ . \tag{A.1}$$

The meaning of the various terms are as follows:
H_0 is the basic atomic Hamiltonian including spin-orbit coupling. The solution of the eigenstates of H_0 results in the states with quantum numbers n, J, and m_J. The eigenstates are represented in Bra-ket notation as $|n\,J\,m_J\rangle$.

Looking at the other terms, represented by

$$H' = A\vec{I}\cdot\vec{J} + g_J\frac{\mu_B}{\hbar}\vec{J}\cdot\vec{B} + g_I\frac{\mu_B}{\hbar}\vec{I}\cdot\vec{B} \ . \tag{A.2}$$

$A\vec{I}\cdot\vec{J}$ is the hyperfine splitting due to the interaction of the nuclear spin with the magnetic field created by the orbiting electron. The next two terms are the interaction of the net orbital and spin dipole moments of the electron with an external magnetic field, and the interaction of the nuclear dipole moment with an external magnetic field.

The nucleus will have states denoted by quantum numbers I and m_J, i.e. $|I\, m_J\rangle$. We will use the uncoupled eigenstates $|J\, m_J\, I\, m_J\rangle$ to diagonalise H'. Letting $\vec{B}$ be in the z direction and noting that $F_z = I_z + J_z$, we then have

$$H' = A\vec{I}\cdot\vec{J} + g_J \frac{\mu_B}{\hbar} J_z B + g_I \frac{\mu_B}{\hbar} I_z B \tag{A.3}$$

$$\begin{aligned}
[I_z, H'] &= I_z(A\vec{I}\cdot\vec{J}) - (A\vec{I}\cdot\vec{J})I_z && \text{(A.4)}\\
&= A(I_z(I_xJ_x + I_yJ_y + I_zJ_z) - (I_xJ_x + I_yJ_y + I_zJ_z)I_z)\\
&= A(I_z(I_xJ_x + I_yJ_y) - (I_xJ_x + I_yJ_y)I_z)\\
&= A(J_x(I_zI_x - I_xI_z) + (I_zI_y - I_yI_z)J_y)\\
&= A(J_x\left[I_z, I_x\right] + \left[I_z, I_y\right]J_y)\\
&= A(I_yJ_x - I_xJ_y)i\hbar && \text{(A.5)}
\end{aligned}$$

$$\begin{aligned}
[J_z, H'] &= J_z(A\vec{I}\cdot\vec{J}) - (A\vec{I}\cdot\vec{J})J_z && \text{(A.6)}\\
&= A(J_z(I_xJ_x + I_yJ_y) - (I_xJ_x + I_yJ_y)J_z)\\
&= A(I_x(J_zJ_x - J_xJ_z) + (J_zJ_y - J_yJ_z)I_y)\\
&= A(I_x\left[J_z, J_x\right] + \left[J_z, J_y\right]I_y)\\
&= A(I_xJ_y - I_yJ_x)i\hbar && \text{(A.7)}
\end{aligned}$$

and it can be shown that

$$[J_z + I_z, H'] = 0 \tag{A.8}$$

Thus the z-component of the total angular momentum is conserved, but not the individual components. Therefore, all states for which $m_I + m_J \neq m'_I + m'_J$ will have $\langle m_I m_J | H' | m'_I m'_J \rangle = 0$.

The total matrix form of H' in the basis $|J\, m_J\, I\, m_J\rangle$ will have the following structure.

$$\begin{pmatrix} [H_1] & \cdot & \cdot & \cdot \\ \cdot & [H_2] & \cdot & \cdot \\ \cdot & \cdot & \ddots & \cdot \\ \cdot & \cdot & \cdot & [H_n] \end{pmatrix} \tag{A.9}$$

The basis $|J\, m_J\, I\, m_J\rangle$ are arranged in such a way that all basis having the same $m_I + m_J = m_F$ values are grouped together. H' will consist of matrices on the diagonal, all other components will be zero. We then find the eigenvalues of H_1, H_2, …, H_n, etc. as a function of the magnetic field $\vec{B}$.

We rewrite (A.3) as

$$H' = A\vec{I} \cdot \vec{J} + \left(g_J \frac{\mu_B}{\hbar} B \right) J_z + \left(g_I \frac{\mu_B}{\hbar} B \right) I_z \ . \tag{A.10}$$

$$\text{Let } C = g_J \frac{\mu_B}{\hbar} B \ , \tag{A.11}$$

$$\text{where } g_J = 1 + \frac{j(j+1) + s(s+1) - l(l+1)}{2j(j+1)} \ . \tag{A.12}$$

$$\text{Let } D = g_I \frac{\mu_B}{\hbar} B \ , \tag{A.13}$$

$$\text{where } g_I = -0.0009951414 \text{ (experimentally determined).} \tag{A.14}$$

We illustrate the process for the ground state of ^{87}Rb, where $I = {}^3\!/\!_2$ and $J = {}^1\!/\!_2$. The m_I and m_J values are:

$$m_J = {}^1\!/\!_2,\ -{}^1\!/\!_2$$
$$m_I = {}^3\!/\!_2,\ {}^1\!/\!_2,\ -{}^1\!/\!_2,\ -{}^3\!/\!_2$$

The uncoupled basis $|m_I\, m_J\rangle$[1] is

	Basis	m_F
1	$\left\|\frac{3}{2}\ \frac{1}{2}\right\rangle$	2
	$\left\|-\frac{3}{2}\ -\frac{1}{2}\right\rangle$	-2
2	$\left\|\frac{3}{2}\ -\frac{1}{2}\right\rangle$	1
	$\left\|\frac{1}{2}\ \frac{1}{2}\right\rangle$	1
3	$\left\|\frac{1}{2}\ -\frac{1}{2}\right\rangle$	0
	$\left\|-\frac{1}{2}\ \frac{1}{2}\right\rangle$	0
4	$\left\|-\frac{1}{2}\ -\frac{1}{2}\right\rangle$	-1
	$\left\|-\frac{3}{2}\ \frac{1}{2}\right\rangle$	-1

Using the raising and lowering operators,

$$I_+ = I_x + iI_y \tag{A.15}$$

$$I_- = I_x - iI_y \tag{A.16}$$

$$J_+ = J_x + iJ_y \tag{A.17}$$

$$J_- = J_x - iJ_y\ , \tag{A.18}$$

---

[1] $I = {}^3\!/\!_2$ and $J = {}^1\!/\!_2$ is understood and not indicated in the notation $|m_I\, m_J\rangle$.

we can write

$$I_x = \frac{1}{2}(I_+ + I_-) \tag{A.19}$$

$$I_y = \frac{1}{2i}(I_+ - I_-) \tag{A.20}$$

$$J_x = \frac{1}{2}(J_+ + J_-) \tag{A.21}$$

$$J_y = \frac{1}{2i}(J_+ - J_-)\ . \tag{A.22}$$

Then

$$H' = A\vec{I} \cdot \vec{J} + CJ_z + DI_z \tag{A.23}$$

can be written as

$$H' = AI_zJ_z + \frac{1}{2}(I_+J_- + I_-J_+) + CJ_z + DI_z\ , \tag{A.24}$$

where

$$J_z\,|m_I\,m_J\rangle = m_J\hbar\,|m_I\,m_J\rangle\ , \tag{A.25}$$

$$J_\pm\,|m_I\,m_J\rangle = \hbar\sqrt{(J \mp m_J)(J \pm m_J + 1)}\,|m_I\,m_J \pm 1\rangle\ , \tag{A.26}$$

and

$$I_\pm\,|m_I\,m_J\rangle = \hbar\sqrt{(J \mp m_J)(J \pm m_J + 1)}\,|m_I \pm 1\ m_J\rangle\ . \tag{A.27}$$

Using the standard formulas and properties of I_+J_-, I_-J_+, J_z, and I_z we can show that for the basis as grouped in Table A.1 we have the following matrices.

$$H_1 = \begin{bmatrix} \frac{3}{4}A + \frac{3}{2}C + \frac{1}{2}D & 0 \\ 0 & \frac{3}{4}A - \frac{3}{2}C - \frac{1}{2}D \end{bmatrix} \tag{A.28}$$

$$H_2 = \begin{bmatrix} -\frac{3}{4}A - \frac{1}{2}C + \frac{3}{2}D & \frac{\sqrt{3}}{2}A \\ \frac{\sqrt{3}}{2}A & \frac{1}{4}A + {}^{1}\!/\!{}_{2}C + \frac{1}{2}D \end{bmatrix} \tag{A.29}$$

$$H_3 = \begin{bmatrix} -\frac{3}{4}A + \frac{1}{2}C - \frac{3}{2}D & \frac{\sqrt{3}}{2}A \\ \frac{\sqrt{3}}{2}A & \frac{1}{4}A - {}^{1}\!/\!{}_{2}C - \frac{1}{2}D \end{bmatrix} \tag{A.30}$$

$$H_4 = \begin{bmatrix} -\frac{1}{4}A + \frac{1}{2}C - \frac{1}{2}D & A \\ A & -\frac{1}{4}A - {}^{1}\!/\!{}_{2}C + \frac{1}{2}D \end{bmatrix} \tag{A.31}$$

We solve for the eigenvalues of these matrices using MATLAB, for various values of the applied magnetic field $\vec{B}$. This process is repeated for the excited state of ^{87}Rb, where $I = {}^{3}\!/\!{}_{2}$ and $J = {}^{3}\!/\!{}_{2}$, and for the ground and excited states of ^{85}Rb.

The resulting eigenvalues are plotted as a function of the magnetic field $\vec{B}$ as follows. In figure A.1 we show the hyperfine energy level splitting of the ground (a) and excited (b) states of ^{85}Rb. Figure A.2 shows the hyperfine energy level splitting of the ground (a) and excited (b) states of ^{87}Rb.

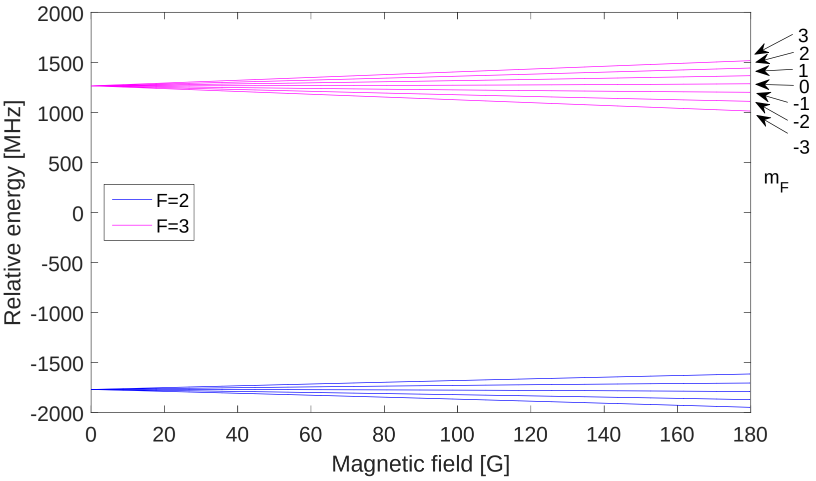

(a)

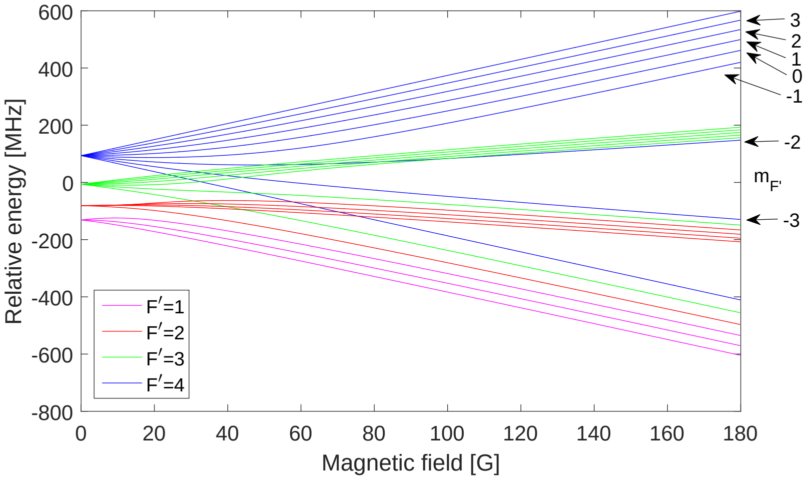

(b)

Figure A.1: *Theoretical Zeeman shifts for the* $5S_{1/2}$ *(a) and* $5P_{3/2}$ *(b) magnetic hyperfine levels of rubidium 85. The energy level from which each set of magnetic sub-levels originates is given by the line colour associated with the F quantum number in the legend. Only the transitions which we have analysed experimentally have been labelled.*

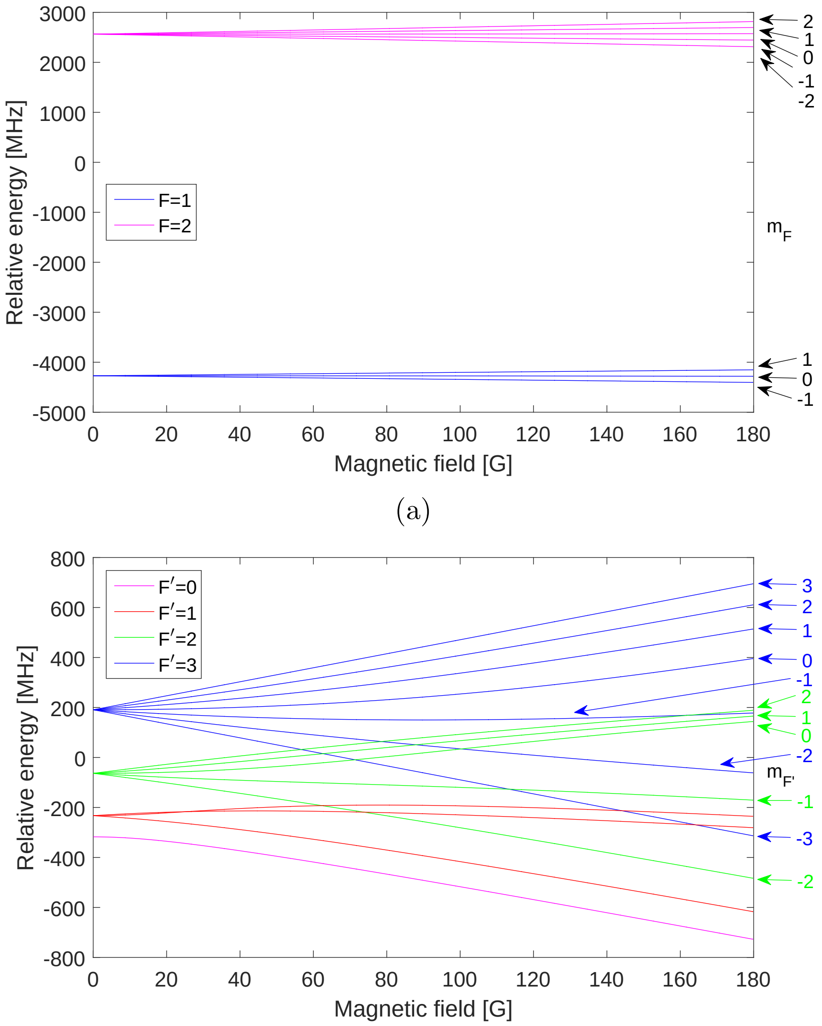

(a)

(b)

Figure A.2: *Theoretical Zeeman shifts for the* $5S_{1/2}$ *(a) and* $5P_{3/2}$ *(b) magnetic hyperfine levels of rubidium 87. The energy level from which each set of magnetic sub-levels originates is given by the line colour associated with the F quantum number in the legend. Only the transitions which we have analysed experimentally have been labelled.*

Appendix B

Lock-in Amplifier Theory and Testing

As mentioned in Chapter 3, we were unable to test the lock-in amplifier together with the saturated absorption experiment due to time limitations. In this chapter we cover more of the theory of operation of the lock-in amplifier, as well as tests of the operation of the lock-in amplifier. Figure B.1 shows a block diagram of the lock-in amplifier which can be used in conjunction with a feedback control system to lock the frequency of a laser to the maximum of an absorption peak; this is why we call it peak locking as opposed to the side locking feedback control system discussed in Chapter 6. Figure B.2, which has been discussed in Chapter 3, shows how the lock-in amplifier can be setup as a peak locking feedback control system, also shown in this figure are the hypothetical input and output signals of the lock-in amplifier.

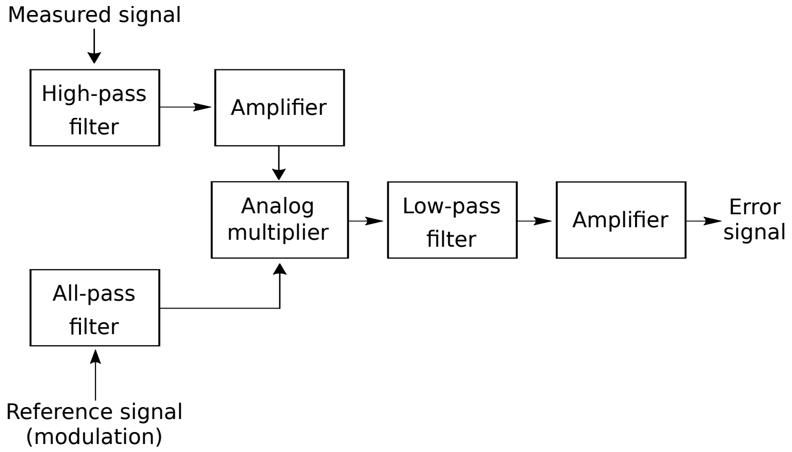

Figure B.1: *Block diagram of the lock-in amplifier which can be used with a feedback control system to lock the frequency of a laser to an atomic transition with the peak locking technique.*

Theory of Operation

The lock-in amplifier has two input signals: a reference signal and the signal from the saturated absorption spectroscopy (SAS) experiment which we will call the measured signal. The reference signal frequency is chosen to be far from the frequency of any noise sources (acoustic and electrical). The measured signal has the reference signal superimposed upon it due to the laser frequency being modulated with the reference signal (see Figure B.2a).

The reference signal is passed through an all-pass filter network to enable phase shifting of the signal relative to the saturated absorption signal. This is necessary because the measured signal is generally out of phase with the reference signal. The all-pass filter network consists of two all-pass filters in series which results in a theoretical phase shift of up to 360 degrees. The signal amplitude is unaffected as these filters have unity gain. The reference signal is given by

$$y_r = A_r(\sin\omega_r t + \phi) \ , \tag{B.1}$$

where A_r is the amplitude, ω_r is the modulation frequency and ϕ_r is an initial phase shift.

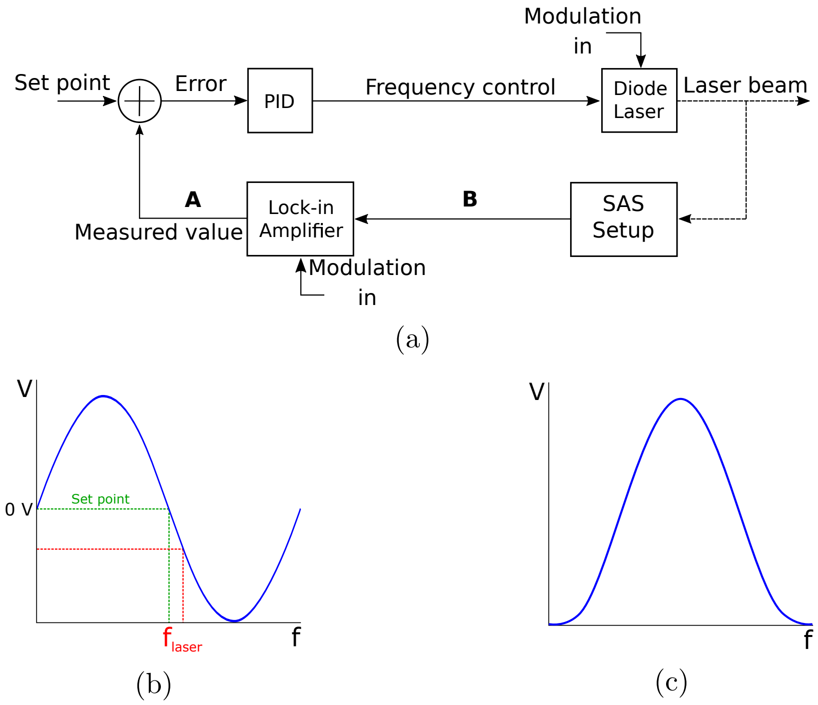
(a)

(b)

(c)

Figure B.2: *(a): Laser frequency feedback control system used to perform peak locking. The system consists of a proportional-integral-derivative (PID) controller, laser, saturated absorption spectroscopy experiment, and a lock-in amplifier. The solid arrows indicate voltage signals and the dashed arrows represent laser light.* ***A*** *and* ***B*** *correspond to the plots (b) and (c), respectively, beneath diagram (a). (b): Frequency response of the SAS setup (blue curve). The green dashed line indicates the point on the response curve at which the laser frequency should be maintained, corresponding to the set point. The red dashed line indicates the point on the response curve that corresponds to the output voltage of the SAS setup due to the laser frequency. (c): "Differentiated" frequency response of the SAS setup (blue curve).*

The measured signal is passed through a high-pass filter (HPF) and differential amplifier. The HPF removes any DC offset the signal may have and the amplifier increases the signal amplitude to a desired level. The amplifier also rejects any noise that is common in both the measured signal and ground as it is a differential amplifier. The measured signal is given by

$$y_m = A_m(\sin \omega_m t + \phi) \ , \tag{B.2}$$

where A_m is the amplitude, ω_m is the modulation frequency that is equal to ω_r, and ϕ_m is a phase shift.

After the input signals pass the input stage of the lock-in amplifier they are multiplied using an analog multiplier. The product of these signals is then

$$y_r \cdot y_m = \frac{1}{2} A_r A_m \left[cos(\omega_r - \omega_m) - cos(\omega_r + \omega_m)\right] t \ , \tag{B.3}$$

and contains two frequency components. Since the reference and measured signals have the common frequency, ω_r we are left with only the $2\omega_r$ frequency component. This stage of the amplifier is commonly referred to as the phase-sensitive detector since it amplifies only the components of either signal that are in-phase. The product is a maximum when the inputs are in-phase, the product is zero if the signals are 90 degrees out of phase, and the product is a minimum when the signals are 180 degrees out of phase.

To use the product signal in the laser frequency feedback control system (see Figure B.2a) it is required that the measured value input to the PID controller be a DC signal. We thus use a low-pass filter to output only the DC component of the product. The DC signal is then passed through a an amplifier. This signal is output from the lock-in amplifier and used as an input into the PID controller which maintains the laser frequency. Figure B.3 illustrates the change in the output of the lock-in amplifier for various changes in relative phase. The changes in the output signal as the phase difference between the two input signals increases agree with the theory described above. We therefore conclude that the lock-in amplifier is operates as intended.

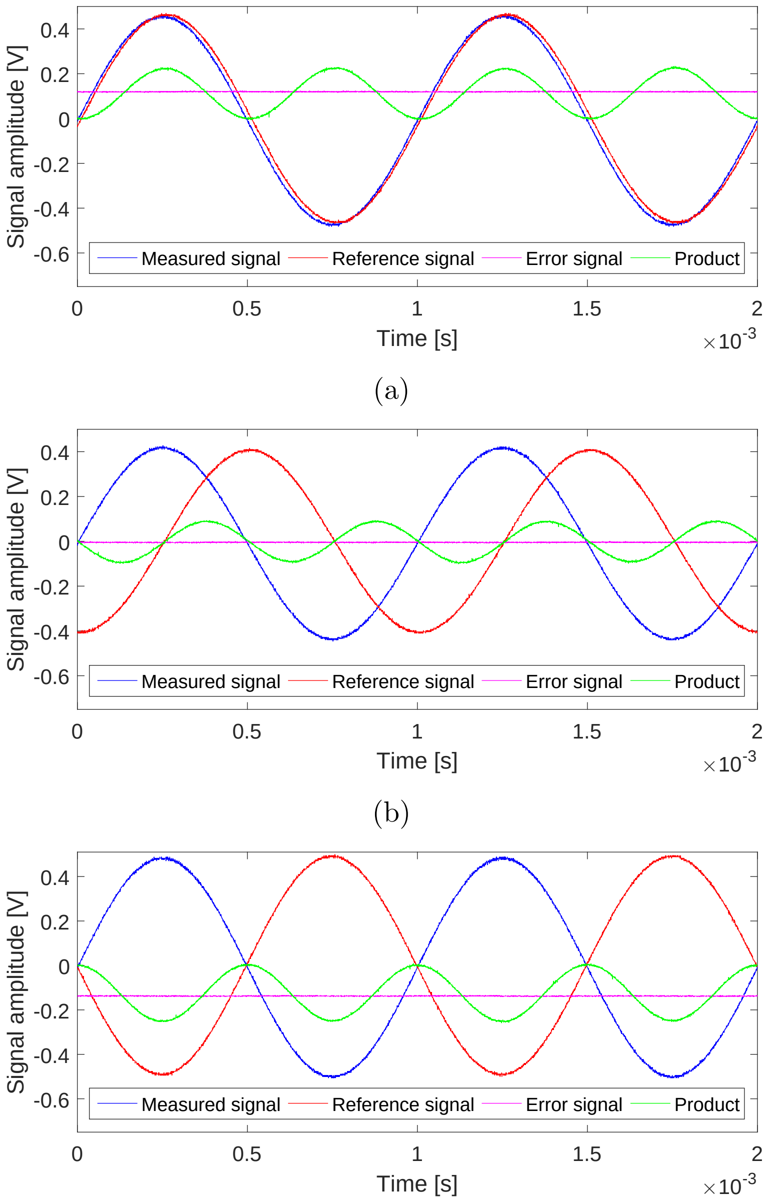

(a)

(b)

(c)

Figure B.3: *Various signals of the lock-in amplifier. The blue and red traces are the input signals, the green trace is the product of the input signals, and the pink trace is the output signal which corresponds to the DC offset of the product signal. (a):* 0 *degree phase shift between the reference and measured signal and the corresponding error signal. (b):* 90 *degree phase shift between the reference and measured signal and the corresponding error signal. (c):* 180 *degree phase shift between the reference and measured signal and the corresponding error signal.*

Appendix C

Laser Frequency Feedback Control System Circuit Diagram

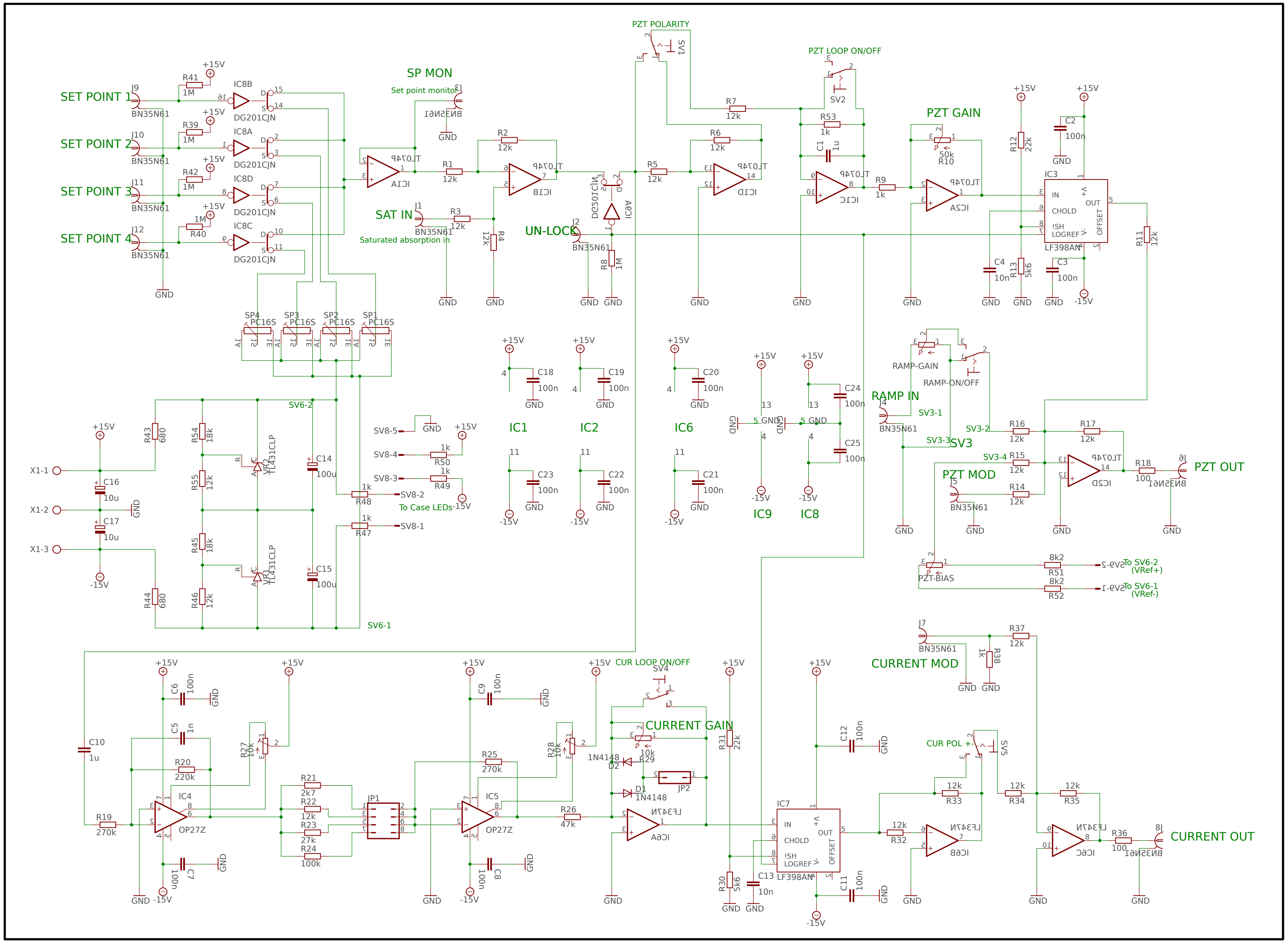

Figure C.1: *Circuit diagram of the laser frequency feedback control system.*

References

A1301 and A1302: Continuous-Time Ratiometric Linear Hall Effect Sensor ICs (2017). Allegro. URL: `http://www.allegromicro.com/en/Products/Magnetic-Linear-And-Angular-Position-Sensor-ICs/Linear-Position-Sensor-ICs/A1301-2.aspx` (visited on 2017).

Bader, S. and L. Zhou (2013). "Doppler-free Spectroscopy of hyperfine Zeeman effects in rubidium".

Balykin, V., V. Letokhov, and V. Mushin (1979). "Obseravtion of the cooling of free sodium atoms in a resonance laser field with a scanning frequency". *Journal of Experimental and Theoretical Physics Letters* 29(10), pp. 560–564.

Basov, N., I. Kompanets, O. Kompanets, V. Letokhov, and V. Nikitin (1969). "Narrow resonances in the saturation of absorption of SF6 by CO2 laser emission". *Zhurnal Eksperimental'noi i Teoreticheskoi Fiziki, Pis'ma v Redaktsiyu* 9(10), pp. 568–571.

Basov, N., O. Kompanets, V. Letokhov, and V. Nikitin (1971). "Investigation of narrow resonances within the Doppler line of the rotational-vibrational transitions of the SF6 molecule during absorption saturation". *Soviet Physics Journal of Experimental and Theoretical Physics* 32(2), pp. 214–219.

Bentley, J. (1995). *Principles of Measurement Systems.* 3rd. Longman Scientific & Technical, pp. 52–53.

Bloch, I. (2008). “Quantum coherence and entanglement with ultracold atoms in optical lattices”. *Nature.*

Bowie, J., J. Boyce, and R. Chiao (1995). “Saturated-absorption spectroscopy of weak-field Zeeman splittings in rubidium”. *Journal of the Optical Society of America B* 12(10), pp. 1839–1842.

Cheron, B., H. Gilles, J. Hamel, O. Moreau, and H. Sorel (1994). “Laser frequency stabilization using Zeeman effect”. *Journal de Physique III, EDP Sciences* 4(2), pp. 401–406.

Chu, S., L. Hollberg, J. Bjorkholm, A. Cable, and A. Ashkin (1985). “Three-Dimensional Viscous Confinement and Cooling of Atoms by Resonance Radiation Pressure”. *Physical Review Letters* 55(1), pp. 48–51.

Corwin, K., Z. Lu, C. Hand, R. Epstein, and C. Wieman (1998). “Frequency-stabilized diode laser with the Zeeman shift in an atomic vapor”. *Optical Society of America: Applied Optics* 37(15), pp. 3295–3298.

Dalibard, J., S. Reynaud, and C. Cohen-Tannoudji (1984). “Potentialities of a new σ_{+}-σ_{-} laser configuration for radiative cooling and trapping”. *Journal of Physics B* 17, pp. 4577–4594.

Eisberg, R. and R. Resnick (1985a). *Quantum physics of atoms, molecules, solids, nuclei, and particles.* 2nd. Wiley.

— (1985b). *Quantum physics of atoms, molecules, solids, nuclei, and particles.* 2nd. Wiley, pp. 364–370.

GC19075-RB - Rubidium Quartz Reference Cell (2017). Thorlabs. URL: `https://www.thorlabs.com/thorproduct.cfm?partnumber=GC19075-RB` (visited on 2017).

Gordienko, V., V. Gorshkov, V. Panchenko, and A. Sukhorukov (1977). “Kinetic cooling of a CO2-N2 gas mixture by CO2-laser radiation”. *Soviet Physics Journal of Experimental and Theoretical Physics* 46(3), pp. 459–464.

Hakhumyan, G., C. Leroy, Y. Pashayan-Leroy, and D. Sarkisyan (2011). “Study of Rb atomic transitions D 1,2 lines in strong magnetic field based on fluorescence spectra of sub-micron thin cell”. *SPIE. International Conference on Laser Physics 2010*, p. 79980V.

Hansch, T. and B. Couillaud (1980). “Laser Frequency Stabilization by Polarization Spectroscopy of a Reflecting Reference Cavity”. *Optics Communications* 35(3), pp. 441–444.

Hansch, T. and H. Schawlow (1975). “Cooling of Gases by Laser Radiation”. *Optics Communications* 13(1), pp. 68–69.

Javan, A., W. Bennet, and D. Herriott (1961). “Population inversion and continuous optical maser oscillation in a gas discharge containing a He-Ne mixture”. *Physical Review Letters* 6(3), pp. 106–110.

Kim, J., H. Kim, H. Moon, and H. Lee (1997). “Saturated-absorption spectroscopy of weak-field Zeeman splittings in rubidium: comment”. *Journal of the Optical Society of America B* 14(11), pp. 2946–2947.

Kompanets, O., A. Kukudzhanov, V. Letokhov, V. Minogin, and E. Mikhailov (1976). “Nonlinear laser spectroscopy of vibrational-rotational transitions in monoisotopic OsO4 molecules and stabilisation of CO2 laser frequency”. *Soviet Physics Journal of Experimental and Theoretical Physics* 42(1), pp. 15–22.

Kuo, B. (1981). *Automatic Control Systems*. 4th. Prentice Hall, pp. 327–331.

Lamb, W. (1964). “Theory of an optical maser”. *Physical Review* 134(6A), A1429–A1450.

Lancaster, G., R. Conroy, M. Clifford, J. Arlt, and K. Dholakia (1999). “A polarisation spectrometer locked diode laser for trapping cold atoms”. *Optics Communications* 170, pp. 79–84.

Letokhov, V. (1969). “Spatial effects in saturation of resonance absorption of a gas in a light field”. *Soviet Physics Journal of Experimental and Theoretical Physics* 29(5), pp. 937–940.

Macadam, K., A. Steinbach, and C. Wieman (1992). “A narrow-band tunable diode laser system with grating feedback, and a saturated absorption spectrometer for Cs and Rb”. *American Journal of Physics* 60(12), pp. 1098–1111.

Nakayama, S., G. Series, and W. Gawlik (1980). “Zeeman effect in the polarization spectroscopy of Na”. *Optics Communications* 34, pp. 382–388.

Nielsen, M. and I. Chuang (2010). *Quantum Computation and Quantum Information: 10th Anniversary Edition.* Cambridge University Press. ISBN: 9781139495486.

Okubo, S., K. Iwakuni, and T. Hasegawa (2012). “Modulation-free laser frequency stabilization to a saturated sub-Doppler spectral line in a transversal magnetic field”. *Optics Communications* 285.

Opeolu, V., K. Govender, A. Wyngaard, N. Ouassini, G. De Jager, and J. Scarrot (2018). “Analysis and Performance of a closed loop external cavity diode laser control system”. *The Proceedings of the 62nd Annual Conference of the South African Institute of Physics (SAIP2017).*

Petelski, T., M. Fattori, G. Lamporesi, J. Stuhler, and G. Tino (2003). “Doppler-free spectroscopy using magnetically induced dichroism of atomic vapor: a new scheme for laser frequency locking”. *European Physical Journal D* 22, pp. 279–283.

Pethick, C. and H. Smith (2008). *Bose-Einstein Condensation in Dilute Gases*. 2nd. Cambridge University Press, pp. 45–50.

Preston, D. (1996). "Doppler-free saturated absorption spectroscopy". *American Journal of Physics* 64(11), pp. 1432–1436.

Prodan, J., A. Migdall, W. Phillips, I. So, H. Metcalf, and J. Dalibard (1985). "Stopping Atoms with Laser Light". *Physical Review Letters* 54(10), pp. 992–995.

Ram, N., M. Pattabiraman, and C. Vijayan (2007). "Low Field Zeeman Magnetometry Using Rubidium Absorption Spectroscopy". *Journal of Physics: Conference Series* 80.

Rao, G., M. Reddy, and E. Hecht (1998). "Atomic hyperfine structure studies using temperature/current tuning of diode lasers: An undergraduate experiment". *American Journal of Physics* 66(8), pp. 702–712.

Ratnapala, A., C. Vale, A. White, M. Harvey, N. Heckenberg, and H. Rubinsztein-Dunlop (2004). "Laser frequency locking by direct measurement of detuning". *Optical Society of America: Optics Letters* 29(33).

Sesko, D., C. Fan, and C. Wieman (1988). "Production of a cold atomic vapor using diode-laser cooling". *Journal of the Optical Society of America B* 5(6), pp. 1225–1227.

Steck, D. (2013). "Rubidium 85 d line data".

— (2015). "Rubidium 87 d line data".

Stellmer, S., B. Pasquiou, R. Grimm, and F. Schreck (2013). "Laser cooling to quantum degeneracy". *Physical Review Letters* 110(26), pp. 1–18.

Svanberg, S. (2003a). *Atomic and Molecular Spectroscopy: Basic Aspects and Practical Applications*. 4th. Springer Berlin Heidelberg.

— (2003b). *Atomic and Molecular Spectroscopy: Basic Aspects and Practical Applications*. 4th. Springer Berlin Heidelberg, pp. 193–194.

Svanberg, S. (2003c). *Atomic and Molecular Spectroscopy: Basic Aspects and Practical Applications.* 4th. Springer Berlin Heidelberg, p. 21.

User's Guide 7000/6000 Series Tunable Diode Laser (n.d.). New Focus, p. 51.

Vachaspati, P. and S. Pasterski (2013). "Doppler-free spectroscopy of rubidium".

Weel, M. and A. Kumarakrishnan (2002). "Laser-frequency stabilization using a lock-in amplifier". *Canadian Journal of Physics* 80, pp. 1449–1458.

Wesenberg, J., R Epstein, D. Leibfried, R. Blakestad, J. Britton, J. Home, W. Itano, J. Jost, E. Knill, C. Langer, R. Ozeri, S. Seidelin, and D. Wineland (2007). "Fluorescence during Doppler cooling of a single trapped atom". *Physical Review A* 76(5), (053416)1–11.

Wieman, C. and T. Hansch (1976). "Doppler-free polarization spectroscopy". *Physical Review Letters* 36(20), pp. 1170–1173.

Wilson, J. and J. Hawkes (1987). *Lasers, principles and applications.* Prentice Hall, p. 159.

Wineland, D., R. Drullinger, and F. Walls (1978). "Radiation-Pressure Cooling of Bound Resonant Absorbers". *Physical Review Letters* 40(25), pp. 1639–1642.

Wyngaard, A., G. De Jager, C. Steenkamp, and K. Govender (2018a). "Doppler-free spectroscopy of the Zeeman spectra of 85Rb and 87Rb in the presence of a weak magnetic field". *Manuscript in preparation to be submitted to a journal.*

— (2018b). "Experimental study of the weak field Zeeman spectra of 85Rb and 87Rb". *The Proceedings of the 62nd Annual Conference of the South African Institute of Physics (SAIP2017).*